Politecnico di Torino

Corso di Laurea Magistrale in Ingegneria Aerospaziale

Tesi di Laurea Magistrale

Aerodynamic analysis and topological optimization of the supercar Montecarlo EVO model using CFD software

Supervisor: Prof. Iovieno Michele

Tutor: Ing. Zamboni Fabio

Candidate
D'Amato Emanuele

Abstract

This Master Thesis in Aerospace Engineering developed in *AGOM Engineering S.a.S.* deals with the numerical study of the external aerodynamics of the supercar Montecarlo EVO by means of *Star CCM+* CFD Software, with the main goals of lowering the drag coefficient and balancing the aerodynamic load on the car.

Contents

1 Theoretic Reference **1**
- 1.1 Fluid flow as a continuum 1
- 1.2 The difference between an ideal gas and a real gas . . . 2
- 1.3 Properties of fluids 4
- 1.4 Governing Equations of Fluid Dynamics 5
- 1.5 Laminar and turbulent flows 8
- 1.6 The boundary layer 11
  - 1.6.1 Laminar and incompressible boundary layer . . . 13
  - 1.6.2 Turbulent boundary layer 14
  - 1.6.3 Aerodynamic forces on a solid body 17

2 The aim of drag reduction on passenger cars **20**
- 2.1 The Aerodynamic drag 20
  - 2.1.1 Flow separation and wake 21
  - 2.1.2 Streamlined and blunt bodies: the importance of turbulent flows over race cars 23
- 2.2 Local generation of drag 26
  - 2.2.1 The front end 26
  - 2.2.2 The A-pillar and windshield 28
  - 2.2.3 Local generation of drag: the roof 29
  - 2.2.4 The "boat tailing" 30
  - 2.2.5 The fastback 31
  - 2.2.6 The wheels and wheel housings 32
  - 2.2.7 The front spoiler 34
  - 2.2.8 The rear spoiler 34

3 High-performance vehicles **36**
- 3.1 The importance of downforce in racecars 37
  - 3.1.1 Ground effect 40
  - 3.1.2 The wing 41
  - 3.1.3 The diffuser 44

3.1.4 Aerodynamical devices on the front end 45

4 Introduction to Computational Fluid Dynamics 46
4.1 The Finite Volume Method (FMV) and the mesh grid . 47
4.2 Boundary conditions 48
4.3 Space and time discretization and time solvers 49

5 Montecarlo EVO model analysis 52
5.1 The preparation of the geometry 53
5.2 Definition of the physics continuum 56
5.3 The setting up of the mesh 57
5.4 Post processing 76

6 Topological optimization 89
6.1 First topological changes 89
6.1.1 Variation of the car's pitch angle 90
6.1.2 Variation of the low spoiler incidence 94
6.1.3 Performance analysis of the 1.5° pitched car, 8° change of low spoiler incidence and spoilers' airfoils 97
6.2 Further topological improvements 101
6.2.1 Change of the splitter geometry 101
6.2.2 Twist angle removal on the high spoiler 102
6.3 Final comparative analysis 104

List of Figures 107

List of Tables 110

Bibliography 111

Chapter 1

Theoretic Reference

1.1 Fluid flow as a continuum

In nature, three states of aggregation of the matter can be found:

- *Solid*: molecular forces are strong, and molecules are fixed in their positions, so solid bodies mantain their shape and volume;
- *Liquid*: intramolecular bonds are lighter and molecules can slightly change their position. Liquids mantain their initial volume, but they conform to the shape of its container;
- *Gas*: intramolecular forces are such weak that molecules chaotically move due to molecular agitation; sure enought, gases don't have a proper shape and volume, but they entirely fill the volume of its container.

Gases and liquids can be collected in the "fluids" category. *A fluid is a matter that distorts limitlessly*, and actually can flow when a force acts on it.
Aerodynamics is the branch of fluid dynamics which studies the flow of the air around a solid body in order to determine forces and moments acting on it.
Fluids are composed by molecules and each of them can be studied by the *Boltzmann Equations*, but that's not in practical interest. It's important to study the macroscopic behaviour of the flow and its physical experimentally measurables quantities such as pressure, velocity, density and temperature.
Since the air is a mixture of gases (78% of nitrogen, 20% of oxygen and the remaining 2% composed by other gases), it is considerable a gas itself. In standard conditions of temperature and pressure ($T = 20°C$, $p = 1\ atm$), a kilomole of every gas contains $6.0233 \cdot 10^{26}$ molecules

(the so-called *Avogadro's number*) and occupies 22.414 m^3 according to the *Perfect gas Law*, that means that an infinitesimal volume contains thousands of molecules; it's enough to think that a $1\mu m$-sided cube can contain tens of milions molecules of air. It is suitable to define the *fluid particles*, small volumes of fluid associables to points that contain a sufficient number of molecules in order to have a proper statistical description of cinematic and thermodynamic properties (the average velocity, pressure, temperature...), then it's possible to formulate the *continuum hypothesis*: the fluid can be seen as a continuum, made by infinite fluid particles.
An important number to express wether continuum a fluid is or not is the *Knudsen number*, represented by the average distance between the molecules (mean free path) l_{mfp} divided by a characteristic length of the faced problem L, for example the length of a car or of a plane.

$$Kn = \frac{l_{mfp}}{L}$$

If $Kn << 1$, continuum hypothesis is satisfied

1.2 The difference between an ideal gas and a real gas

As every other gas, air has physical properties connected with molecular excitement. Two of them are:

- Viscosity: in a moving Newtonian fluid, two neighboring particles mutually exchange a pressure force on an ideal surface dS and a tangential force on that surface, a sort of internal friction force expressed by the *Newton's law*

  $$\tau = \mu \frac{du}{dy}$$

  Whre τ is the tangential stress, du is the infinitesimal variariation of velocity between two particles of air at an infinitesimal normal distance dy and μ is the viscosity of the fluid, evaluable through the *Sutherland's law*

  $$\mu = S \, \frac{T^{3/2}}{T + \chi}$$

where temperature T is expressed in Kelvin and

$$S = 1.458 \cdot 10^{-6} \ \frac{Kg}{m \ s\sqrt{K}}$$

is a constant value and $\chi = 110.4 \ K$ for air.

The viscosity of air in standard conditions is

$$\mu \simeq 1.8 \cdot 10^{-5} \ Pa \cdot s$$

- Thermal conducibility: this property produces a heat flux (heat per unit surface per unit time) $\dot{q}$; wherever a gradient of temperature occurs, the heat fluxed is expressed by the *Fourier's law*

$$\dot{q} = -k \ \nabla T$$

where k is the thermal conduction and the negative sign states that heat flux moves from warmer to colder places.

In standard condition, thermal conduction of air is

$$k = 25.87 \ \frac{mW}{m \ K}$$

In classical susbonic Aerodynamics, air can be considered as inviscid and having no thermal conducibility. An inviscid flow denies the existence of boundary layer and the wake, where viscous effects are dominant.

1.3 Properties of fluids

Beyond viscosity and thermal conduction, fluids may have many properties related to thermodynamics, mechanics, or other fields of science. In the following list there are mentioned only a few, which are principally used aerodynamics:

- Density: it is defined by a quantity of mass per unit volume. It is expressed by the formula

$$\rho = \lim_{V \to 0} \frac{m}{V}$$

  where V is the control volume and m is the mass contained in it;

- Pressure: it can be described as the normal force F, per unit area, acting on a surface S

$$p = \lim_{S \to 0} \frac{F}{S}$$

- Compressibility: A flow in which the density ρ is constant is called *incompressible* and a flow with variable density is called *compressible*. The compressibility β can be expressed as

$$\beta = -\frac{1}{V} \frac{dV}{dp}$$

  According to the Mach number, a flow can be considered as:

  - *Incompressible* for $M < 0.3$;
  - *Subsonic compressible* for $0.3 < M < 0.8$;
  - *Transonic* for $0.8 < M < 1.2$;
  - *Supersonic* for $1.2 < M < 5$;
  - *Hypersonic* for $M > 5$

  For general automotive applications the flow regime is considered incompressible, whereas for Motorsport applications the flow can speed up to compressible regime below the car.

1.4 Governing Equations of Fluid Dynamics

As a viscous Newtonian fluid, air behaviour is governed by the fundamentals equations of fluid dynamics, the *Navier-Stokes equations.*
The Navier-Stokes equations represent the conservation of mass, momentum and energy of fluid particles during their movement. A fixed and finite control volume will be used, in order to write the conservation laws in its conservative and integral forms.

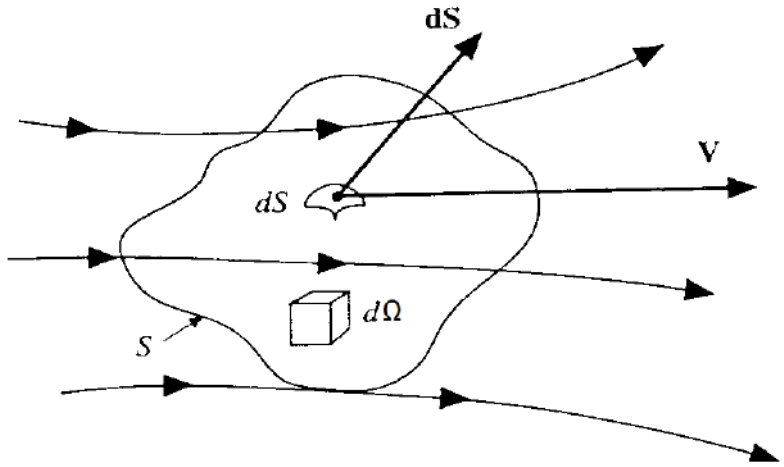

Fig. 1.4.1: Finite and fixed control volume (4)

1. Conservation of mass: the *law of conservation of mass* established that *matter is neither created nor destroyed.* Considering a fixed control volume, the time rate of change of mass is equal to the mass fluxes outwards the control volume

$$\frac{\partial}{\partial t}\int_{\Omega}\rho\, d\Omega + \int_{S}\rho\vec{V}\cdot\vec{n}\, dS = 0$$

2. Conservation of momentum: these vectorial equation derive from the *Newton's law of motion* $\vec{F} = m\,\vec{a}$
   The time rate of change of momentum inside a control volume is equal to the forces acting on it, as pressure, tangential and volumetric forces.
   $\frac{\partial}{\partial t}\int_{\Omega}\rho\vec{V}\, d\Omega + \int_{S}\rho\vec{V}\vec{V}\cdot\vec{n}\, dS + \int_{S}p\bar{\bar{I}}\cdot\vec{n}\, dS - \int_{S}\bar{\bar{\tau}}\cdot\vec{n}\, dS = \int_{\Omega}\rho\vec{f}\, d\Omega$

where p is the pressure, f is the volumetric force per unit mass and τ is the stress tensor. For a Newtonian fluid, we have

$$\tau_{i,j} = \delta_{i,j}\lambda\nabla \cdot v + \mu + \mu\left(\frac{\partial u_i}{x_j} + \frac{\partial u_j}{x_i}\right)$$

Where $\delta_{i,j}$ is Kroenecker's delta and $\lambda = -2/3\mu$ is the *bulk viscosity*

3. Conservation of energy: the third conservation law establishes that energy is neither created nor destroyed, but it only changes from one form to another. Here, the time rate of change of the energy inside the control volume is equal to the net heat flux towards the control volume and the work done per unit time on the control volume by volumetric and surface forces.

$$\int_\Omega \frac{\partial E}{\partial t}\, d\Omega + \int_S (E+p)\vec{V}\cdot\vec{n}\, dS - \int_s \left(\overline{\tau}\cdot\vec{V}\right)\cdot\vec{n}\, dS + \int_S \overline{\dot{q}}\cdot\vec{n}\, dS = \\ = \int_\Omega \rho\dot{\xi}\, d\Omega + \int_\Omega \rho\vec{f}\cdot\vec{V}\, d\Omega$$

where E is the total energy, $\dot{q}$ represent the heat fluxes frough the surfaces of the volume control and ξ represent the internal sources of energy.

In the end, we have 5 governing equations but 7 unknowns. to close the system it's possible to approximate air behaviour as a perfect gas, so we can use:

- the *perfect gas law*

$$\frac{p}{\rho} = \frac{R}{M}T$$

where $R = 8314\ \frac{J}{mol\ K}$ is the gas constant and M is the molar mass of air, expressend in kilograms per unit mole.

- The definition of internal energy

$$e = c_v T$$

and the specific heat at constant volume doesn't change for an ideal gas

For incompressible flows, the mass conservation law reduces itself at the *incompressibility condition*

$$\nabla \cdot \vec{V} = 0$$

and the momentum balance equation, after neglecting volume forces, can be written as

$$\rho \int_\Omega \frac{\partial \vec{V}}{\partial t}\, d\Omega + \int_S \rho \vec{V}\vec{V} \cdot \vec{n}\, dS + \int_S p\overline{\overline{I}} \cdot \vec{n}\, dS - \int_S \overline{\overline{\tau}} \cdot \vec{n}\, dS = 0$$

with $\tau_{i,j} = \mu \left(\frac{\partial u_i}{x_j} + \frac{\partial u_j}{x_i} \right)$. For an inviscid and stationary flow $\mu = 0$ and time derivatives are zero-valued and, for every streamline, the momentum equation -after the integration- becomes

$$p + \frac{1}{2}\rho V^2 = const$$

called *Bernoulli's equation.* It represents the sum of static and dynamic pressure and the value of the constant (representing the total pressure) changes its value for different streamlines; only in irrotational incompressible ideal flows the constant value is the same everywhere. This principle is often use for the explanation of the Venturi tube, and in the automotive industry finds its application on the diffuser for the creation of the *ground effect*, also called "Venturi effect" indeed.

1.5 Laminar and turbulent flows

Let us assume a free-stream flow along the x-axis with uniform velocity **V**.If we follow the traces made by several particles in the fluid we would expect to see organized lines parallel to the direction of the flow. This organized behaviour of the flow is called *laminar*; this behaviour is strictly dependent on the *Reynolds number*, a non-dimensional number expressed as

$$Re = \frac{VL}{\nu}$$

where L is a characteristic length of the considered problem and ν is the kinematic viscosity. As the Reynolds number increases, this flow loses its "organization", and fluid particles start to oscillate in every other direction around a mean direction and having an average speed $\overline{V}$.

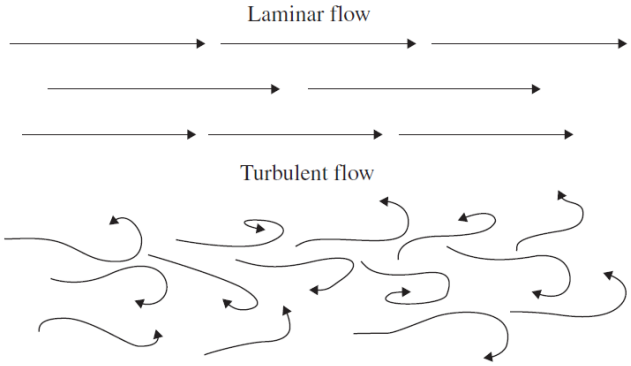

Fig. 1.5.1: Difference between laminar and turbulent flow (6)

Turbulent flow is time and space dependent with a very large number of spatial degrees of freedom. The random nature of the flow is experimentally observed using hot wire or Laser Doppler Anemometry.

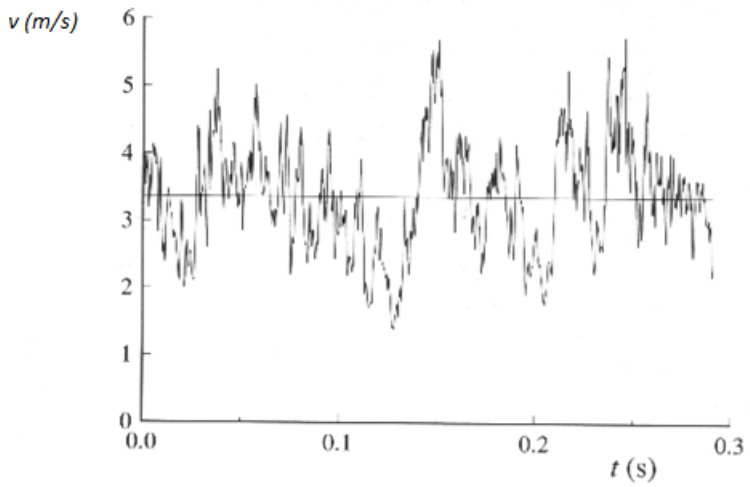

Fig. 1.5.2: Unsteady behaviour of turbulent flows (7)

Although turbulence is umpredictable in detail, its statistical properties are supposed reproducible and it is considerable to use statistical tools, such as the average value of the flow and its fluctuations. For every generic unsteady function f, we have

$$\overline{f} = \frac{1}{\Delta t} \int_{t}^{t+\Delta t} f(\tau)\, d\tau$$

$$f' = f - \overline{f}$$

Considering a flow moving in x-direction at an average velocity $\overline{U}$ and fluctuations u', v' and w' along the three directions, the velocity vector $\vec{V}$ can be expressed as the sum of the averaged value and its fluctuations.

$$\vec{V} = \left(\overline{U} + u'\right)\ \vec{i} + v'\ \vec{j} + w'\ \vec{k}$$

Splitting the velocity as written before (*Reynolds decomposition*) and averaging in time Navier-Stokes equation, we obtain a new set of equations *Reynolds Averaged Navier-Stokes equations* (RANS). For an incompressible bidimensional flow, the equations of conservation of mass can be written as

$$\frac{\partial}{\partial t} \int_{\Omega} \rho d\omega + \int_{\Omega} \rho \nabla \cdot \left(\overline{\overline{U}} + \overline{u}',\ \overline{v}',\ \overline{w}'\right) d\Omega$$

and, thus $\frac{\partial \overline{u_i'}}{\partial x_i} = 0$, we obtain

$$\frac{\partial}{\partial t}\int_\Omega \rho d\Omega + \int_\Omega \rho \frac{\partial \overline{U}}{\partial x} d\Omega$$

and the momentum balance equation are

$$\frac{\partial}{\partial t}\int_\Omega \rho\left(\overline{U}+u'\right)\, d\Omega + \int_S \rho\left(\overline{U}+u'\right)\vec{V}\cdot\vec{n}\, dS + \int_S \overline{p}\, n_x dS - \int_S \overline{\tau_x}\cdot\vec{n}\, dS = 0$$

$$\frac{\partial}{\partial t}\int_\Omega \rho v'\, d\Omega + \int_S \rho v'\, \vec{V}\cdot\vec{n}\, dS + \int_S \overline{p}\, n_y dS - \int_S \overline{\tau_y}\cdot\vec{n}\, dS = 0$$

$$\frac{\partial}{\partial t}\int_\Omega \rho w'\, d\Omega + \int_S \rho w'\, \vec{V}\cdot\vec{n}\, dS + \int_S \overline{p}\, n_z dS - \int_S \overline{\tau_z}\cdot\vec{n}\, dS = 0$$

Reynolds equations are formarly almost the same as the Navier Stokes equation with the appearence of the *Reynolds stress tensor*, which adds the stresses due to the turbulent fluctuations.
Besides its apparent randomness, one of the important characteristics of turbulent flows at high Reynolds number is the wide range of different space and time scales which they contain; in addition, as the Reynolds number increases the separation of scales between the widest and the smallest scales of turbulence.
The order of size of the wider spacial scale of turbulence is measured by a *correlation length* L, and the smallest is measured by the *Kolmogorov scale* η.
The kinetic energy related to the flow can be expressed as

$$\frac{1}{2}\overline{U_i U_i} = \frac{1}{2}\overline{U_i}\ \overline{U_i} + \frac{1}{2}\overline{u_i' u_i'}$$

where the first term in right hand side represents the kinetic energy of the mean flow and the second one represents the turbulent kinetic energy.
Combining u', L and ν it's possible to define the *turbulent Reynolds number*

$$Re_L^t = \frac{u'\ L}{\nu}$$

which is a measure of the significance of the viscosity for the large scales of turbulence: the larger Re_L^t is, the smaller the effects of viscosity on the large scales and the wider the range of scales present inside develop turbulence.

1.6 The boundary layer

"*A very satisfactory explanation of the physical process in the boundary layer between a fluid and a solid body could be obtained by the hypothesis of an adhesion of the fluid to the walls, that is, by the hypothesis of a zero relative velocity between fluid and wall. If the viscosity was very small and the fluid path along the wall not too long, the fluid velocity ought to resume its normal value at a very short distance from the wall. In the thin transition layer however, the sharp changes of velocity, even with small coefficient of friction, produce marked results.*" [Ludwig Prandtl, 1904]
With these sencentes written by Prandtl on his paper, he introduced the existence of the boundary layer at the Third Congress of Mathematicians at Heidelberg, in Germany: the boundary layer is a thin region created by the relative movement of a fluid around a surface, a region where the relative velocity between the wall and the fluid is zero and a high gradient of velocity along the normal direction of the wall takes place.

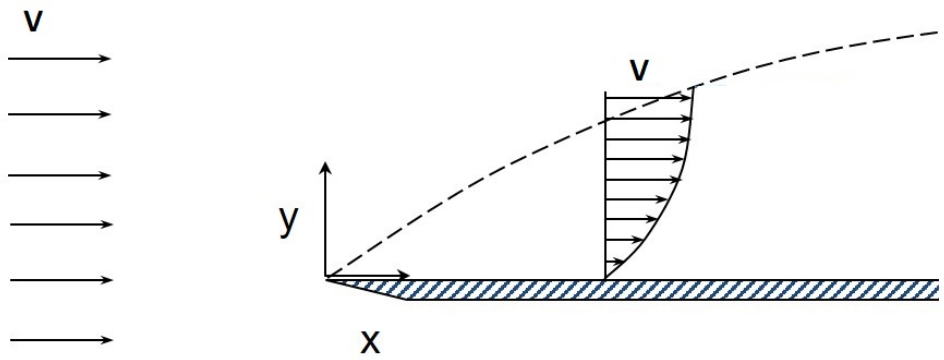

Fig. 1.6.1: Boundary layer

The Navier-Stokes equation well describe the behaviour of the flow in the boundary layer too. Considering an incompressible two-dimensional flow, the equations can be rearranged, thus we obtain

$$\frac{\partial(\rho u)}{\partial x} + \frac{\partial(\rho v)}{\partial y} = 0$$

$$\rho u\frac{\partial u}{\partial x} + \rho v\frac{\partial u}{\partial y} = -\frac{\partial p_e}{\partial x} + \frac{\partial}{\partial y}\left(\mu\frac{\partial u}{\partial y}\right)$$

$$\frac{\partial p}{\partial y} = 0$$

The consequence of the velocity gradient at the wall is the generation of the wall shear stress

$$\tau_w = \mu\left(\frac{\partial u}{\partial y}\right)_{y=0}$$

Therefore, it is possible to identify some properties of the boundary layer, that are:

- Boundary layer thickness δ: it is the region between the velocity profile starts from the zero value to the wall until the value of the distance y where $u(y) = 99\%V$. It will be defined in the following pages, making a distinction between laminar and turbulent boundary layer;
- Boundary layer displacement thickness δ^*: it represents the vertical displacement of the streamline due to the existence of the boundary layer

$$\delta^* = \int_0^\infty \left(1 - \frac{\rho u}{\rho_e V}\right) dy$$

- Momentum thickness θ: it represents the displacement for the momentum due to the existence of the boundary layer

$$\theta = \int_0^\infty \frac{\rho u}{\rho_e\, V}\left(1 - \frac{\rho u}{\rho_e V}\right) dy$$

1.6.1 Laminar and incompressible boundary layer

Considering a flat plate, the approximate solution of the boundary layer problem for an incompressible flow was given by Blasius. For an incompressible flow, the Navier-Stokes equations written for the boundary layer can be written as

$$\frac{\partial u}{\partial x} + \frac{\partial v}{\partial y} = 0$$

$$u\frac{\partial u}{\partial x} + v\frac{\partial u}{\partial y} = \nu\frac{\partial^2 u}{\partial y^2}$$

$$\frac{\partial p}{\partial y}$$

where $\nu = \mu/\rho$ is the *kinematic viscosity*, expressed in m^2/s.
Now, using a change of variables, we obtain

$$\xi = x \qquad\qquad \eta = y\sqrt{\frac{V}{\nu x}}$$

Defining the variable

$$f = \frac{u(y)}{V}$$

the equations of momentum becomes

$$2f''' + ff'' = 0$$

This is called the *Blasius equation*

- Boundary condition:

$$f = f' = 0 \qquad\qquad for\ \eta = 0$$

- Far-field condition:

$$f' = 1 \qquad\qquad for\ \eta \to \infty$$

From this Blasius solution, it can be found

- The skin friction coefficient c_f

$$c_f = \frac{0.664}{\sqrt{Re_x}}$$

- The boundary layer thickness

$$\delta = \frac{5}{\sqrt{Re_x}}$$

- The displacement thickness

$$\delta^* = \frac{1.72x}{\sqrt{Re_x}}$$

- The momentum displacement

$$\theta = \frac{0.664x}{\sqrt{Re_x}}$$

This solution is important for computational fluid dynamics, where an arbitrary body can be seen as a sequency of small flat plates.

1.6.2 Turbulent boundary layer

Considering a flow over a flat surface, the boundary layer is initially laminar. Therefore, as the Reynolds number increases due to the distance from the beginning of the surface, the local Reynolds number Re_x increases until it reaches a critical value Re_{crit}; at this point, the boundary layer starts its transition from laminar to turbulent, as shown in the following picture.

A turbulent boundary layer can be splitted into two regions:

- Inner layer:
- Outer layer

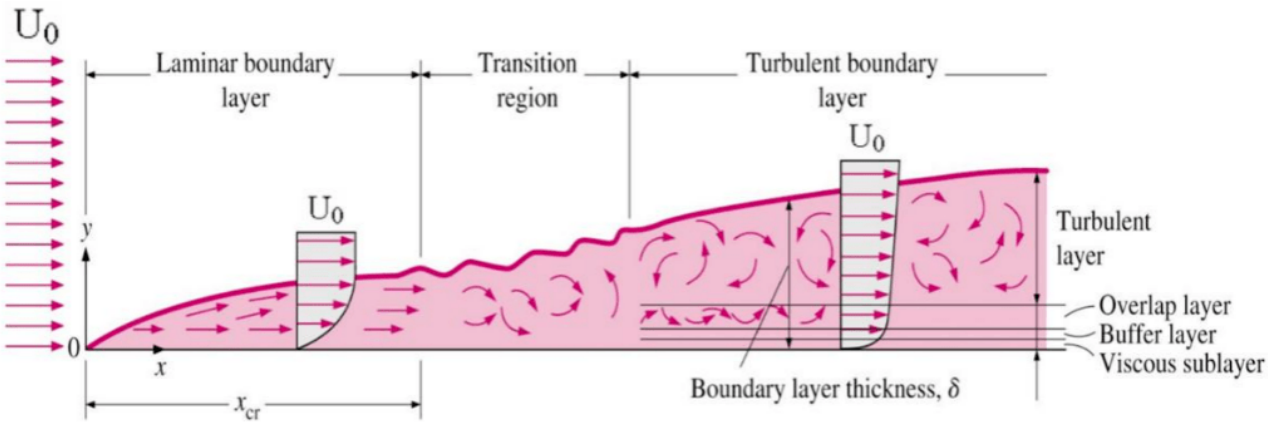

Fig. 1.6.2: Transition from laminar to turbulent boundary layer

The inner layer expands for the 20% of the total thickness of the boundary layer; in this region, because of the very low value assumed by the wall distance y, a new definition of variable is given by

$$y^+ = \frac{y}{l_v} \qquad\qquad u^+ = \frac{u}{u_\tau}$$

where l_v is the *viscous scale length*

$$l_v = \frac{\mu}{u_\tau}$$

and $u_\tau = \sqrt{\tau_w/\rho}$ is the friction velocity.
The inner layer could be furtherly divided into three regions:

- Viscous sublayer ($y^+ < 5$): it is the nearest region to the wall, and it is identified by the relation

  $$y^+ = u^+$$

  in this region viscous stresses are dominant.

- Buffer layer ($5 < y^+ < 30$): here, the most of the turbulent kinetic energy is produced;
- Logarithmic layer ($30 < y^+ < 1000$): in this region, we have

$$u^+ = \frac{1}{k} ln(y^+) + C$$

where $k = 0.41$ is the *Von Karman constant* and $C = 5.1$ is the *Coles constant*.

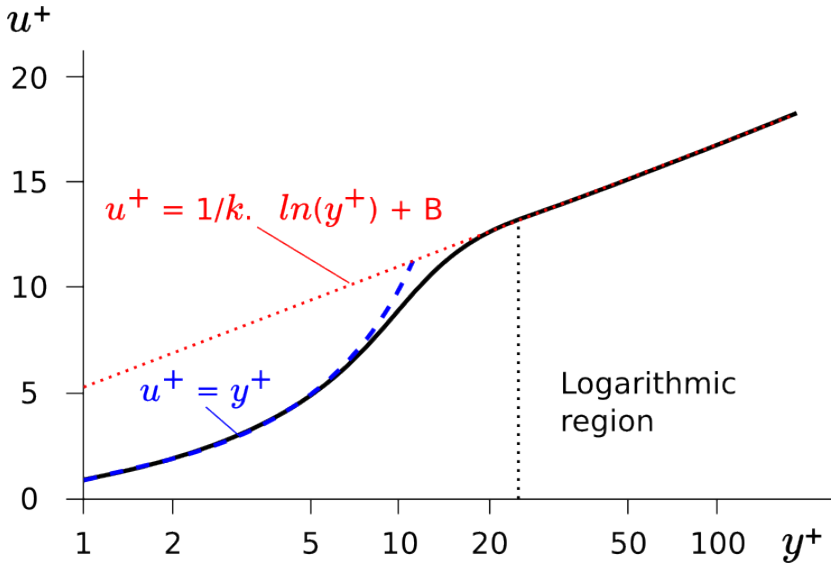

Fig. 1.6.3: Structure of the inner layer of a turbulent boundary layer

For an incompressible boundary layer the boundary layer thickness is

$$\delta = \frac{0.37}{Re_x^{0.2}}$$

and skin friction coefficient

$$c_f = \frac{0.074}{Re_c^{0.2}}$$

1.6.3 Aerodynamic forces on a solid body

According to the Navier-Stokes equation, pressure and velocity of the flow are strictly connetted each other. Every flud particle, varying its trajectory, changes its pressure and velocity too. There will be a pressure distribution around the body, e.g. an airfoil, and this pressure distribution will cause a force R acting on the body, given by

$$\vec{R} = \oint_{\sigma} (p - p_{\infty})\, \vec{n}\; d\sigma$$

where σ is the countour of the body and p_{∞} is the freestream pressure. This aerodynamic force can be splitted into a force parallel to the direction of the flow and a force perpendicular to it: they are rispectively the *drag* D and the *downforce* $-F_z$.

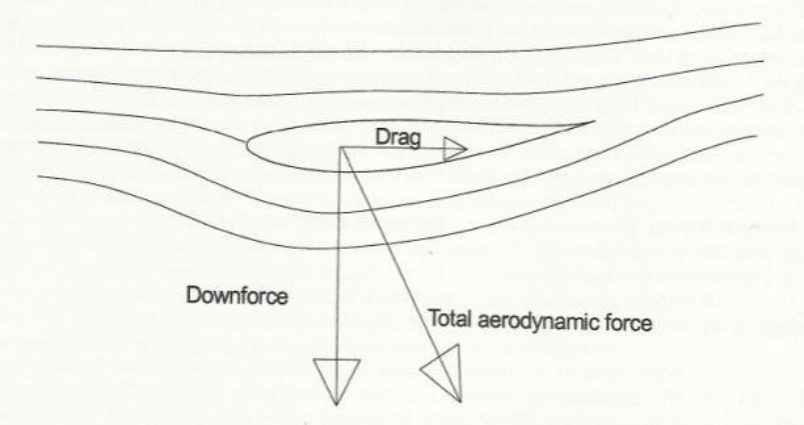

Fig. 1.6.4: Generation of drag and downforce over an airfoil

Considering a point of the airfoil, a pitching moment around it is generated too. Considering the leading edge of an airfoil which overall length is c, the pitching moment on the angle of attack is given by

$$M_{LE} = \int_0^c [(p_+ - p_{\infty}) - (p_- p_{\infty})]\, x\; dx$$

where p_+ and p_- are rispectively the pressure on the top and the bottom of the airfoil.
The effective point of application of the total aerodynamic force is called *center of pressure*.

Beyond the mere dimensional forces on a body, applied aerodynamics is interested in aerodynamic coefficients, that are the aerodynamic forces divided by the freestream dynamic pressure and for a reference surface (in the automotive field, that is the frontal area of the car S). It is possible then define the *drag coefficient* C_D and the *downforce coefficient* C_Z.

$$C_D = \frac{D}{\frac{1}{2}\rho V^2 S} \qquad\qquad C_Z = \frac{F_Z}{\frac{1}{2}\rho V^2 S}$$

and the pitching moment coefficient is

$$C_M = \frac{C_M}{\frac{1}{2}\rho V^2 S c}$$

The aerodynamic forces, as written before, can be predicted by the pressure distribution around the body. It is also useful to use the *pressure coefficient* C_P

$$C_P = \frac{p - p_\infty}{\frac{1}{2}\rho V^2}$$

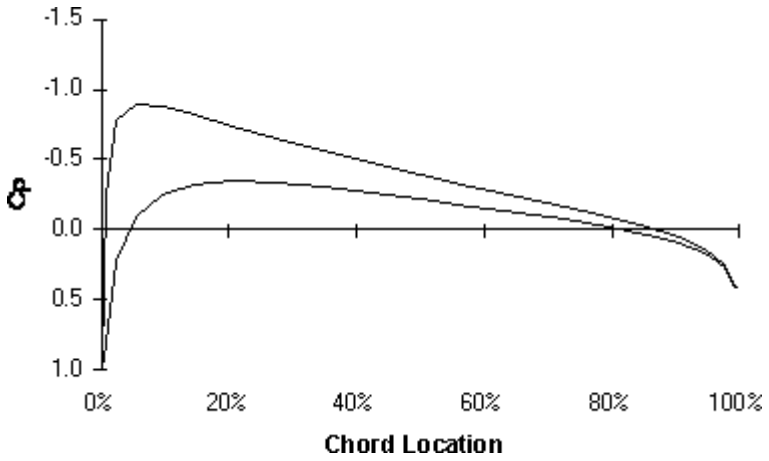

Fig. 1.6.5: Example of pressure coefficient distribution over an airfoil

The maximum positive value for the pressure coefficient is 1: it states that the flow has been reached the zero-value of velocity, and then the the flow has been arrested. The point in which this behaviour occurs is called *stagnation point*.
At fixed geometry, the values of C_D, C_Z and C_M are fixed and the values of drag, downforce and pitching moment depend only from the square velocity of the body, so

$$F_Z,\ D,\ M \propto V^2$$

Chapter 2

The aim of drag reduction on passenger cars

2.1 The Aerodynamic drag

The aerodynamic drag is added to the drag developed from the rolling of the tyres, as shown in the following picture

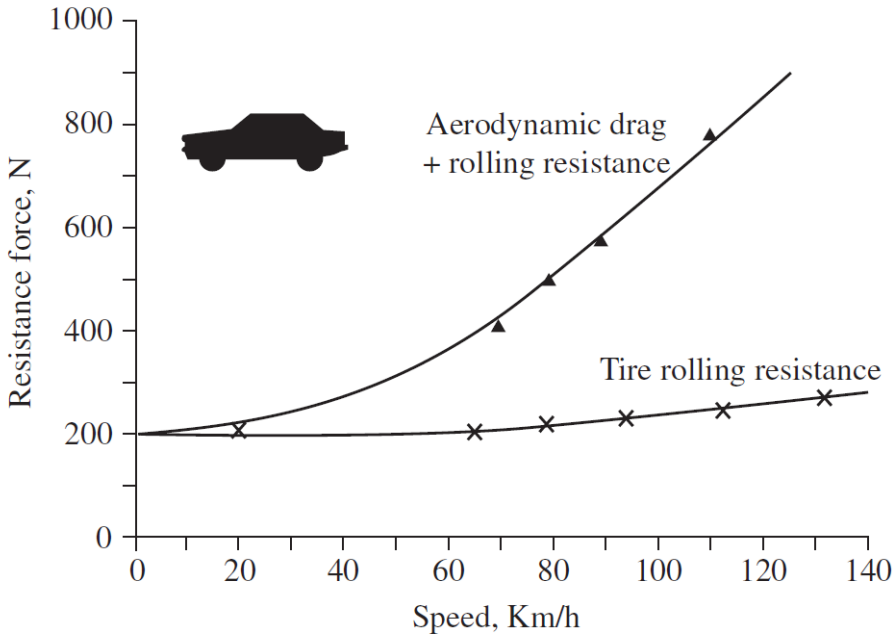

Fig. 2.1.1: Drag on a vehicle (6)

During the years, studies have been accomplished in order to reduce the drag coefficient of the car, that reflects itself in fuel consumptions too.

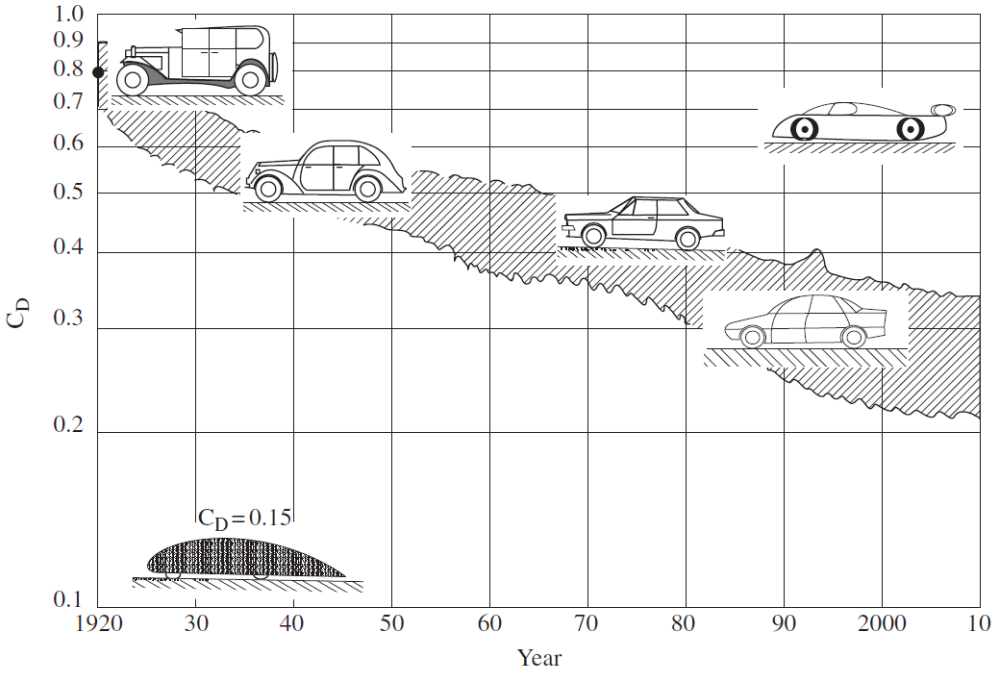

Fig. 2.1.2: Decrease of the drag coefficient during the years (6)

2.1.1 Flow separation and wake

Pressure drag on a solid body is due to the separation of the flow on the rear part of the body. If it were fully attached to the body till the very end, there wouldn't be a difference of pressure betewen (fully recovered pressure) the front and the rear part of the body and pressure drag would have been zero.
The flow around a body changes its velocity, and then pressure. Considering the pressure gradient on the longitudinal axis x we can distinguish:

- *Negative pressure gradient* $\partial p/\partial x < 0$: in these points the flow speeds up around the body;
- *Positive* or *Adverse pressure gradient* $\partial p/\partial x > 0$: in these regions the flow slows down. If the adverse pressure gradient is strong enough, the flow reverses its direction and vortices are produced; here, the arriving flow passes over the vortices, separating from the surface.

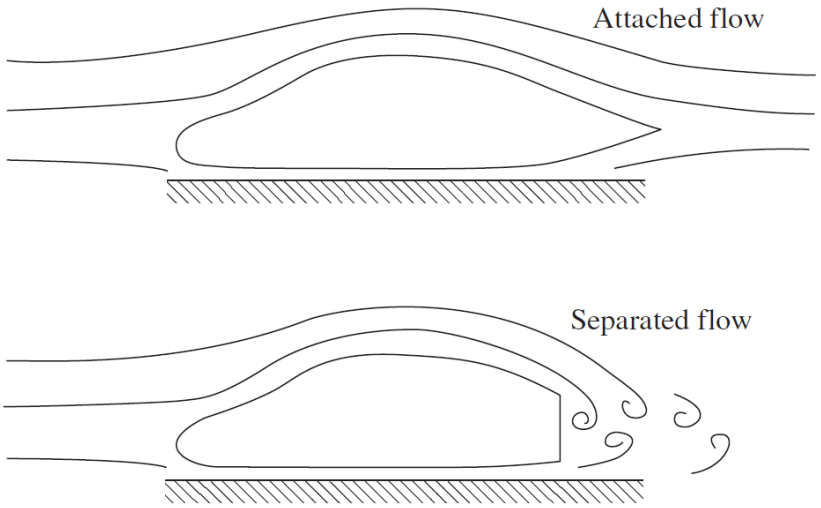

Fig. 2.1.3: Difference between attached and separated flow (6)

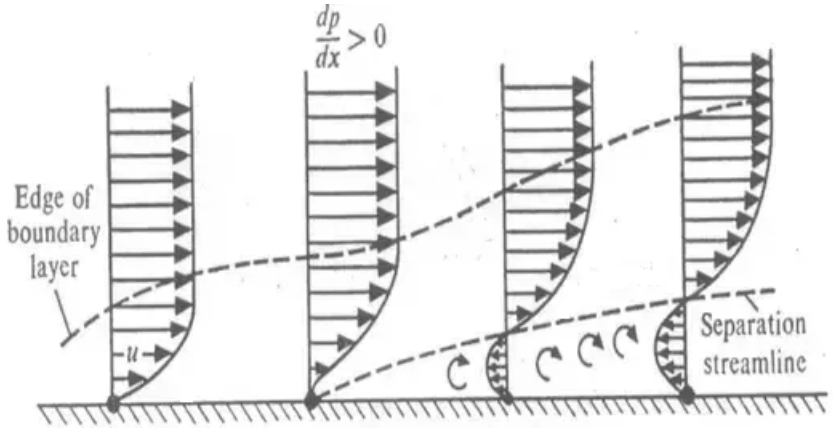

Fig. 2.1.4: Flow separation mechanism

The flow separation occurs when the velocity profile into a boundary layer presents a vertical tangent at the wall, so that $\frac{\partial u}{\partial y} = 0$; this implies that, when the flow separates, the wall shear is stress $\tau_w = 0$.
The region of separated flow after the rear part of the body is called *wake*.

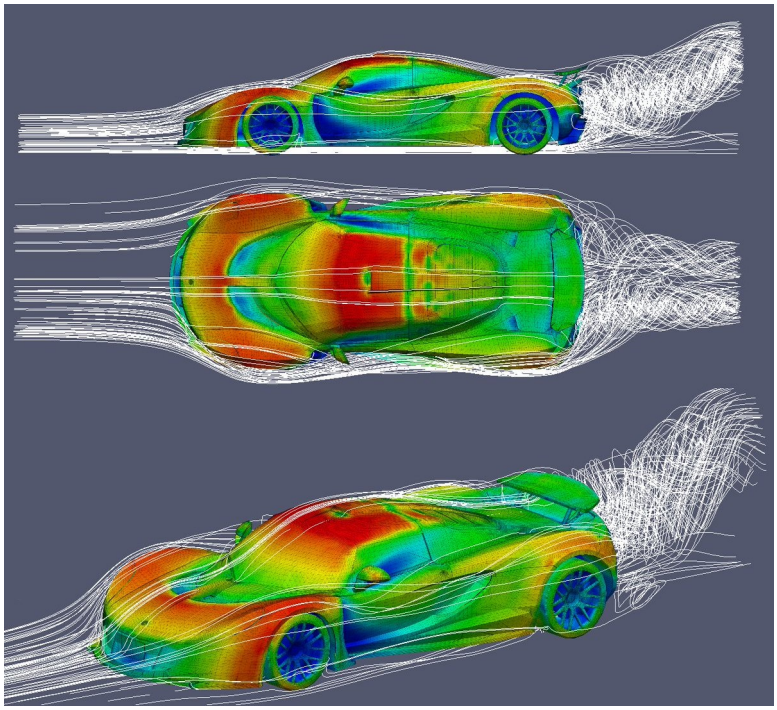

Fig. 2.1.5: Velocity field, streamlines and wake on a race car

2.1.2 Streamlined and blunt bodies: the importance of turbulent flows over race cars

In aerodynamics, bodies can be divided into two categories:

- *Streamlined bodies*: these bodies have their characteristic length much greater than the other dimensions (e.g. an airfoil): they can be distinguished for their very small wake, so the main drag source is given by shear stresses;
- *Blunt bodies*: Their characteristic length is the same order of magnitude as the other dimensions (e.g. a sphere). For this class of bodies, pressure drag is the main source of the overall drag.

An important feature of blunt bodies is the difference of the behaviour from laminar to turbulent flow over them. Examining, for example, the flow over a sphere, laminar and turbulent separations and their wakes are shown in the following picture.

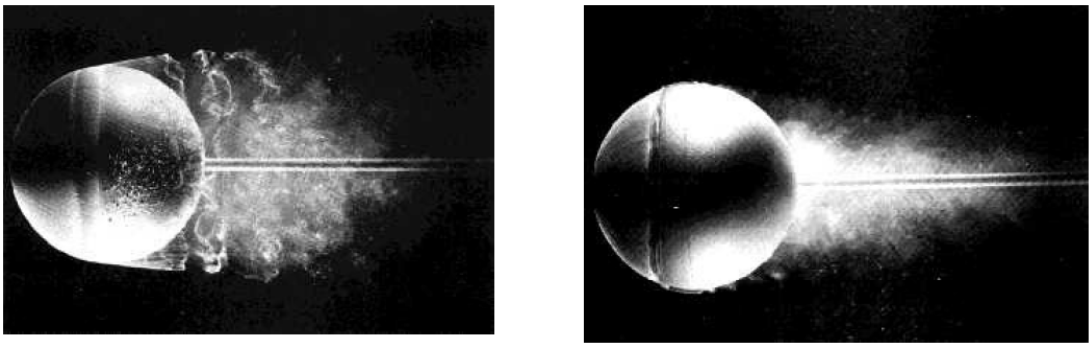

Fig. 2.1.6: Laminar and turbulent separation on a sphere

On the left, the wake of a laminar flow separation is shown; the wake generated is much greater than the wake generated by a turbulent flow. The size of the wake greatly influences the pressure drag, as the following diagram shows.

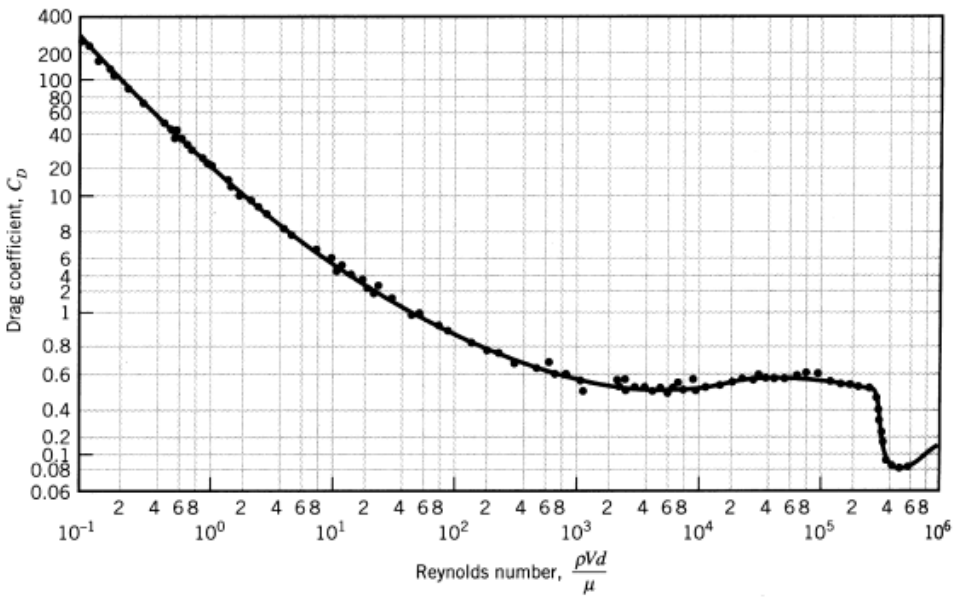

Fig. 2.1.7: $C_D - Re$ diagram of a sphere

As the Reynolds number increases, viscous effects become even less important and when the flow start its transition from laminar to turbulent regime the flow becomes even more energetic and it's more capable of following the sphere's surface and separates later than the laminar flow, reducing the wake size and then the pressure drag drop, as it can be seen in the figure for the drag coefficient when $Re > 3.5 \cdot 10^5$.

This is why racecars use *vortex generators*; the aim is to pick some of the kinetic energy of the freestream flow to create an earlier transition of the boundary layer, and delay the flow separation, improving the car's and even the wings' aerodynamical efficiency, defined by the ratio of downforce and drag.

Fig. 2.1.8: Vortex generators

However, among the years, pressure drag has been so much that reduced attention has to be paid to friction drag too, because its percentage on the overall pressure can't now be neglected.

2.2 Local generation of drag

2.2.1 The front end

The front end of a car can be roughly approximated as a square block; a stagnation point is formed on the vertical front face. because of the close proximity of the road, the air tends to flow over and around a vehicle rather than under it; the streamlines near the front end are therefore directed upward. The flow is significantly deflected at the intersection between the front face and the hood and fenders.

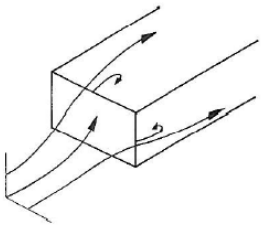

Fig. 2.2.1: Approximation of a front end and related streamlines (3)

Without special measures, this flow pattern will cause separation, with the result that the pressure distributions near the edges of the forebody will deviate from those for ideal flow.
To reduce the generation of drag at the front end, the edge radius, the slope of the hood and the slope of the front end face have been studied:

- In the case of the *edge radius*, an increasing value makes the front end less sharp, reducing the drag coefficient;
- The *inclination angle of the hood* helps in reducing the drag coefficient for moderate values, reaching rapidly its saturation effect. The drag-reducing effect of the hood inclination provides an example of interaction: with a sufficiently large leading-edge radius for the hood, drag reduction due to hood inclination should depend mainly on improved airflow in other regions so that the flow farther downstream can overcome a steeper adverse pressure gradient without separating.

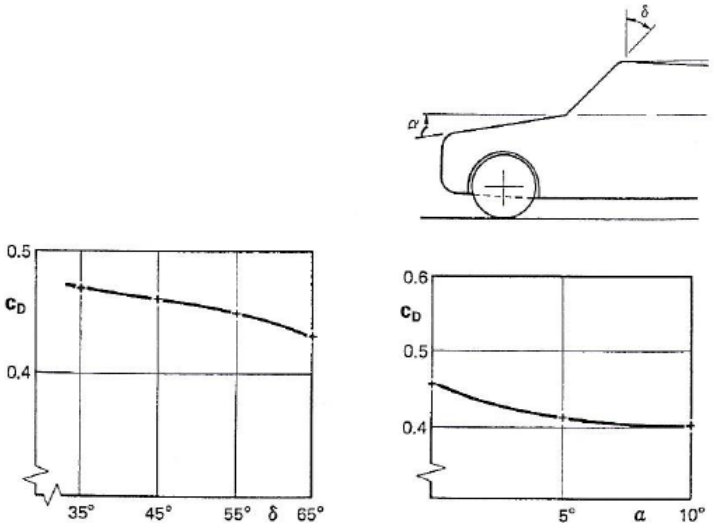

Fig. 2.2.2: Reduction of drag coefficient with hood and windshield inclination (3)

- The third parameter is the *front end inclination angle.*but it slightly reduces the drag coefficient.

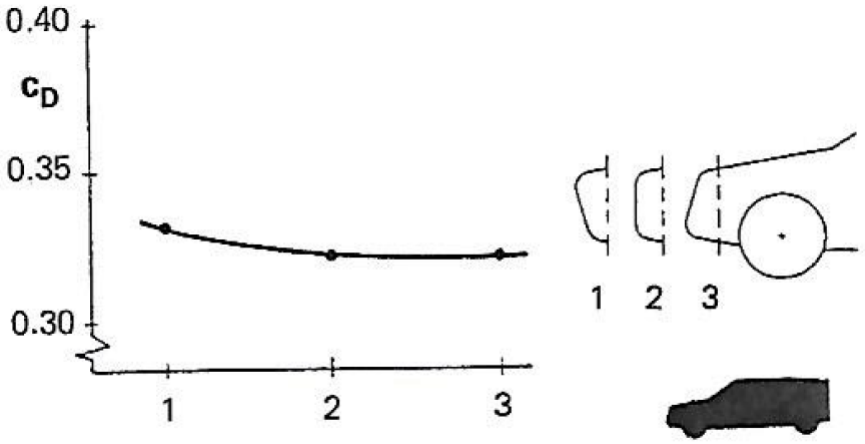

Fig. 2.2.3: Dependency of drag coefficient o the front end inclination (3)

2.2.2 The A-pillar and windshield

A schematic representation of the flow over the windshield and the A-Pillar is shown in the following figure

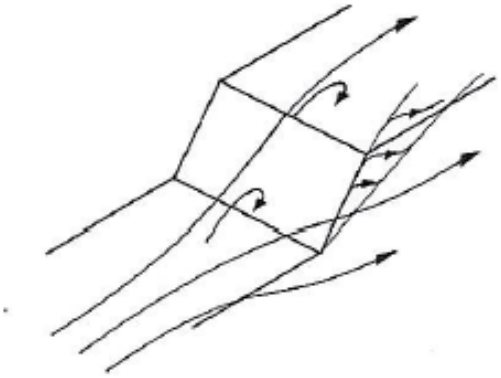

Fig. 2.2.4: Approximation of A-pillar and windshield and related streamlines (3)

Flow separation occurs in three different locations:

- At the base of the windshield, in the concave space formed by its juction with the hood;
- At the top of the windshield, at the junction with the roof;
- At the A-pillars.

For the first two separation a farther reattachment downstream can occur, the separation at the A-pillars is irreversible.

The three main parameters that descrie the geometry of windshield and A-pillar are:

- Radius of the A-pillars;
- The windshield inclination δ;
- The angle between hood and windshield ϵ

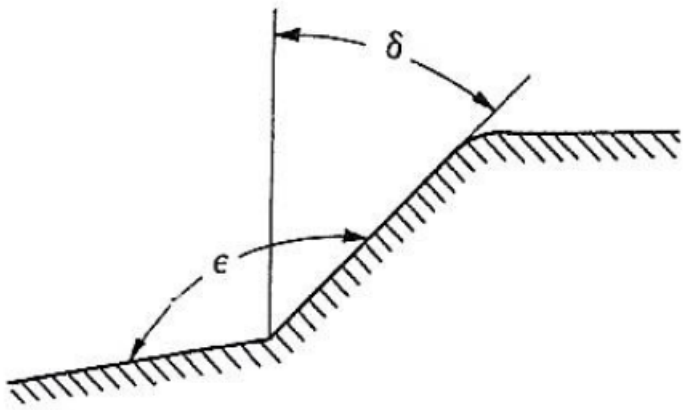

Fig. 2.2.5: Inclination angles of the windshield (3)

The size of the separation bubble at the base of the windshield is determined by the inclination angle between the windshield and the hood (called *dead water* region). With increasing windshield inclination δ drag is reduced but for $\delta > 60°$ there is no further significant reduction of drag coefficient.

2.2.3 Local generation of drag: the roof

The drag coefficient can be reduced by arching the roof in the longitudinal direction; however, if the curvature is too great, the drag coefficient can increase. The favourable effect of arching the roof depends on maintaining sufficiently large bend radii at the junctions between windshield and roof and between roof and rear window, so that the negative pressure peaks at these locations are not large and the corresponding pressure gradients are reasonably small.

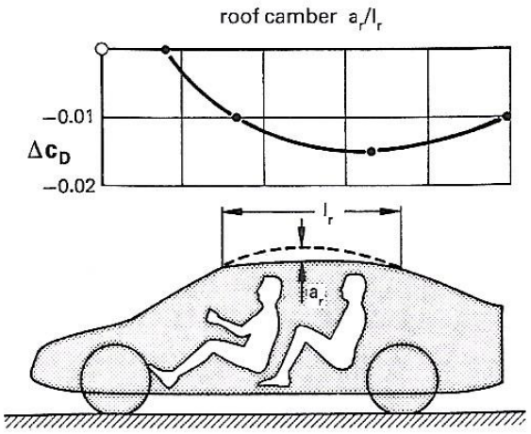

Fig. 2.2.6: Dependency of the drag coefficient on the roof camber (3)

2.2.4 The "boat tailing"

An aim of shape development is to make the static pressure at the end of a vehicle's body as high as possible and the base where this pressure acts as small as possible. This is made possible when tapering the rear, with a tecnique called *boat tailing*. An optimum tapering angle is found in 22°.

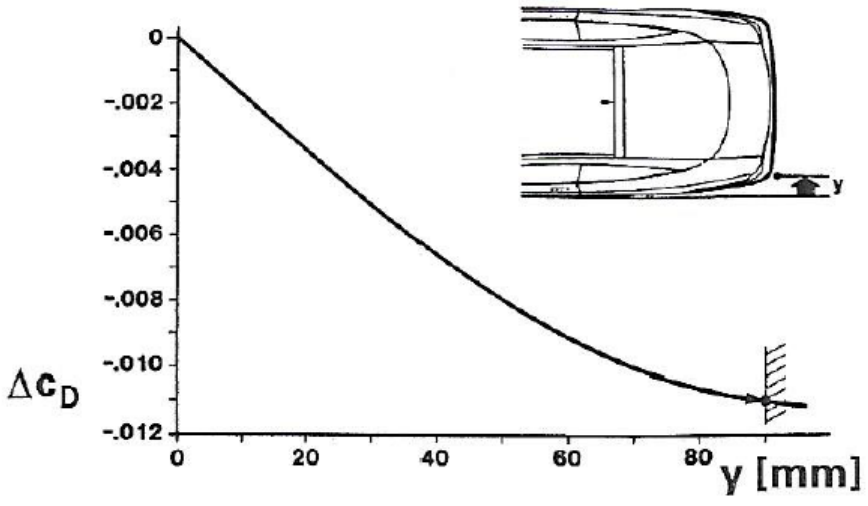

Fig. 2.2.7: The boat tailing technique (3)

2.2.5 The fastback

The fastback represents the latest rear car geometry that allows the best drag reduction.The formation of vortices on the slanted upper-rear surface of a vehicle is determined by its angle of inclination φ. Drag and lift at first rise steeply with an increasing slant angle. At a critical angle of $\varphi = 50°$ both forces suddenly drop. The following diagram shows some experimental measures at different slant angles.

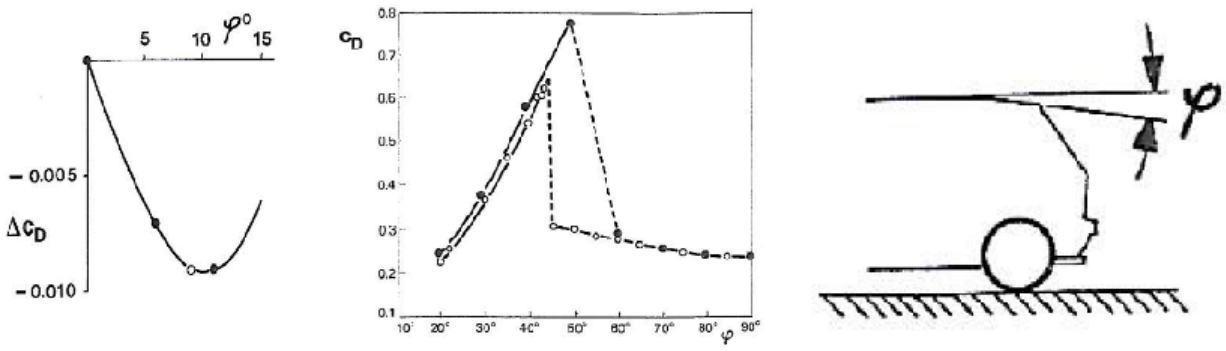

Fig. 2.2.8: Dependency of the drag coefficient on the slant angle φ (3)

2.2.6 The wheels and wheel housings

The contribution of wheels to the drag coefficient of a car is very high; with streamlined cars it can account for as much as 50% of the total drag. The cause of the disproproportionate contribution of the wheels to overall drag has three main reasons:

- *Wheels are not streamlined*: it becomes evident when it is considered as a circular cilinder, off ground and not rotating. If the shoulders of the wheel are sharp, the flow around it separates on both forward sides and vortices are shed from the sharped edges which roll up outward. If the shoulders are well rounded, the flow passes the forward facing part without separation.

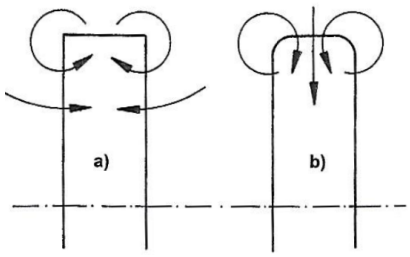

Fig. 2.2.9: Difference between sharped and rounded shoulders, vortex formation at the rear of a stationary wheel off ground (3)

These pair of vortices transport air into the wake region: in the case of sharp edges from both sides, and ind the case of rounded edges from above and underneath
A real car differs front this simple model because:

- The wheel rotates;
- The wheel touches the ground;

Even in the absence of a wheel housing, the flow now becomes asymmetrical from top to bottom, and a third vortex is shed by the axle. Due to viscosity, a rotating wheel adds energy to the flow in front of the wheel . Consequently, air is pressed out the stagnation zone with high velocity to both sides of the wheel. The vortices rolling up at the lower part are much more energized than for the stationary wheel off ground. Much more fluid is now drawn in by entrainment and transported into the dead-water region; the increase in pressure behind the wheel is more pronounced, and consequently the drag of a wheel rolling on the grown is lower than for

a stationary wheel off ground.

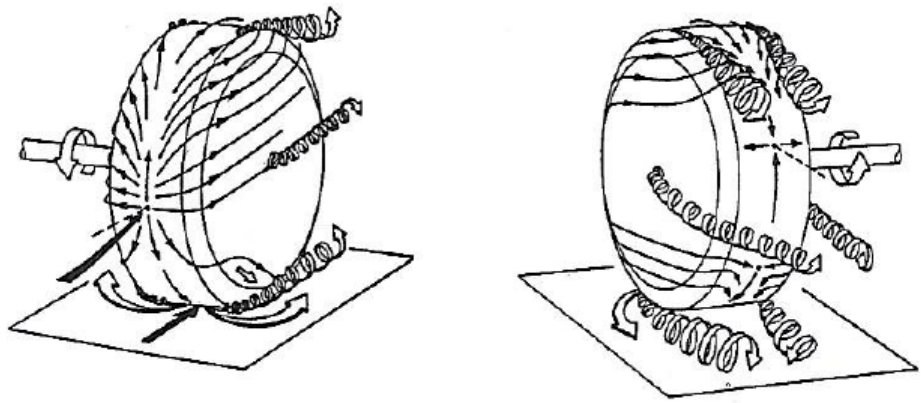

Fig. 2.2.10: Vortices on a 3D rotating wheel on the ground (3)

- *The local flow approaches the wheels under yaw*: the flow underneath a car spreads outward to the sides; consequently, the wheels are approached with an angle of yaw. The magnitude of this yawing angle depends on the overhang of the car's front end and of the outflow of radiator cooling air. For passengers car this yawing angle is about 15° at the front wheels. For the rear wheels, yawn angle is not exactly known but it is slightly lower than the yaw angle at the front tyres. A yawing angle causes the drag of a wheel to increase. For an angle of yaw of 15° the wheel's drag is more than three times the zero yaw value

- *The wheels rotate within wheel housings*: this fact further complicates understanding of the flow around a car's wheel, and a consistent physical model for the flow around a wheel within a wheel housing does not exist.

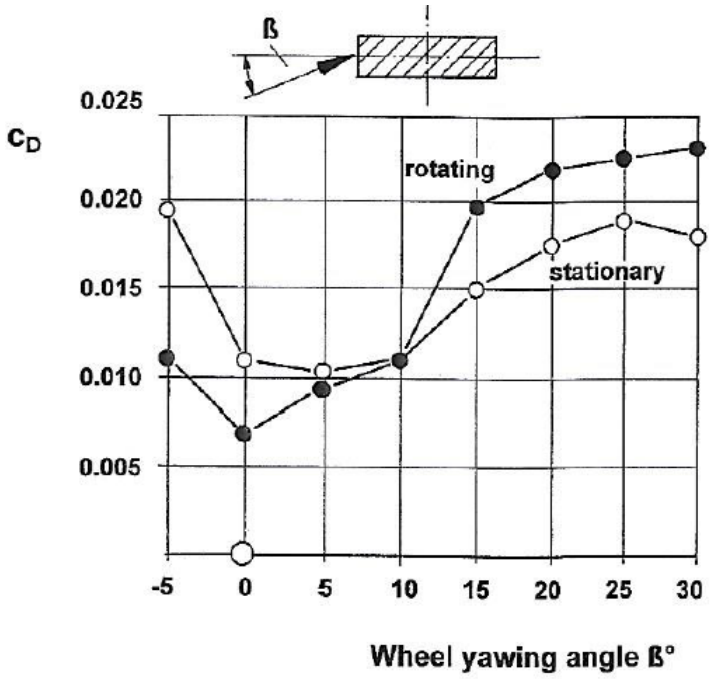

Fig. 2.2.11: Drag coefficient at increasing yaw angle (3)

2.2.7 The front spoiler

Three positive effects can be achieved with a well-designed underbody spoiler:

- Reduced drag;
- Reduced lift at the front axle;
- Increased volumetric flow of cooling air.

The drag-reducing effect of a front spoiler is based on the fact that it diminishes the air speed under a vehicle thus attenuating the contribution of the underbody airflow to overall drag. This contribution is normally due to the roughness and the non-streamlined nature of the underbody surface.

2.2.8 The rear spoiler

A rear spoiler can also have three effects:

- Reduction of drag;
- Reduction of the rear-axle lift;
- Reduction of dirt flow on the rear surface.

Two designs of the rear spoilers exist: deck strips and free-standing airfoils, that are shown in the following picture.

Fig. 2.2.12: From left to right, a deck strip and a free standing airfoil

The effect of a rear spoiler is fundamentally different from that of a front spoiler. It can be compared to the effect of a trailing edge flap on an aircraft wing.

Chapter 3

High-performance vehicles

High-performance vehicles are primarily characterized by a high power-to-weight ratio. The vital demands to be met by sports and racing cars can be identified in

- High accelerations;
- Very high decelerations;
- Excellent maneuvrability;
- Relatively low fuel consumption.

The three basic categories in which high-performance cars can be divided into are:

- Sports cars: they are designed for everyday use on public roads. They have high power-to-weight ratio, low center of gravity and compact outer dimensions and less priority is given to payload;
- Racing cars: these cars compete with other cars of the same category on special tracks; they are designed for maximum performance in terms of acceleration, top speed, braking power and cornering behaviour, and must comply with specific regulations which frequently also include special fuel consumption limits and safety instructions.
- Record cars: they are more restricted in their application spectrum and must comply with strict regulations.

Fig. 3.0.1: From top to bottom: a sports car, a racing car and a record car

3.1 The importance of downforce in racecars

The high downforce for racecars is needed for better tire adhesion (resulting in faster laps); the large increase in drag is a result of the increased negative lift (downforce) and it resembles the induced drag dependency on downforce.
The resultant aerodynamic loads acting on a road vehicle may be described by three force and three moment components. While cornering, there will be a *slip angle* β between the longitudinal axis of the car and the wheel axis. The friction coefficient of the tyre can be expressed as

$$\mu = -\frac{F_y}{F_z}$$

The following figure shows the dependency of the lateral force F_y on the slip angle, considering two diferent aerodynamic loads.

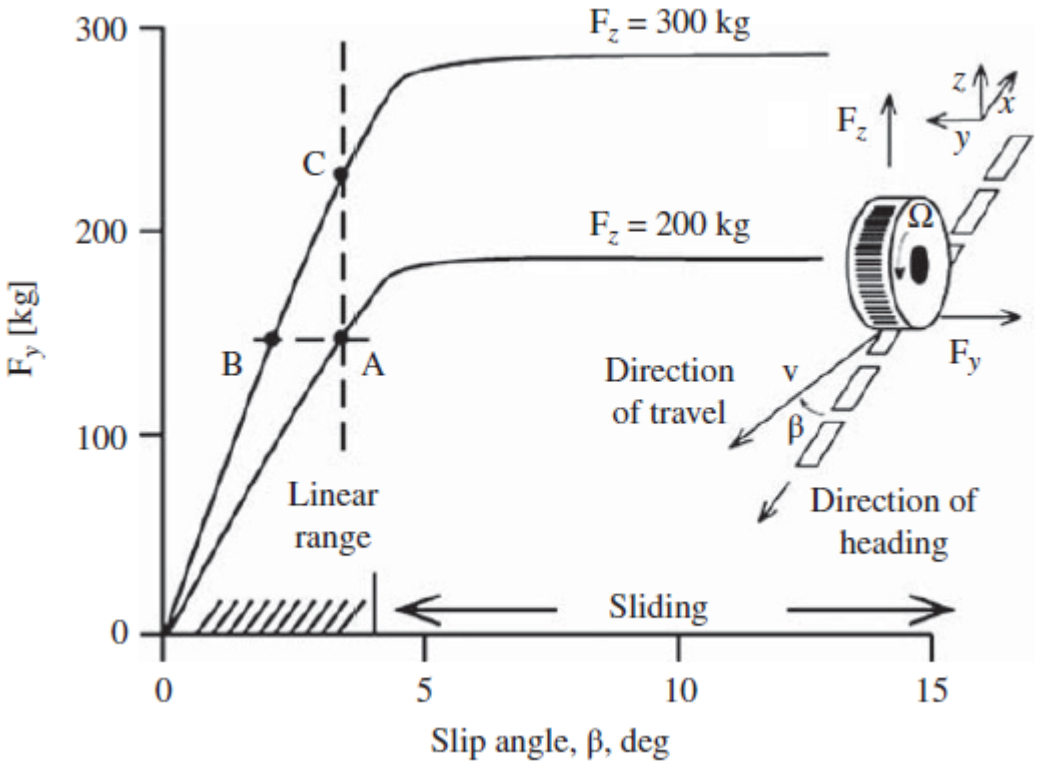

Fig. 3.1.1: $F_y - \beta$ diagram (6)

Increasing the slip angle, the side force F_y initially increases linearly and, for the same β, more downforce generates more side force (points A and C). Furthermore, to generate the same amount of side force, a car with more downforce reaches the same F_y at lower β: that means that the more the downforce a car generates, the less heating and wear on tyres occurs due to friction, and it will preserve its tires for a longer period (points A and B). On the other hand, for maximum performance the largest possible force is sought and then point C represents a condition with the same tire slip as in A, but now the vehicle with the aerodynamic downforce is turning faster.
Another important benefit of creating downforce is to increase the dynamic stability. Let's consider the following figure, schematically representing the forces on a vehicle.

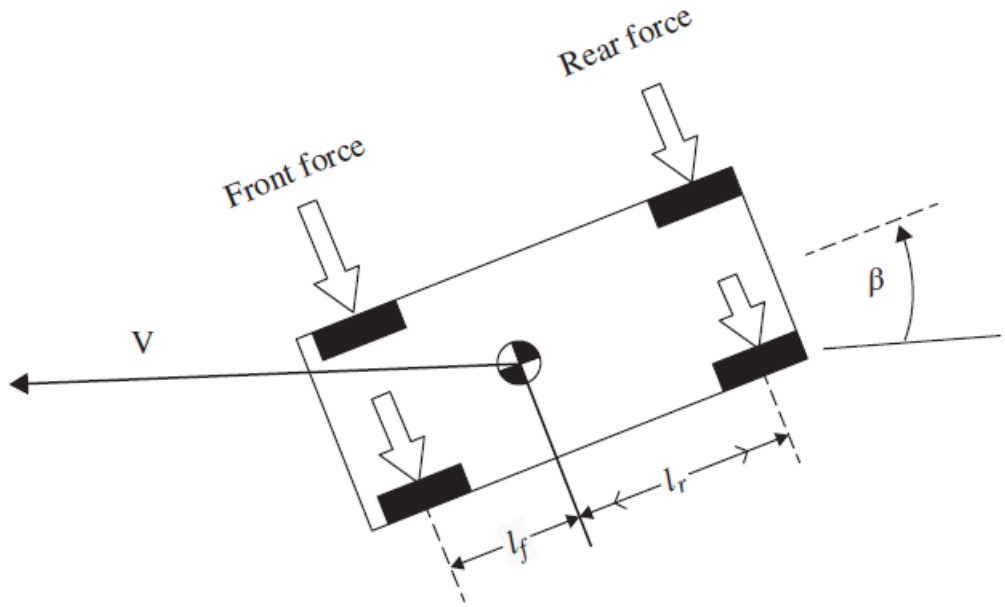

Fig. 3.1.2: Forces on a cornering vehicle (6)

Assuming that the moment around the center of gravity generated by the forces on the rear wheels is greater than the moment generated by the forces on the front ones; the total moment acts reducing the sideslip angle

$$\frac{dM}{d\beta} = -F_r \cdot l_r + F_f \cdot l_f < 0$$

This means the *the vehicle is stable*. Otherwise, if $dM/d\beta > 0$ the vehicle is unstable. During cornering, a statically unstable vehicle tends to oversteer, while the statically stable vehicle will understeer.
The yawing moment can be easily affected by aerodynamic loads. For example, if a vehicle tends to be slightly unstable, the addition of rear downforce can increase the available side force of the rear tires and consequently stabilize the vehicle (and also make it safer to drive). These effects become more important at higher speeds, as in the case of racecars driving close to the tyre maximum friction coefficient

3.1.1 Ground effect

The flow over a body will change when it is close to a boundary, and in case of ground vehicles the streamlines close to the ground are eventually forced to be parallel to the road. This *ground effect* was observed early in the twentieth century during takeoff and landing, when airplanes flying close to the ground experienced increased lift. Consequently, the attached-flow over an airfoil, in ground effect was studied and it was found that the increase in force is present for both positive and negative lifting airfoils.
Clearly, both downforce and drag increase as ground clearance is reduced, but at a very small clearance the trend stops (also in this case, this behaviour is called *stall*). Of course, at a very small ground clearance, the boundary layer in the narrow gap between the airfoil and the ground slows down the flow and stalls the aft section of the airfoil (resulting in a reduction in the downforce). Also, when h = 0, there is no flow under the airfoil.

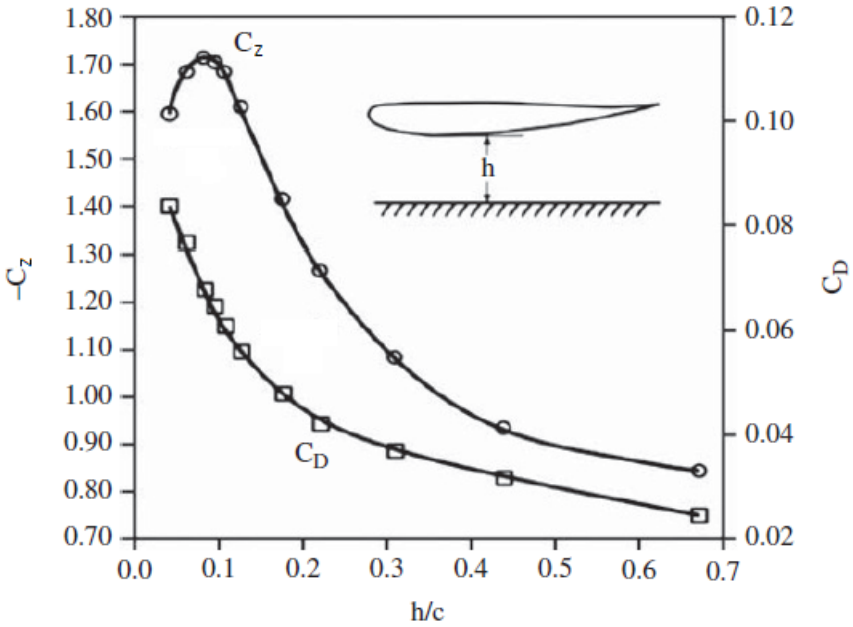

Fig. 3.1.3: Coefficients change over ground clearance (6)

3.1.2 The wing

In many passenger cars, wings, spoilers and other aerodynamic devices are added to increase downforce (or reduce lift). This interaction can be demonstrated when mounting a rear wing to the generic ellipsoid shape as shown in the following figure. When an inverted wing is added at the back, the flow under the ellipsoid accelerates as a result of the lower base pressure (at the back), induced by the wing. The higher speed causes more downforce on the body, apart from the downforce created by the wing itself. Furthermore, on many occasions, the high-speed flow created near the wing partially reattaches the flow on the body, reducing the area of flow separation and then the pressure drag generated by the car. This simple example demonstrates why proper mounting of a rear wing can increase the downforce of a vehicle more than the expected lift of the wing itself.

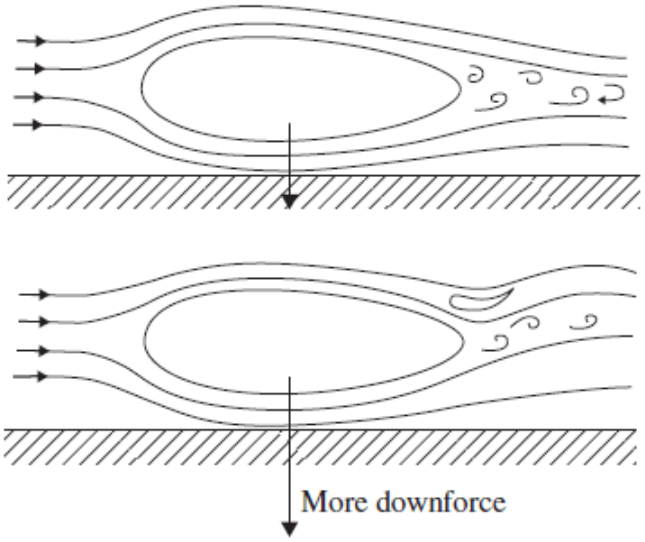

Fig. 3.1.4: Effects of a rear wing (6)

As an aerodynamic device, the wing is a body of highly pecial form, with a rounded front (for subsonic flows) called the *leading edge* and an a sharp end callled the *trailing edge* The wing section is called *airfoil*, formed by a symmetric geometry which is opportunely cambered, as shown in the following picture

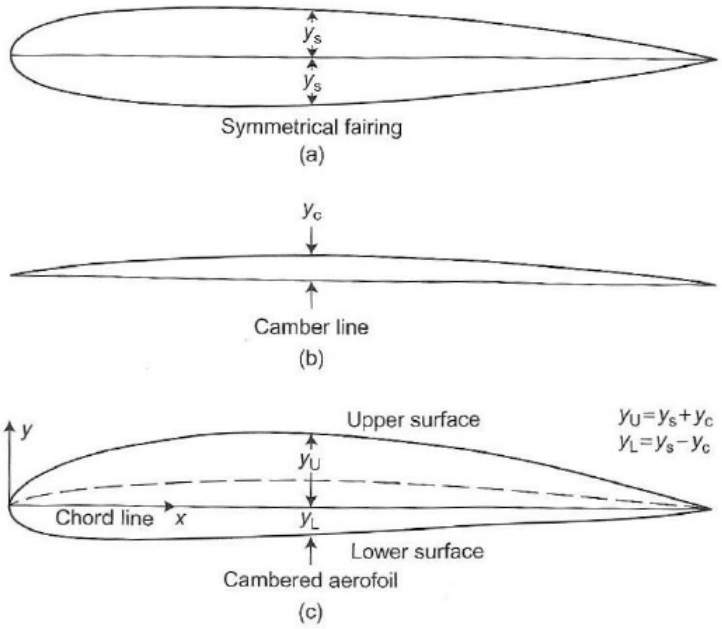

Fig. 3.1.5: The airfoil (12)

The finite wing is made by the extrusion of the airfoil along and axis forming a 3D body. The characteristics of a finite wing are:

- The plan form;
- The length L from a wing tip to the other
- plan surface aera S;
- the *mean geometric chord* $c_n = \frac{S}{L}$;
- The *aerodynamic twist angle*, the rotation of the airfoil along the wing;
- The *tapering angle*, the ratio between the tip chord and the root chord;
- The *aspect ratio* $\lambda = \frac{L}{c_n}$;

- The *dihedral angle*, the angle formed between the horizontal plane and the plane passing through the root and tip chords of the wing profiles. This has little application in motorsport, because of the regulation restrictions.

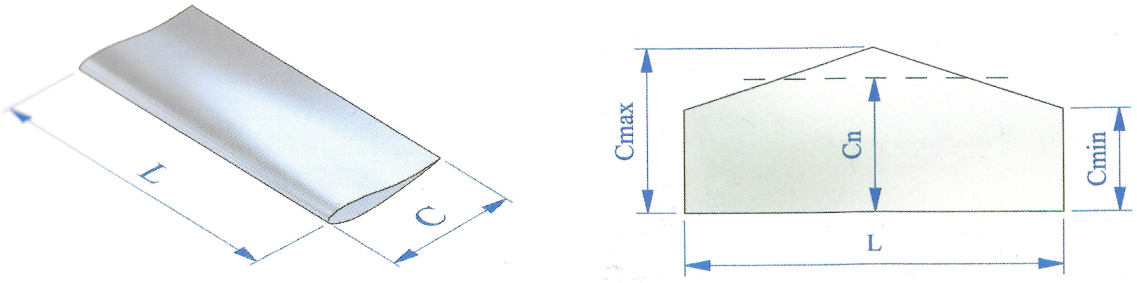

Fig. 3.1.6: The 3D wing (13)

The performances of an airfoil (and then of a wing), are represented in terms of downforce, aerodynamic drag and pitching moment (or their coefficients) at different angles of attack, functions of the pressure distribution along the airfoil or a wing.

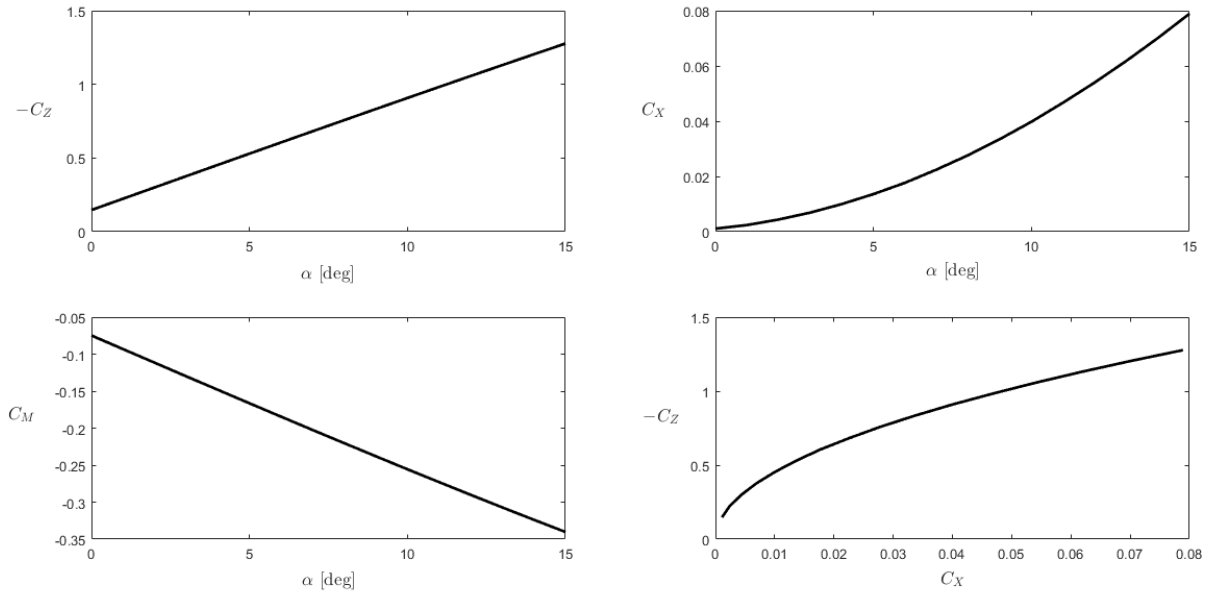

Fig. 3.1.7: Performance diagrams of a wing

3.1.3 The diffuser

Let's consider a slender flat-plate at an angle of attack. The main aspect of this flow field is the formation of two concentrated side edge vortices that dominate the nearby flow field. These two vortices induce high velocity on the plate (under the vortices), creating strong suction forces, which considerably increase the lift of the flat-plate wing. When introducing a slanted surface to the lower aft section of the body a similar behaviour can be expected. This principle can be utilized for racecars, and for moderate slant angles (less than 15°) an increase in the downforce is observed. In the racing circuits, such upward deflections of the vehicle lower surface are usually called *diffusers*. However, a far more interesting case is when two side plates are added to create an underbody tunnel, sometimes called *Venturi*, tunnels in which air speeds up and its pressure decreases according to Bernoulli's law, increasing the difference of pressure between the upper and the lower part of the care, generating downforce. This geometry can generate very large values of negative lift, with only a moderate increase in drag. Furthermore, the downforce created by this geometry increases with smaller ground clearances.

Fig. 3.1.8: The rear diffuser of a rally car

3.1.4 Aerodynamical devices on the front end

In many racing cars except *monoposti*, many types of aerodynamical solution have been developed:

- *Splitter*: a device almost parallel to the flow which is meant to create downforce and split the airflow, from the one which has to go in the upper part of the vehicle and the one who is sent beneath it;
- *Dam*: it is a vertical barrier with the aim to stop the flow and to create a low pressure region under the front end of the car due to the acceleration of the flow; obviously, this barrier slightly increases aerodynamic drag;
- *Front diffuser*: it is designed to create part of the front downforce and to provide a more organized flow inside the wheel arch

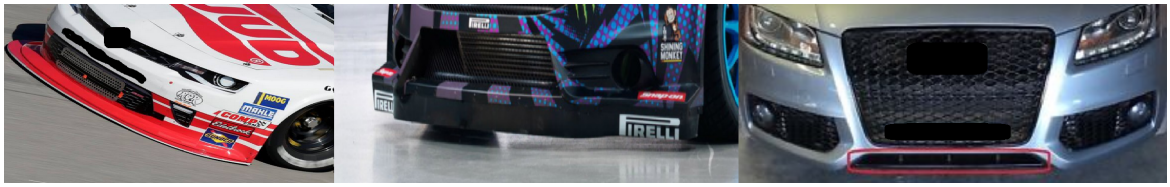

Fig. 3.1.9: From left to right: the splitter, the dam and the frontal diffuser

Chapter 4

Introduction to Computational Fluid Dynamics

Computational Fluid Dynamics is the art of replacing partial differential equation systems by a set of algebraic equations which can be solved using digital computers. For a proper numerical simulation using CFD techniques, it provides a qualitative and quantitative prediction of fluid flows using:

- Mathematical modelling;
- Numerical methods;
- Software tools for pre- and postprocessing;

CFD enables scientists and engineers to perform numerical experiments without the need of using wind tunnels and measurement instruments. The advantages of CFD simulations over experimental tests is:

- Lower cost;
- Faster speed in obtaining results;

However, the results of a CFD simulation are never completely reliable due to numerical approximation and too much guessing, and the accuracy of the results is limited by the available computing power.

4.1 The Finite Volume Method (FMV) and the mesh grid

The Finite Volume Method is a numerical technique that transforms partial differential equations representing conservation laws over differential volumes into discrete algebraic equations over finite volumes (called *cells*). The geometric domain is splitted into non-overlapping finite volume cells in which algebraic equations are solved. Some tems in the conservation laws are turned into face fluxes and evaluated at the finite volume faces. Because the flux entering a given volume is identical to that leaving the adjacent volume, the FMV is strictly conservative, and that's why this method is the preferred method in CFD.

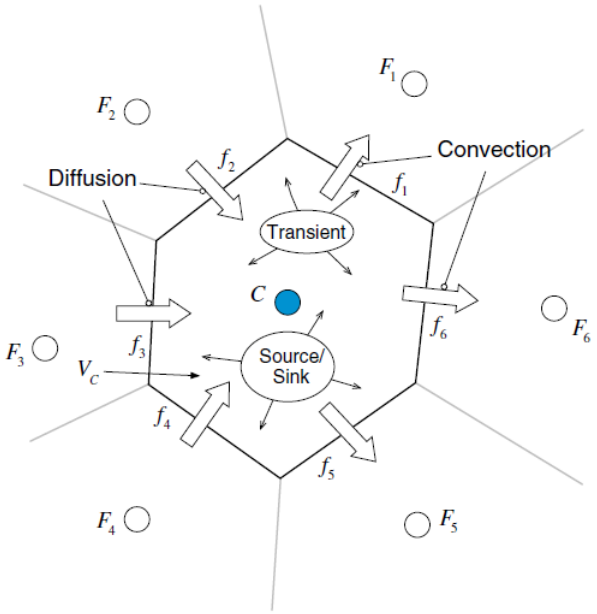

Fig. 4.1.1: Conservation law in a cell (11)

The fluid properties are solved for every cell in the computational domain, giving the solution at che centre of every cell of the numerical grid (called *mesh*). The latest figure shows exahedral cells; however, fluid domain can be split into different types of cells (triangular cells, quadrilateral cells). Also, the mesh grid can be structured or unstructured, as shown in the figure below.

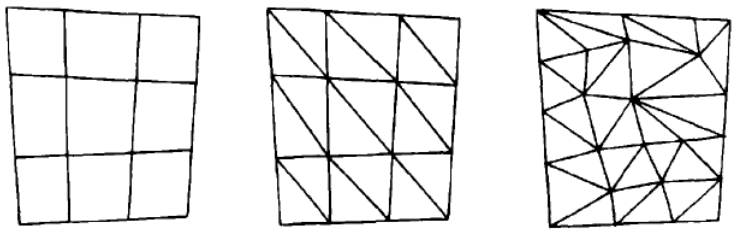

Fig. 4.1.2: Example of different types of mesh over the same domain (9)

4.2 Boundary conditions

The evaluation of the fluxes at the faces of a domain boundary does not require, in general, a profile assumption. Rather a direct substitution is usually performed. The type of boundary conditions are numerous. However, two of the most widely used ones for general scalars are the Dirichlet and the Neumann boundary conditions. In mathematical terms these are respectively a value specified (Dirichlet) and a flux specified (Neumann) boundary condition. Considering a fluid domain Ω and its boundary $\partial\Omega$, the Dirichlet boundary condition for a generic variable ϕ can be expressed as:

$$\int_{\partial\Omega} \phi \, d\Omega = k$$

The Neumann boundary condition, instead, has the form

$$\int_{\partial\Omega} \frac{\partial\phi}{\partial n} \, d\Omega = k$$

where k is a constant value, and n is the vector normal to the boundary. In FVM, every boundary cell has its own boundary condition.
In Computational Fluid Dynamics, boundary conditions are found:

- On the external boundary of the computational fluid domain (*far field condition*);
- On surfaces representing walls (*wall condition*);
- In case of internal sources/sinks of mass, momentum or energy.

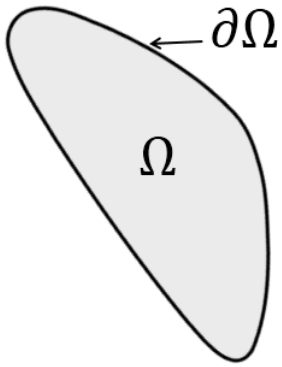

Fig. 4.2.1: Representation of a computational domain and its boundary

4.3 Space and time discretization and time solvers

Navier Stokes Equations are highly non-linear differential equations, thus it's necessary to evaluate every temporal and spatial derivative they contain. In Computational Fluid Dynamics, given the initial conditions, the solver computes:

- Temporal derivatives for unsteady problems;
- First spatial derivatives between adjacent cell midpoints for convective fluxes.
- Second spatial derivatives between adjacent cell midpoints for diffusive fluxes;

The *order of accuracy* of the numerical scheme is defined by how those derivatives are approximated: the higher is the temporal or spatial accuracy order, the slower will be the simulation of a fluid dynamic problem.

The discretization of the time derivatives also determines:

- *Explicit methods*: the temporal derivative is evaluated using the unknown value of the variable at the actual time step and the values of the variables in the previous ones. This temporal scheme shows its stability only if the Courant-Friedichs-Levy condition (know as *CFL condition*) is satisfied, that reflects itself, after defining the meshgrid, on a low and limited time step;
- *Implicit methods*: the temporal derivative is computed using the values of a variable at the actual and following time steps, which

are unknown. The equation must be solved iteratively, using inner iterations to make the solution converge before passing to the following time step. This is a always stable and solid numerical scheme and doesn't need any further condition but it is computationally much more expensive than explicit methods at the same order of accuracy.

Here are the following properties that a good numerical solution method must have:

- *Consistency*: The discretization should become exact (no truncation errors) as the grid spacing tends to zero;
- *Stability*: The numerical scheme doesn't magnify the errors that appear during the simulation;
- *Convergence*: The solution of the discretized equations must tend to the exact solution of the analytical Navier-Stokes equations as the grid spacing tends to zero;
- *Conservation*: Since the equations to be solved are conservation laws, the numerical scheme should also respect these laws, both locally and globally;
- *Boundedness*: Numerical solutions should lie within proper bounds that depend on the particular variable and on the particular equation
- *Reliazability*: Models of phenomena that are too complex to treat directly should be designed to guarantee physically realistic solutions;
- *Accuracy*: Numerical solutions of fluid flow are only approximate solutions. They always include three kinds of systematic errors (modelling errors, discretization errors and iteration errors).

In the end, a CFD simulation can be summarized as it follows:

1. Setting up the physics of the problem (defining the set of equations used to solve the numerical simulation)
2. Choice of the computational fluid domain;
3. Creation of the mesh grid
4. Definition of the boundary and initial conditions;
5. Choice of the accuracy of spatial discretization, accuracy of the temporal discretization and resolution schemes for time dependent problems;
6. Simulation process;
7. Post processing (validation of the obtained results).

Chapter 5

Montecarlo EVO model analysis

This chapter deals with the preparation of the geometry, the setting up of the mesh of the computational fluid domain and the performance analysis. The Montecarlo EVO model is an evolution of the supercar *Montecarlo-BRC W12* created by a previous thesis work in AGOM.

Fig. 5.0.1: The Montecarlo-BRC W12 model and its evolution

5.1 The preparation of the geometry

To prepare the geometry for the aerodynamic simulation, the supercar has been opened in *SolidWorks* CAD software. The external body of the car was formerly created with a surface modelling software.

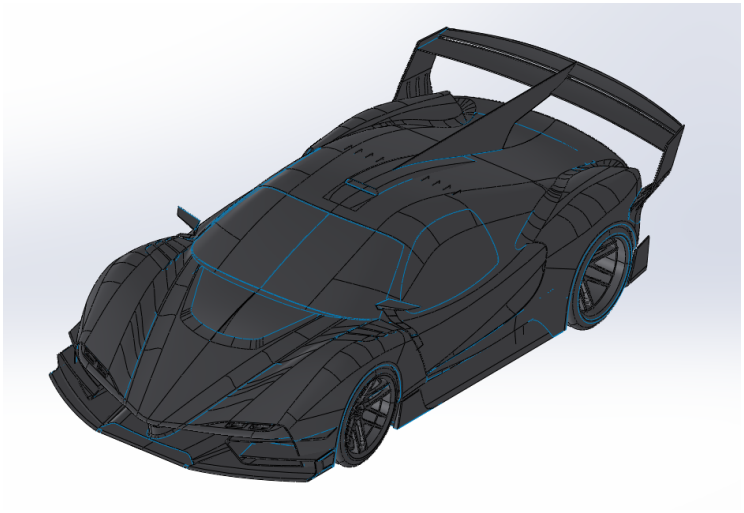

(a) Front car isometric view

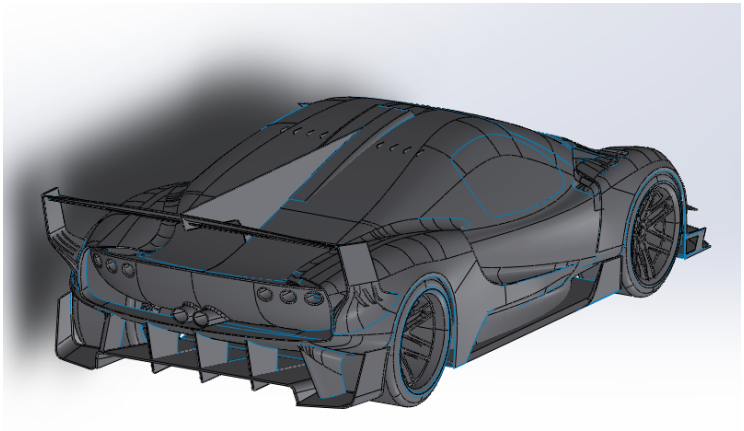

(b) Rear car isometric view

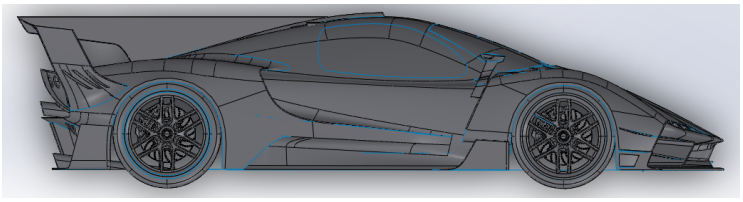

(c) Side car view

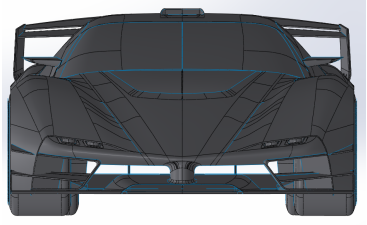

(d) Front car view

Fig. 5.1.1: Overview of the car

The two important issues of the preparation of the geometry are:

- An **enclosed volume**, to subtract from the computational fluid domain block, which represents the wind tunnel. Every opening in the car (diffuser, hood, muffler,...) has to be closed, adding further boundary conditions in those regions;
- A **correct and clean geometry**; an incorrect geometry can cause the surface mesher to fail or give an invalid solution.

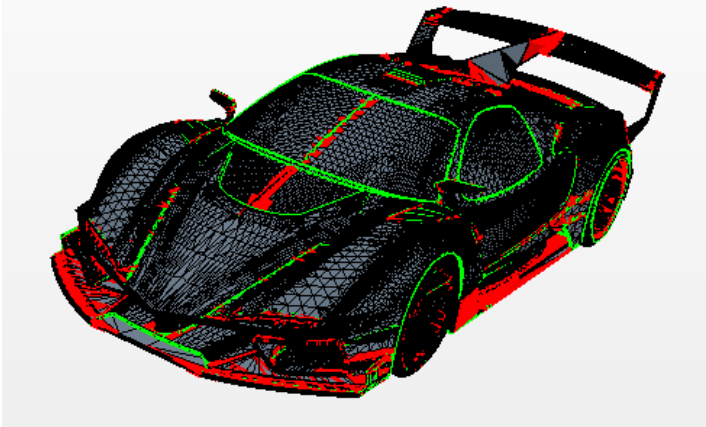

(a) Front car isometric view

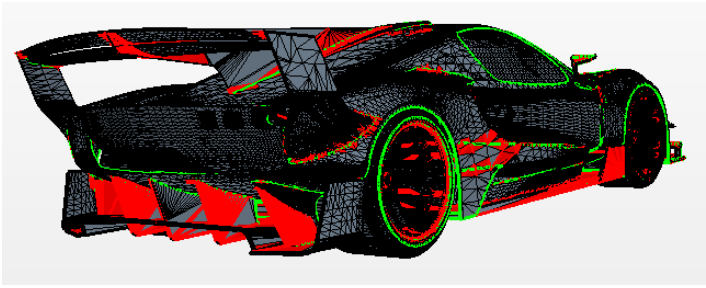

(b) Rear car isometric view

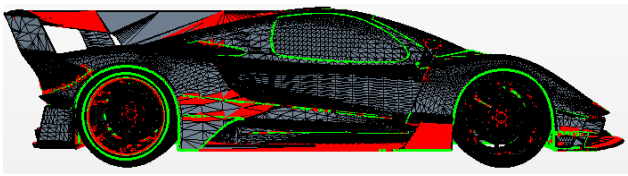

(c) Side car view

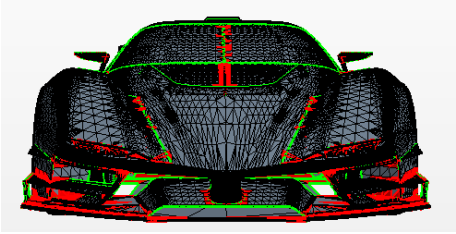

(d) Front car view

Fig. 5.1.2: Geometry errors

where:

- The 35.092 pierced faces represent the faces that pass through the other ones;
- The 46.031 free edges represent the edges of the cells which are not shared with other cells and identify free zero-thickened surfaces;
- The 32 non-manifold edges and 9 non-manifold vertices represent those edges and vertices who are shared between more than two faces

Using both the *SolidWorks* and *Star-CCM+* software a closed and clean geometry is obtained, using a simplified geometry for the wheels for the preliminary desing and creating the wheel's hubs having a diameter equal to $\phi_{hub} = 10mm$.

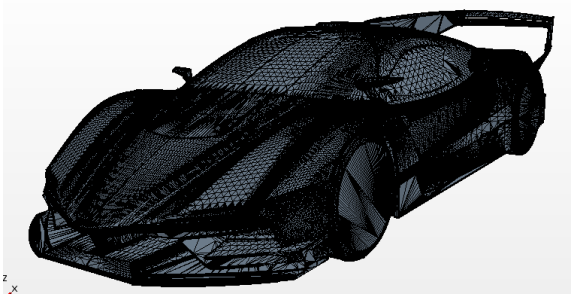

(a) Front car isometric view

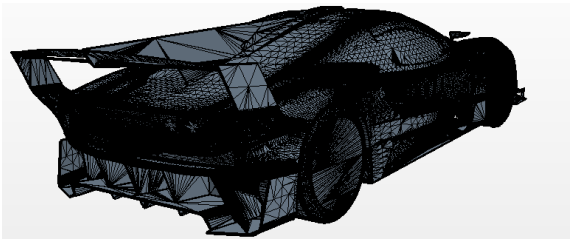

(b) Rear car isometric view

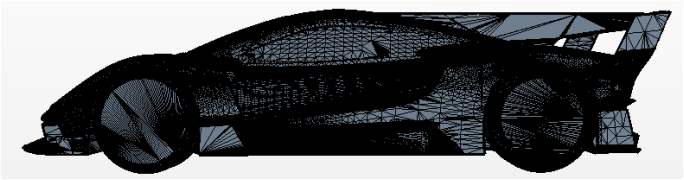

(c) Side car view

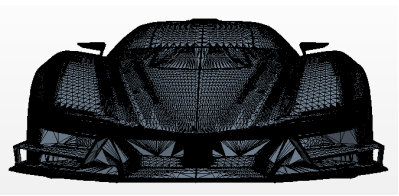

(d) Front car view

Fig. 5.1.3: The closed and clean car geometry

5.2 Definition of the physics continuum

The physics continuum deals with the preparation of the faced physic problem.
As the *Steve portal's Vehicle external aero tutorials* suggest, the chosen options for the preliminar aerodynamic study of the Montecarlo EVo model are the following:

- Three dimensional flow;
- Steady state flow;
- Gas with constant density $\rho_{air} = 1.225 Kg/m^3$;
- Segregated model for the resolution of the Navier Stokes equations in every cell center of the mesh. This computational process solves each of the momentum equations in turn, one for each dimension;
- Reynolds Averaged Navier Stokes equations (RANS) to solve the turbulence, using the $k - \omega$ turbulence model, which is a two-equation model that solves transport equations for the turbulent kinetic energy k and the specific dissipation rate ω the dissipation rate per unit turbulent kinetic energy in order to determine the turbulent eddy viscosity;
- All y^+ wall treatment for the turbulent boundary layer;
- Cell quality remediation model to optimize the solving of the equations inside bad quality mesh cells.

The physics continuum needs to know the reference absolute pressure relative to which other pressures are defined. The reference pressure is set as $p_\infty = 101325\ Pa$.
At least, the resolution of differential equations needs the initial conditions: they will be the steady velocity of the car.

5.3 The setting up of the mesh

Now that the geometry has been prepared, the computational fluid domain can be created using the best practice sizes by the *Simcenter Steve Portal's vehicle external aero tutorials*. For the aim of the longitudinal aerodynamic analysis, the simulation will be processed only using half a car.
Starting with the original dimensions of the car equal to:

- 2.0 m wide;
- 1.2 m high;
- 4.5 m long.

The computational fluid domain sizes have to be:

- 5 times the length of the car for the upstream;
- 10 times the length of the car for the downstream;
- 5 times the height of the car for the upper face;
- 5 times the width of the car for the side face.

The overall dimensions of the computational fluid domain block are, then:

- 10 m wide;
- 6 m high;
- 72 m long.

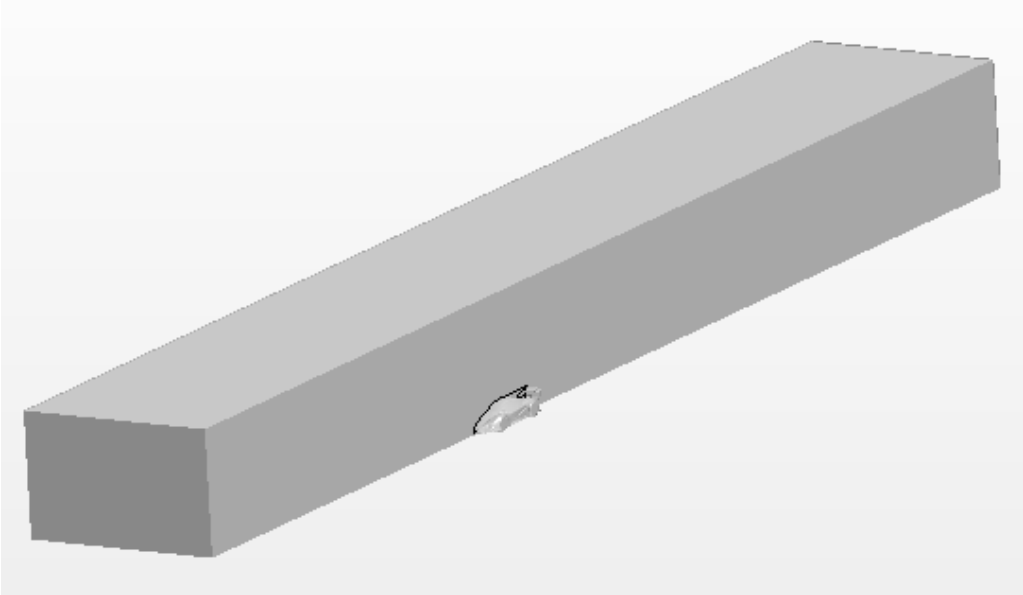

(a) Isometric view

(b) Side view

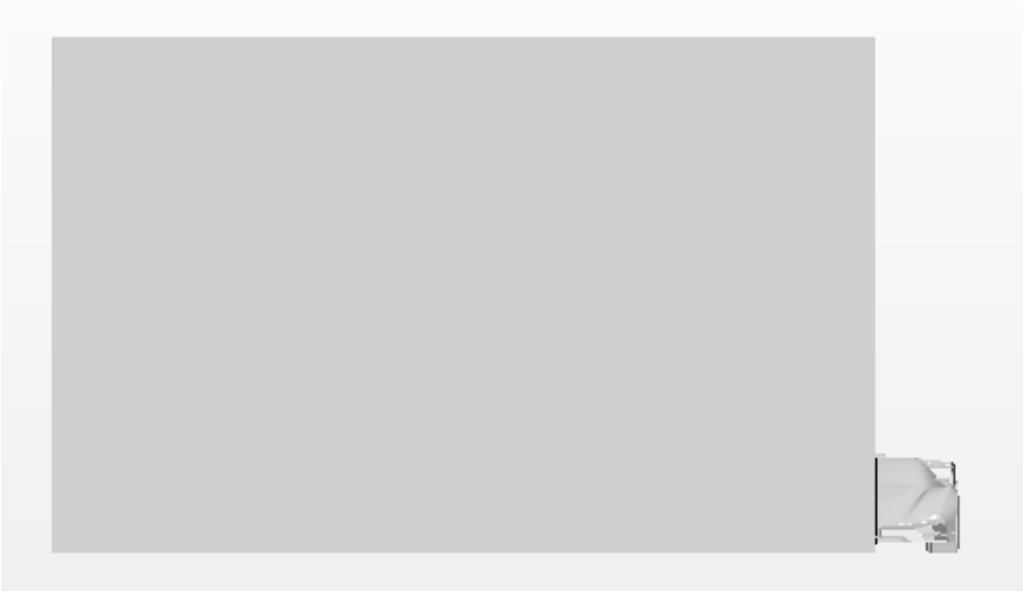

(c) Front view

Fig. 5.3.1: The car and the computational fluid domain block

The following step deals with the creation of a suitable mesh. After extracting the car volume from the computational fluid domain block via Boolean subtract operation and running a first meshing operation. To make the subtract operation success, the computational domain block was modeled cutting slightly the tyres, to avoid singularities. This operation can also be seen as the reproduction of the brush model theory of the vehicle dynamics.
Setting:

- Trimmed cells (the best choice cell type for flows having a main direction);
- Base size = 0.05 m;
- External volume size = 1.0 m;
- Local refinements on car curvatures (such as spoilers, roof diffuser, spoilers' pillar and others)

the first result can be seen in the following picture, where the orange regions in the mesh scene represent the car openings (and closed to obtain a closed volume) and they are set as regions with a *pressure outlet condition.*

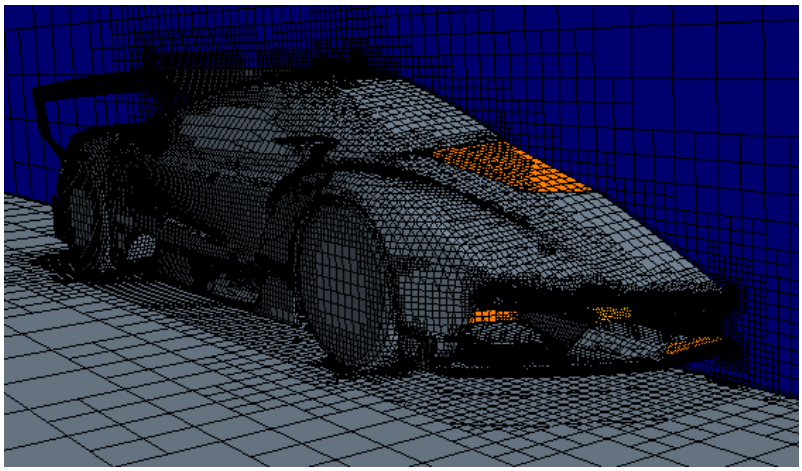

(a) The former mesh

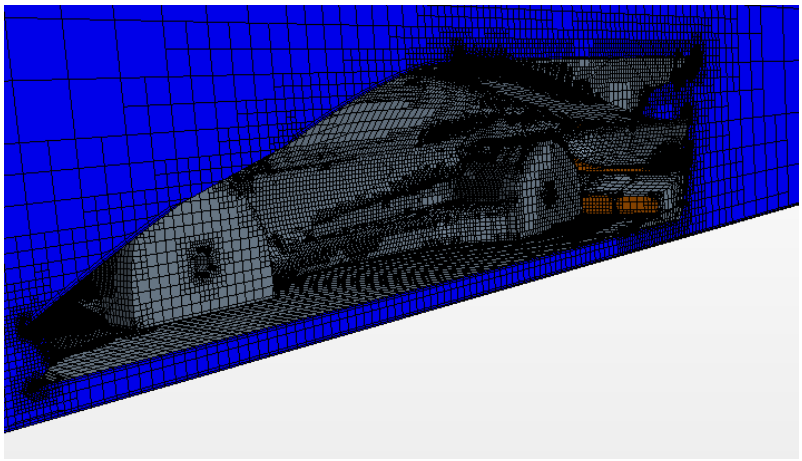

(b) The car subtraction

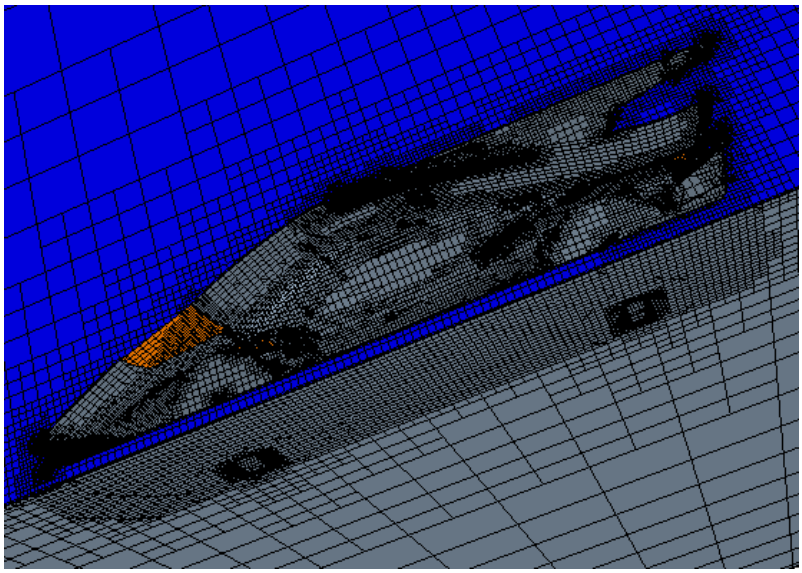

(c) The intersection between the tyres and computational fluid domain block

Fig. 5.3.2: The computational fluid domain and the subtraction of the car

This first mesh, having 2.8 millions of cells, has to be further refined, changing its base size and the external volume mesh. The following table shows the new mesh operation launched, combining different sizes of base size and external size. The highlighted row in the following table show the chosen combination for the further mesh refinements.

Base size [m]	**External volume cell size** [m]	**Milions of cells**
0,04	2	3.2
0.04	1.5	3.2
0.04	1	3.2
0,025	2	5.8
0.025	1.5	6.0
0.025	1	5.8
0,015	2	11.0
0.015	1.5	11.0
0.015	1	11.3
0.01	2	21.7

Table 5.1: Meshing campaign - variation of base size and external volume cell size

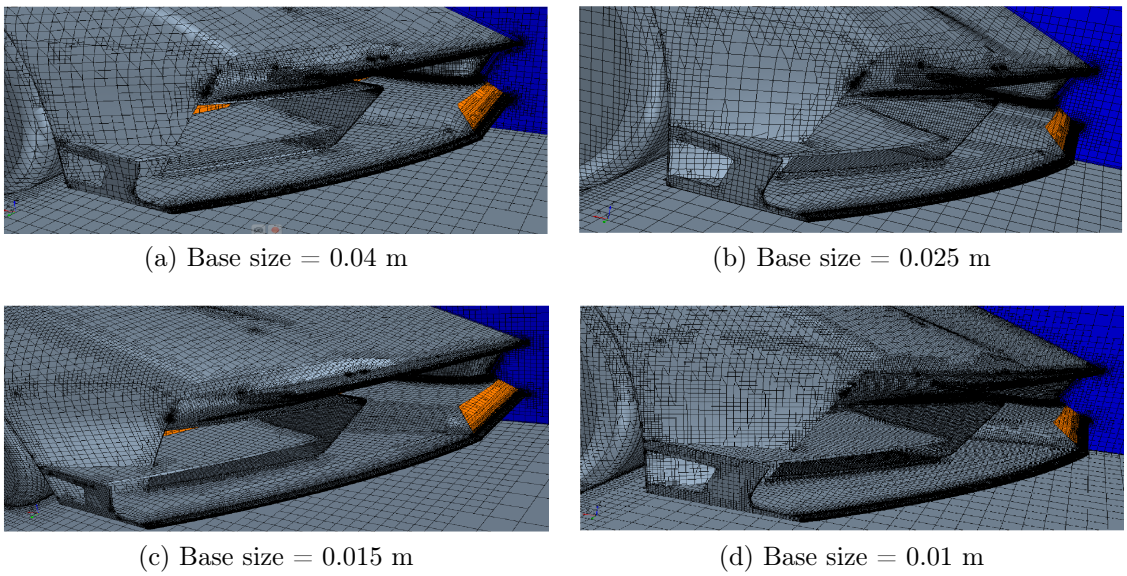

(a) Base size = 0.04 m

(b) Base size = 0.025 m

(c) Base size = 0.015 m

(d) Base size = 0.01 m

Fig. 5.3.3: Comparison of the front car's mesh

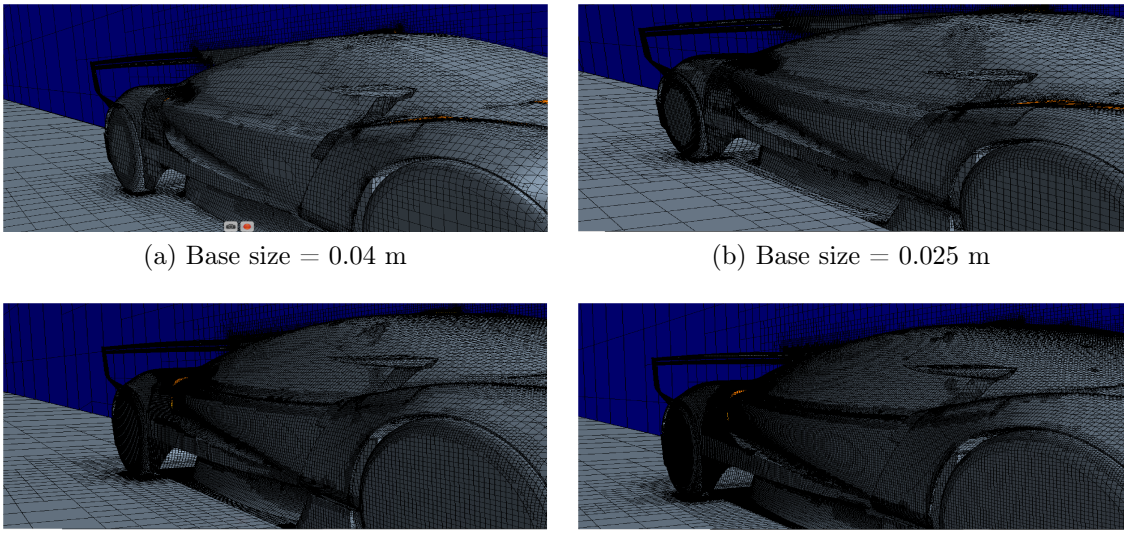

(a) Base size = 0.04 m

(b) Base size = 0.025 m

(c) Base size = 0.015 m

(d) Base size = 0.01 m

Fig. 5.3.4: Comparison of the side car's mesh

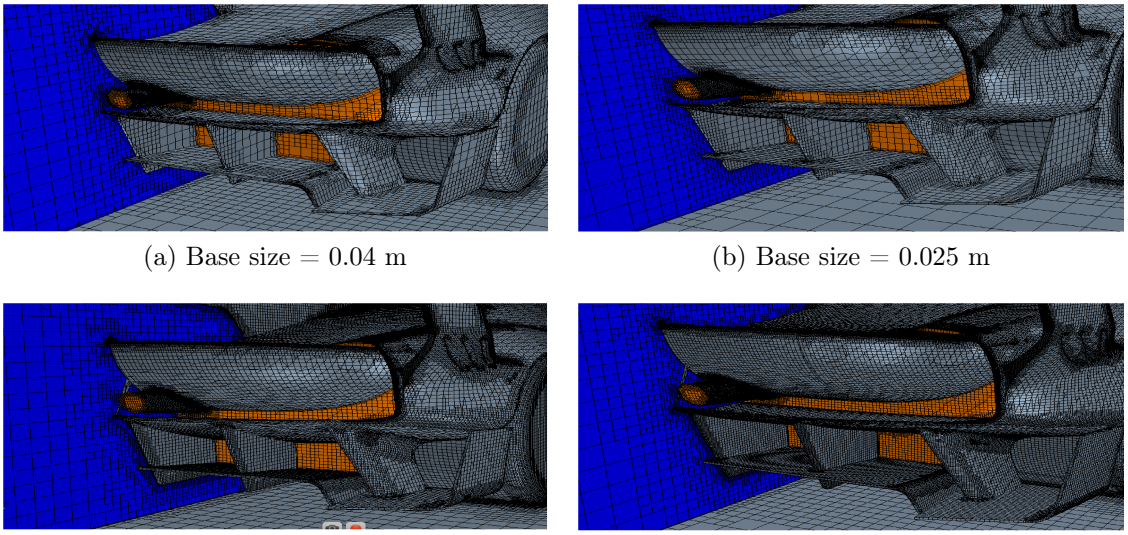

(a) Base size = 0.04 m

(b) Base size = 0.025 m

(c) Base size = 0.015 m

(d) Base size = 0.01 m

Fig. 5.3.5: Comparison of the rear car's mesh

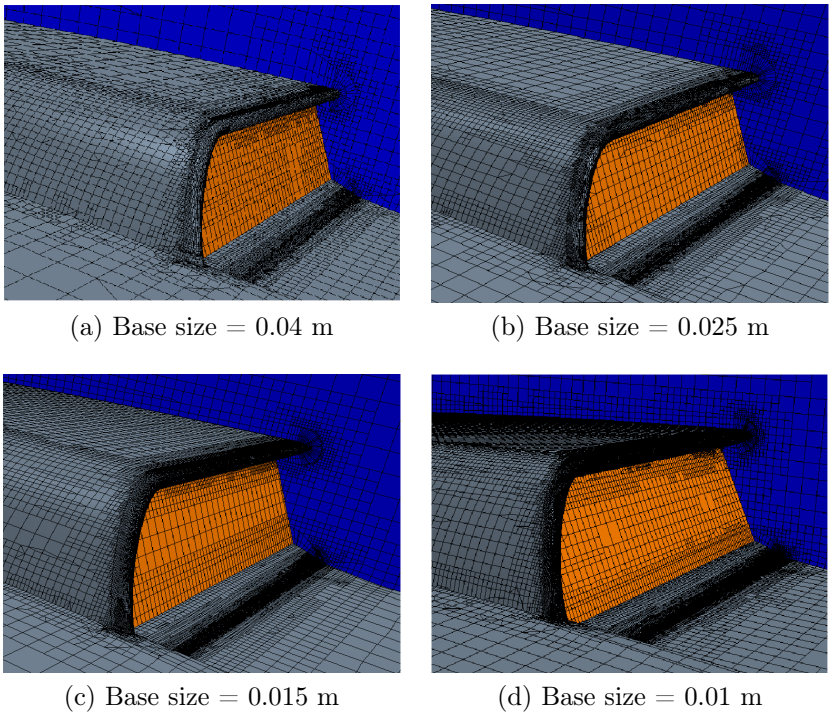

(a) Base size = 0.04 m (b) Base size = 0.025 m

(c) Base size = 0.015 m (d) Base size = 0.01 m

Fig. 5.3.6: Comparison of the roof diffuser's mesh

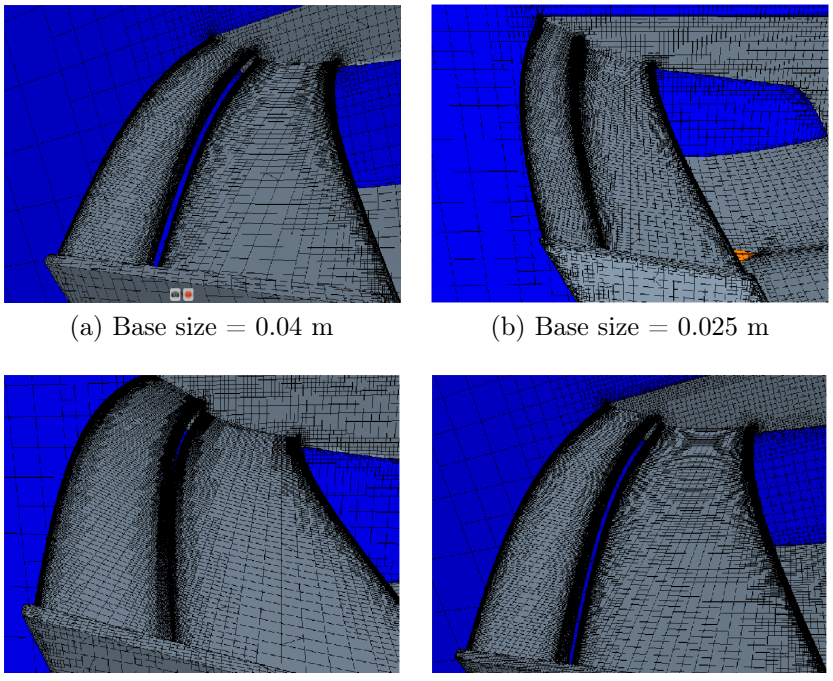

(a) Base size = 0.04 m (b) Base size = 0.025 m

(c) Base size = 0.015 m (d) Base size = 0.01 m

Fig. 5.3.7: Comparison of spoilers' mesh

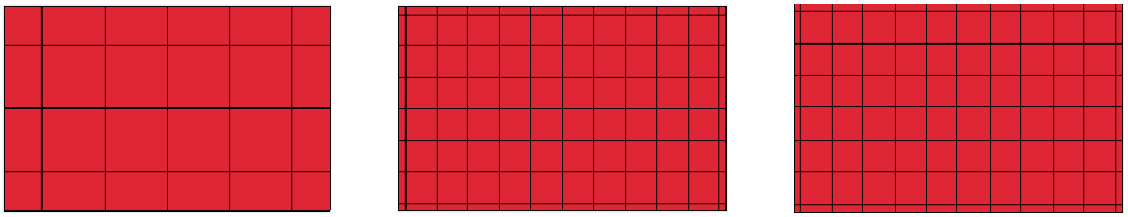

(a) Ext. size = 2.0 m (b) Ext. size = 1.5 m (c) Ext. size = 1.0 m

Fig. 5.3.8: Comparison of front external mesh

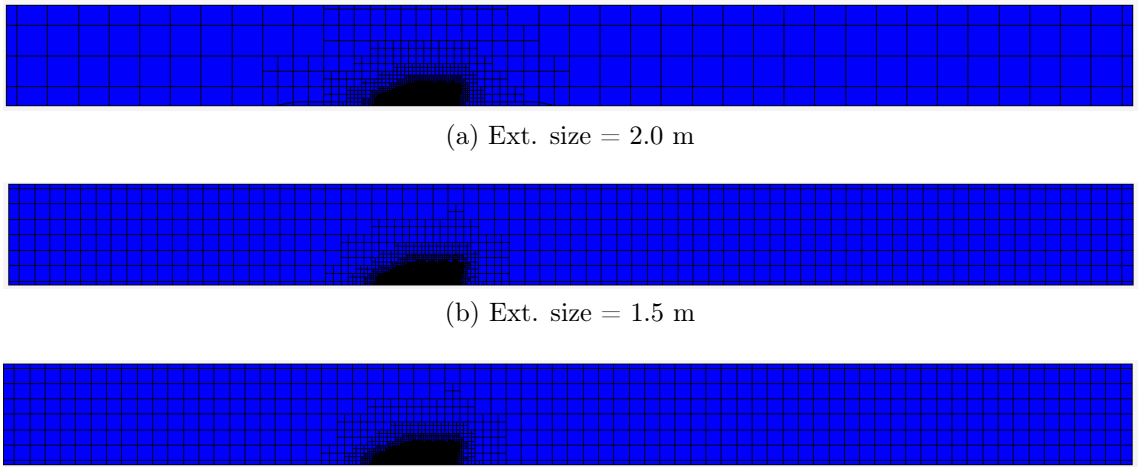

(a) Ext. size = 2.0 m

(b) Ext. size = 1.5 m

(c) Ext. size = 1.0 m

Fig. 5.3.9: Comparison of side external mesh

The next step in the mesh creation deals with the volumetric refinements, which are used:

- For the stagnation points on the car;
- For the below car;
- For the wake.

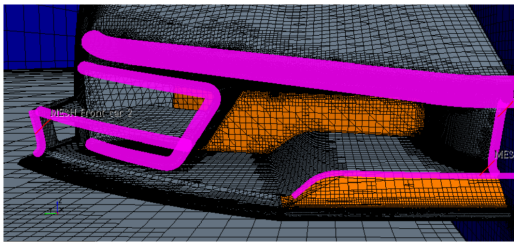

(a) Front car volumetric controls

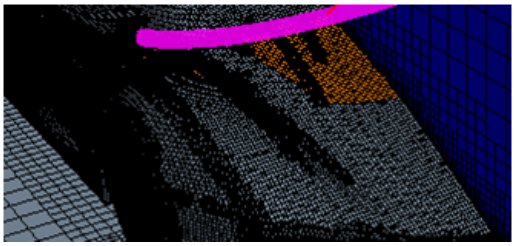

(b) Hood-windshield volumetric control

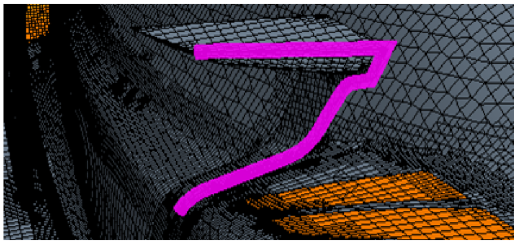

(c) Mirror volumetric control

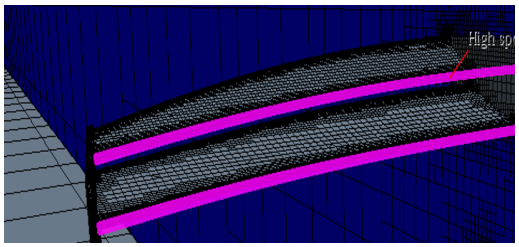

(d) Spoilers volumetric control

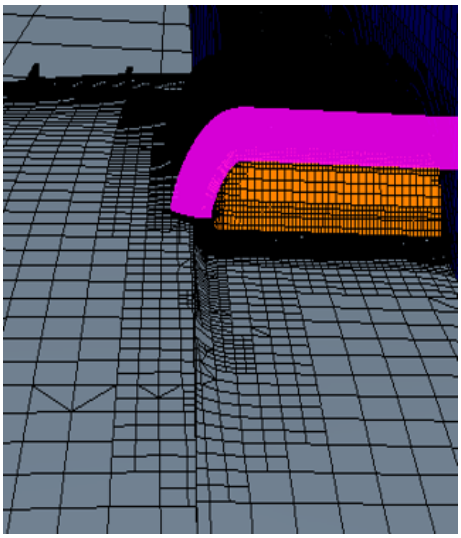

(e) Diffuser volumetric control

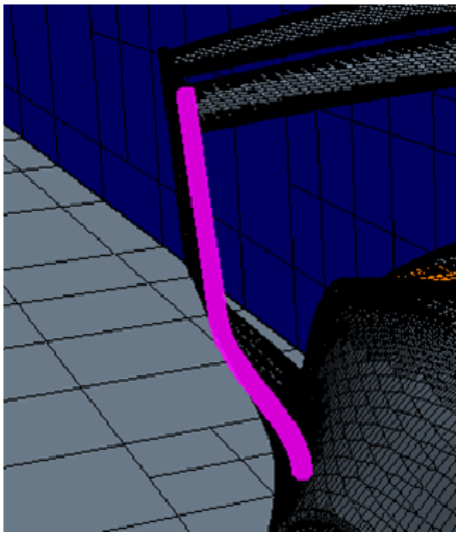

(f) Spoiler's pillar volumetric control

Fig. 5.3.10: Volumetric controls at the stagnation points of the car

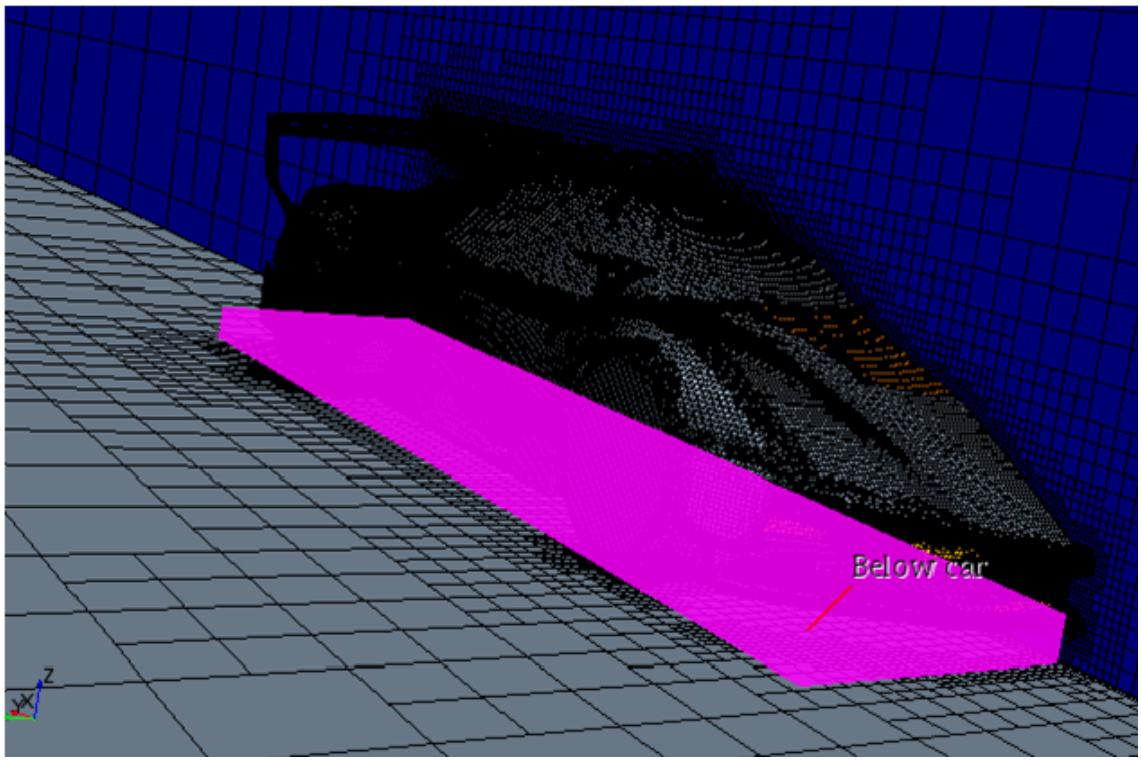

(a) The below car volumetric control

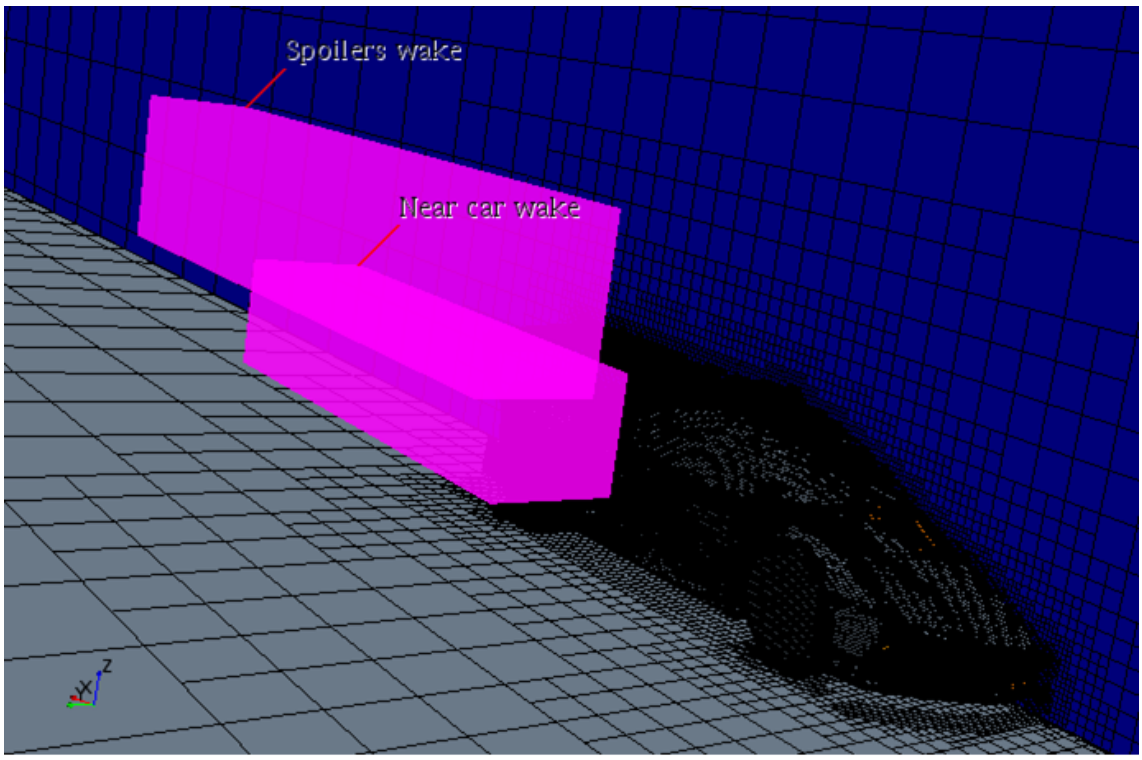

(b) The wake volumetric controls

Fig. 5.3.11: The volumetric control blocks

Like the previous step, different values of mesh refinement for these volumes are chosen. The mesh operations processed are shown in the following table.

Stagnation points refinements [% B.s.]	**Underboby and wake refinement** [% B.s.]	**Millions of cells**
70	50	12.6
70	30	16.7
70	20	19.2
50	50	12.4
50	30	16.7
50	20	19.2
10	50	12.9
10	30	16.8
10	20	19.3

Table 5.2: Meshing campaign - size variation of stagnation point's refinement and wake and underbody blocks

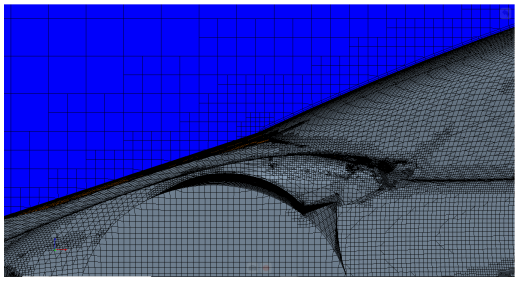

(a) Refinement at the 70% of the base size

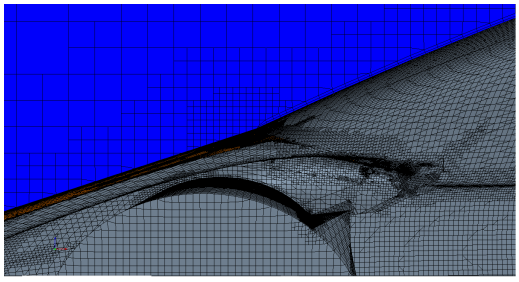

(b) Refinement at the 50% of the base size

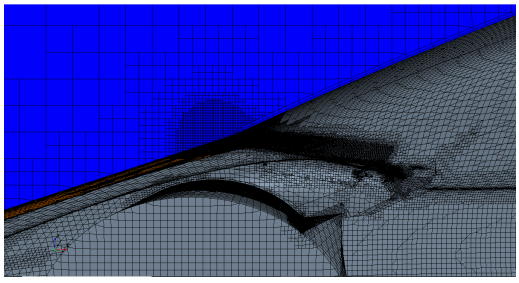

(c) Refinement at the 10% of the base size

Fig. 5.3.12: Stagnation points refinement (hood-windshield intersection example)

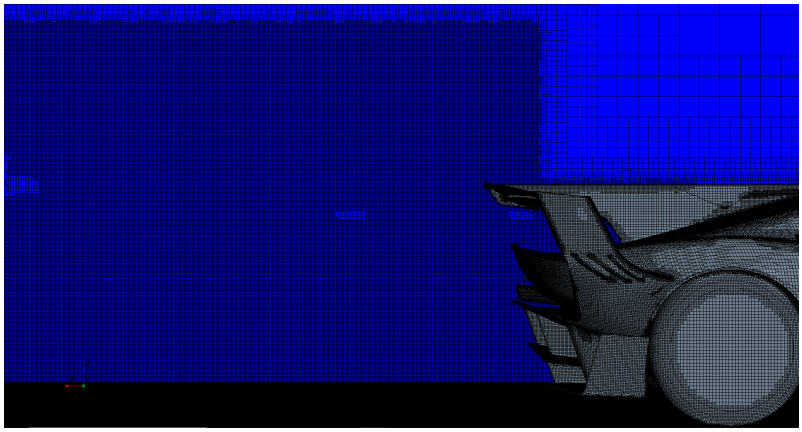

(a) Refinement at the 50% of the base size

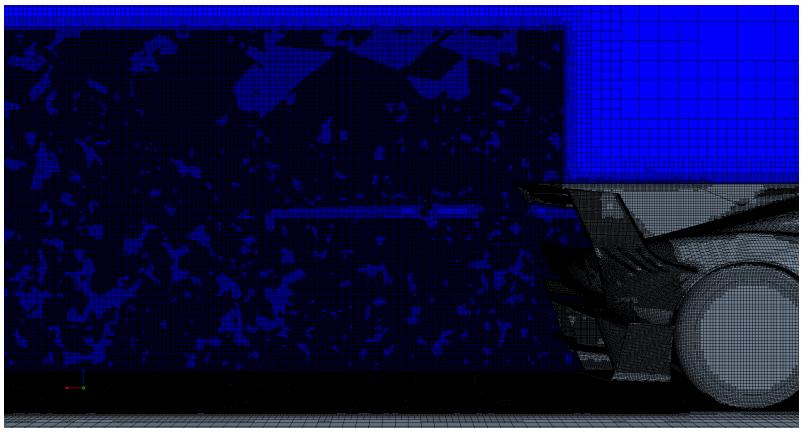

(b) Refinement at the 30% of the base size

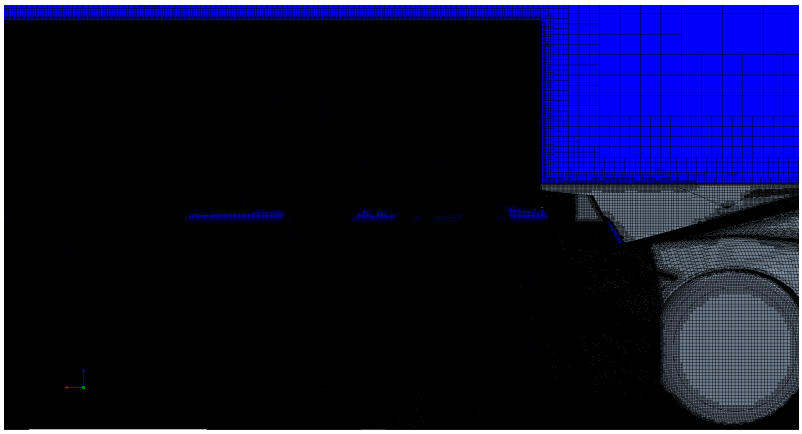

(c) Refinement at the 20% of the base size

Fig. 5.3.13: Wake and underbody refinement

Other refinement are now needed. To evaluate the flow field around the car body, two refinement blocks around the car and the wake have been created, respectively called *Near car 1* and *Near car 2* blocks.

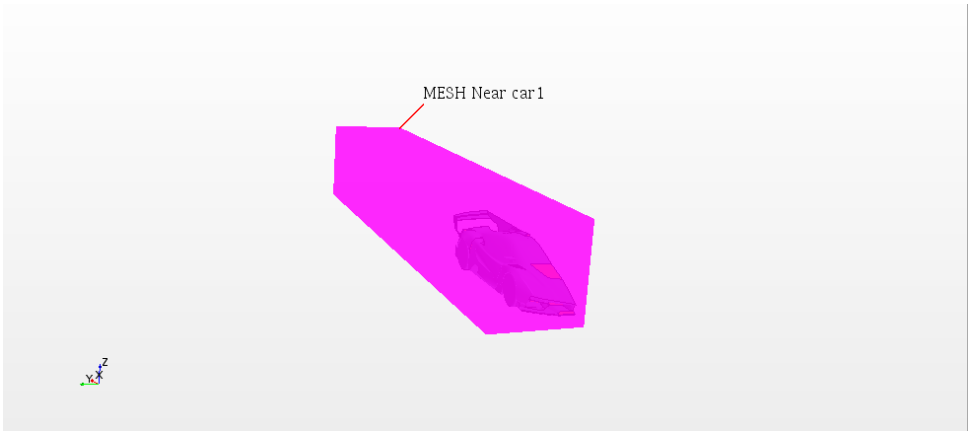

(a) *Near car 1* block

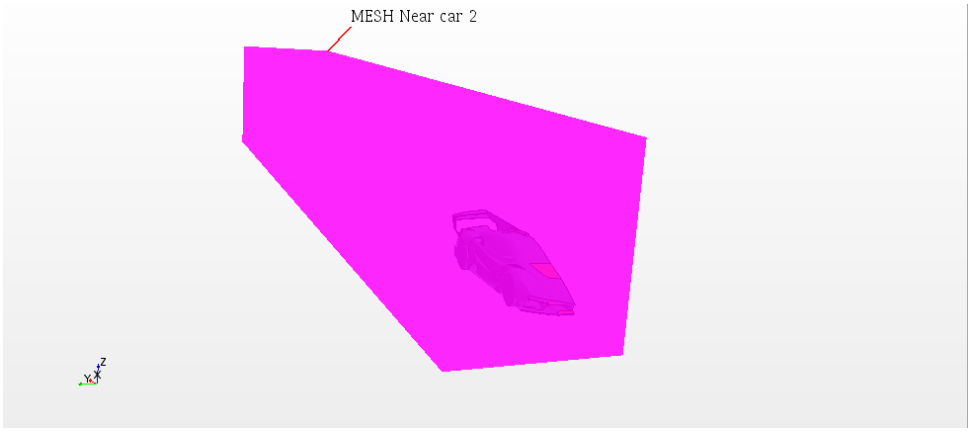

(b) *Near car 2* block

Fig. 5.3.14: Refinement blocks around the car

Defining the near car blocks' cells as a percentage of the base size, the following mesh operations have been set.

- Near car 1 = 200% of the Base Size;
- Near car 2 = 500% of the Base Size;

The last step of the setting up of the mesh deals with the improvement of the mesh and the meshing process of the prism layer for the boundary layer capture. As the best practice of automotive aerodynamics in the *Steve Portal* suggests, the first adimensional distance of the first centroid of the prism layer from the car body, the *wall* y^+, has to be

$$Wall\ y^+ < 5$$

for most of the car. This is the *Low* y^+ wall treatment approach, which is included in the *all* y^+ *wall treatment model* chosen in the setting up of the physics.
The aerodynamic simulation on the Montecarlo EVO model will be run at different velocities, starting from 100 Km/h (from which aerodynamic effects start to be important) to the final velocity of 300 Km/h increasing the velocity by 50 Km/h for each simulation.
The definition of the prism layer in *Star CCM+* has been created by means of:

- Prism layer total thickness, set as $\delta = 10\ mm$;
- First cell near wall distance $y_1 = 0.03\ mm$;
- Total number of layers. $N = 8$ prism layers have been set.

To improve the prism layer mesh quality, the following modifications have been done:

- Minimum prism layer thickness reduction percentage from 10% to 1%
- Number of prism layers reduction percentage from 50% to 10%.
- Near core layer aspect ratio (ratio of the first core cell and the last prism layer cell) set to 1

Now the computational fluid domain contains around 42 milions of cells.

The following figures show the distribution of the wall y^+ around the car. The aim of having values of *wall* $y^+ < 5$ for most of the car has been reached.

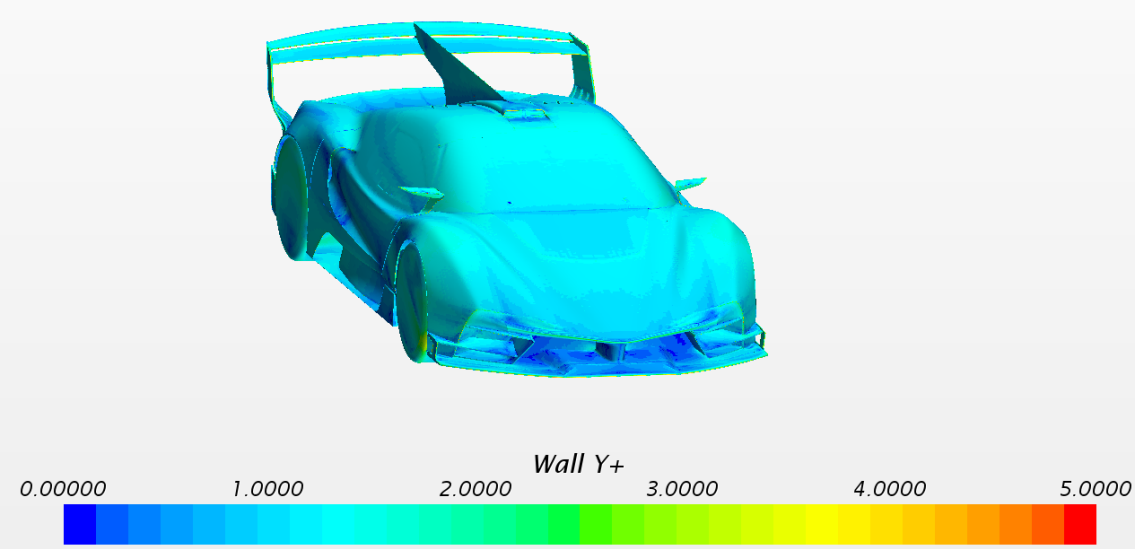

(a) Isometric view

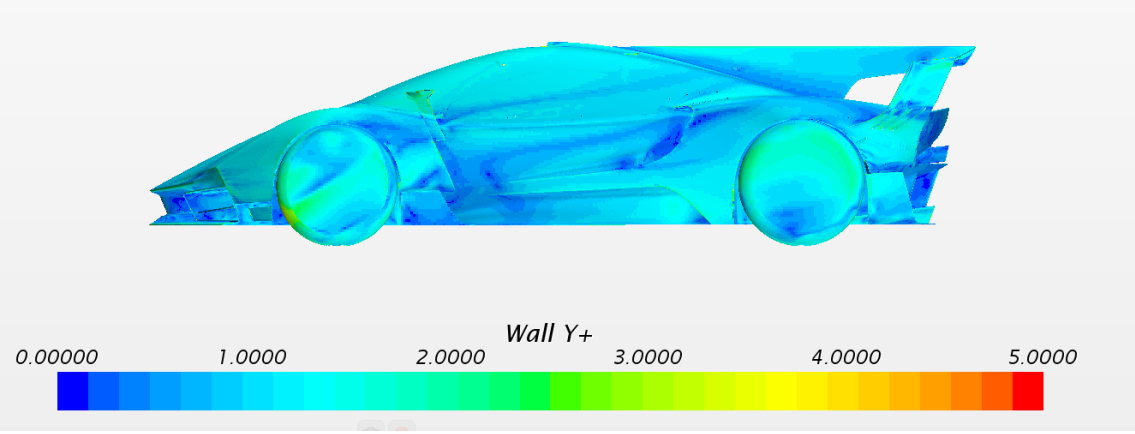

(b) Side view

Fig. 5.3.15: Wall y^+ at 100 Km/h

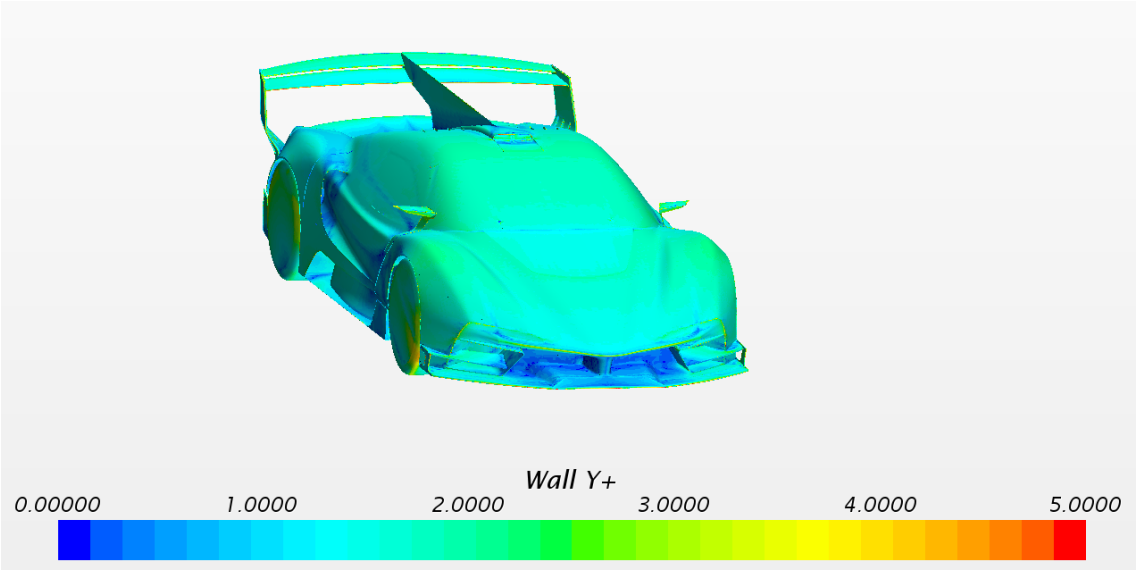

(a) Isometric view

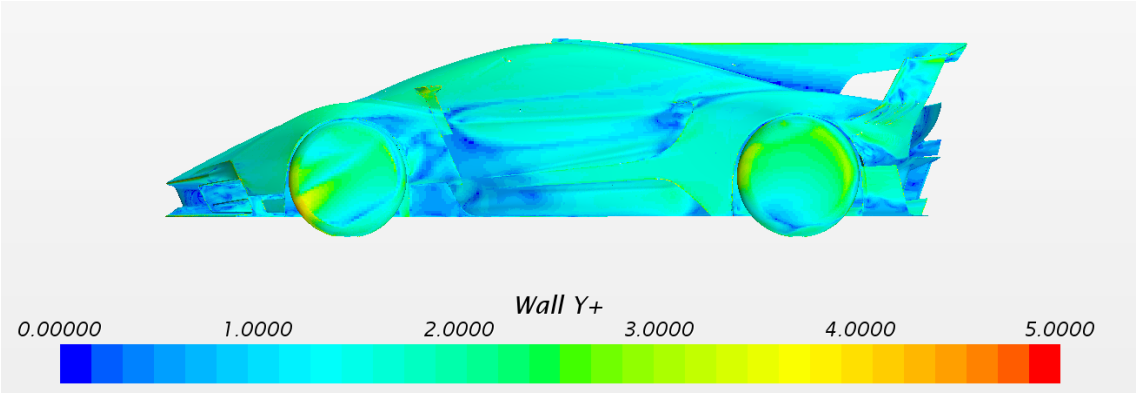

(b) Side view

Fig. 5.3.16: Wall y^+ at 150 Km/h

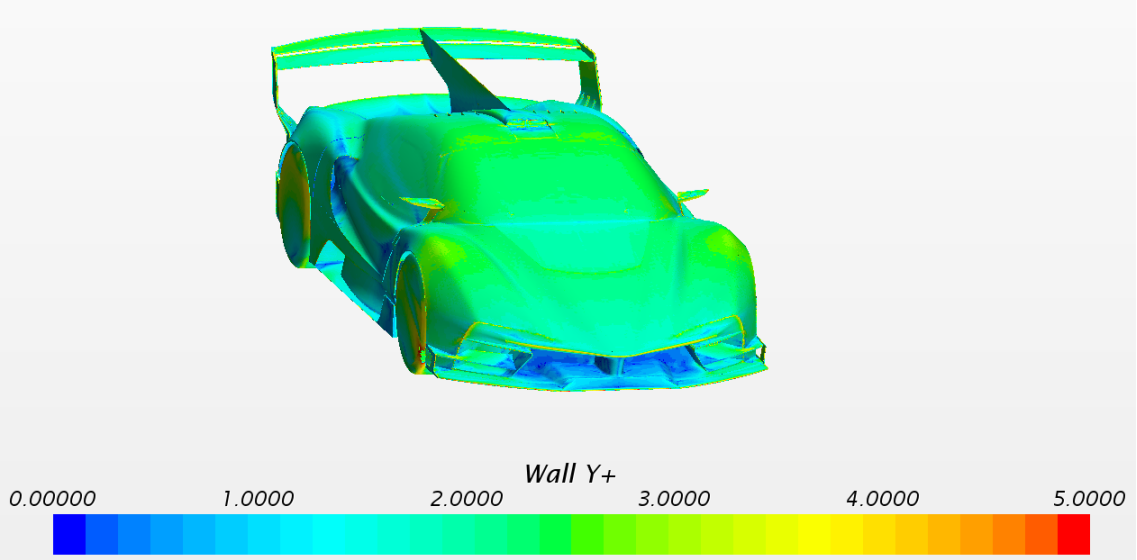

(a) Isometric view

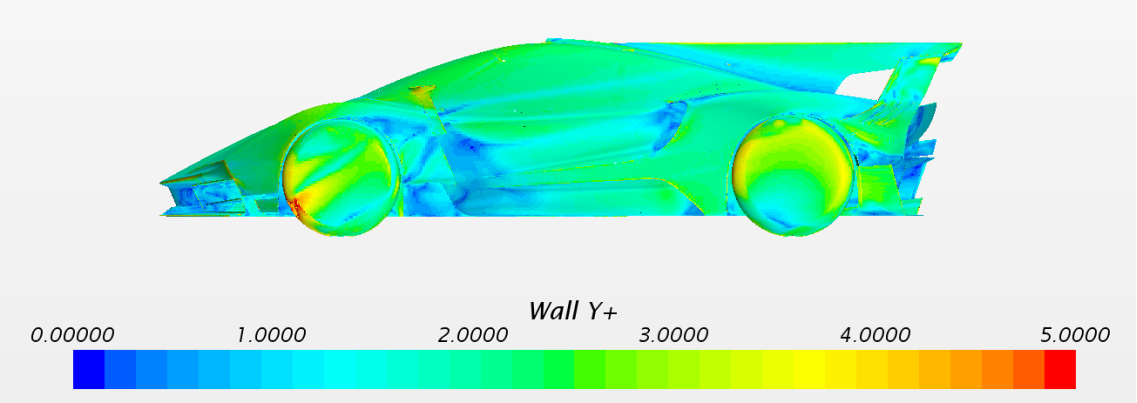

(b) Side view

Fig. 5.3.17: Wall y^+ at 200 Km/h

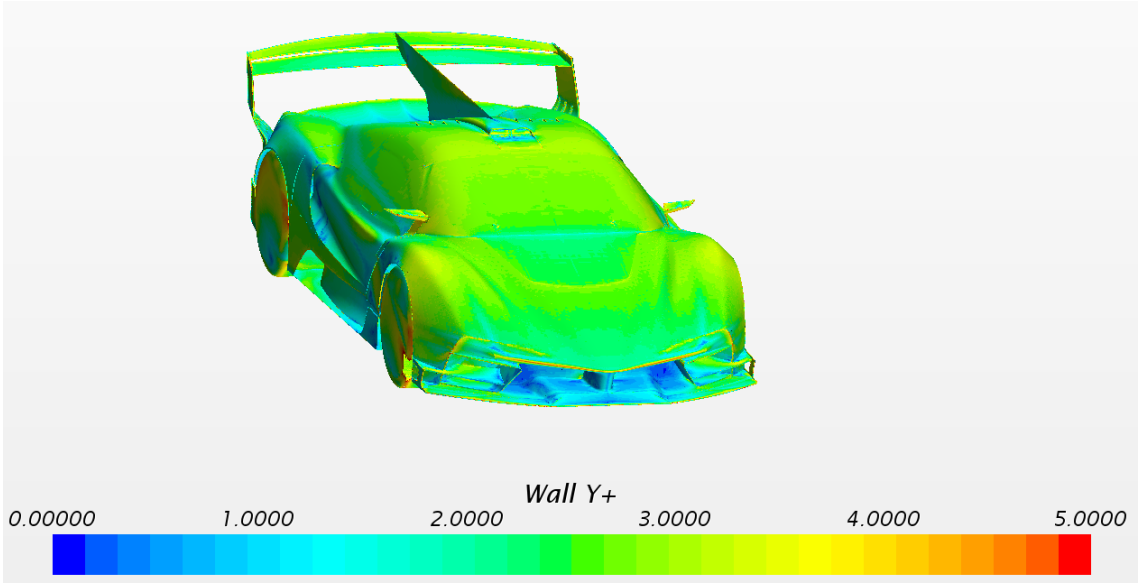

(a) Isometric view

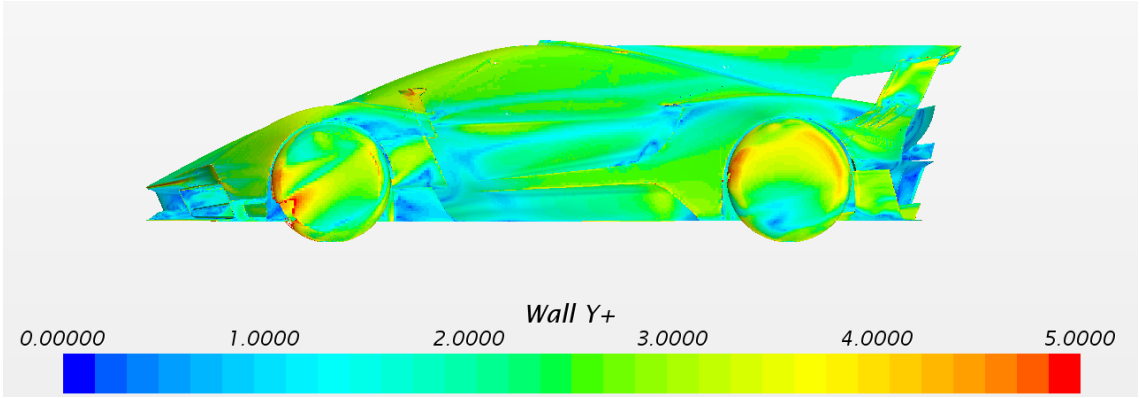

(b) Side view

Fig. 5.3.18: Wall y^+ at 250 Km/h

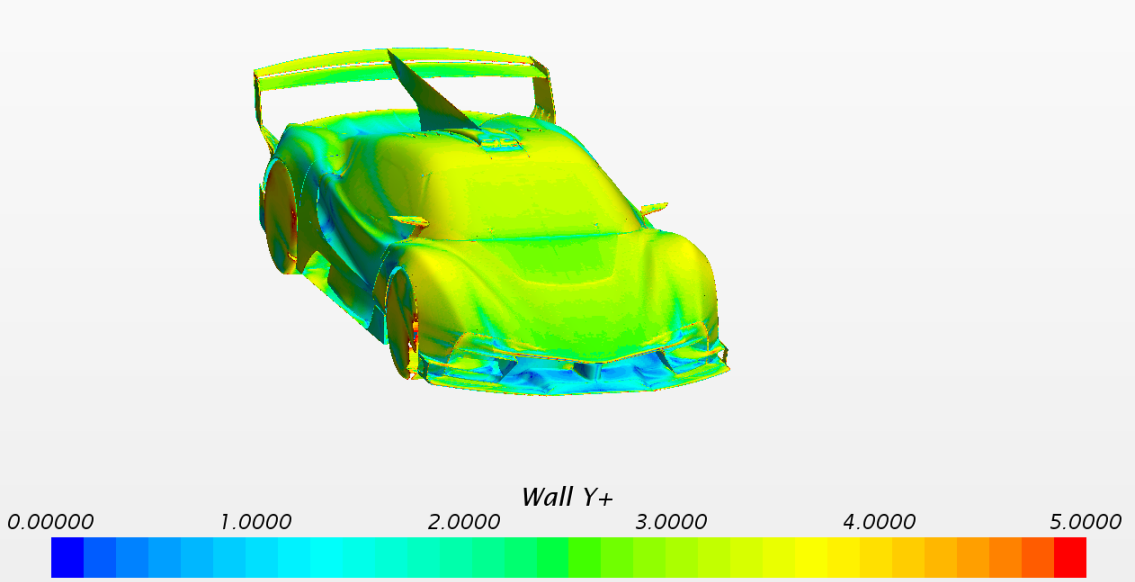

(a) Isometric view

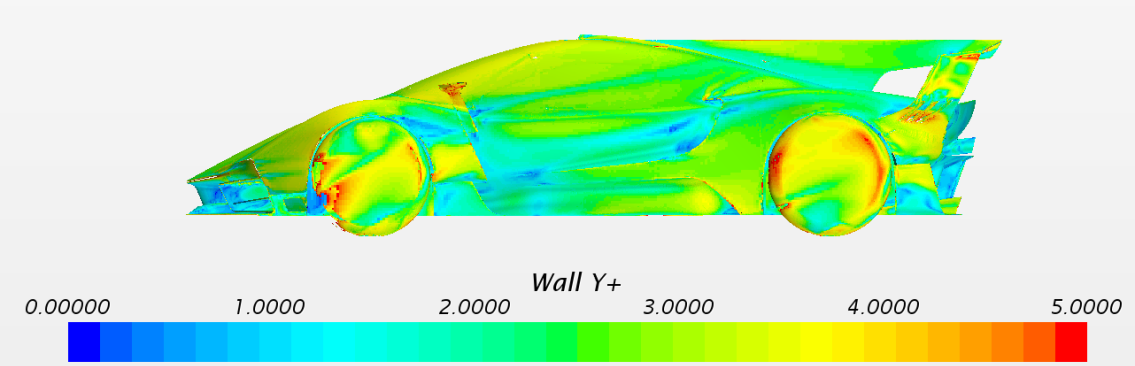

(b) Side view

Fig. 5.3.19: Wall y^+ at 300 Km/h

5.4 Post processing

Once the simulations have been completed, the performance of the car in terms of C_x, C_z, C_m (coefficients of drag, lift and pitching moment around the center of gravity of the car), downforce at both the axles can be plotted.
To evaluate the pitching moment coefficient on the car, there is need of a specification: the distribution of mass is uknown, so the entire body has been considered as a homogeneous body, making the center of mass be equivalent to the geometric center of the car, as the following pictures show.

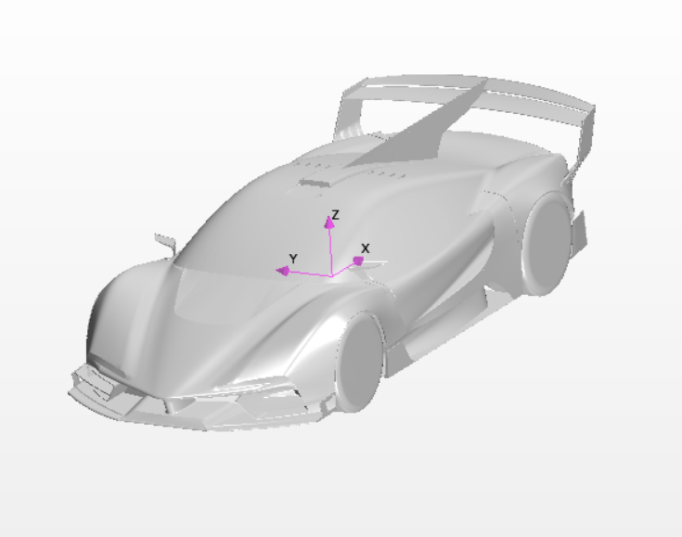

(a) CG reference sysyem - Isometric view

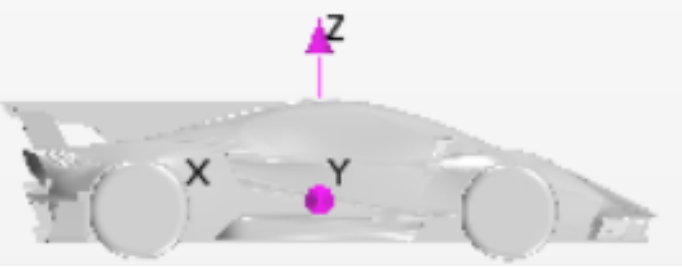

(b) CG reference sysyem - Side view

Fig. 5.4.1: Center of gravity coordinate system

Other reference systems on the wheels are needed, to set their rotation rate

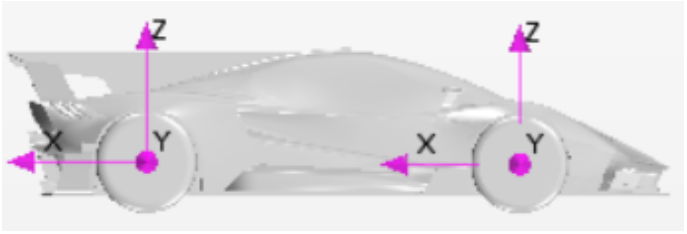

Fig. 5.4.2: Wheels' reference systems

The equation used to evaluate the local rotation rate is

$$\omega_{RPM} = \frac{10^5}{6\pi} \frac{V_{Km/h}}{\phi_{mm}} \simeq 31831 \frac{V_{Km/h}}{\phi_{mm}}$$

	Front Wheel	**Rear Wheel**
ϕ [mm]	710	736
$\omega_{\ 100\ Km/h}$ [rpm]	747	721
$\omega_{\ 150\ Km/h}$ [rpm]	1120	1081
$\omega_{\ 200\ Km/h}$ [rpm]	1494	1441
$\omega_{\ 250\ Km/h}$ [rpm]	1867	1801
$\omega_{\ 300\ Km/h}$ [rpm]	2240	2162

Table 5.3: Set up of the wheels' rotation rate

Other reference systems are required to determine the downforce distribution on the axles of the car.

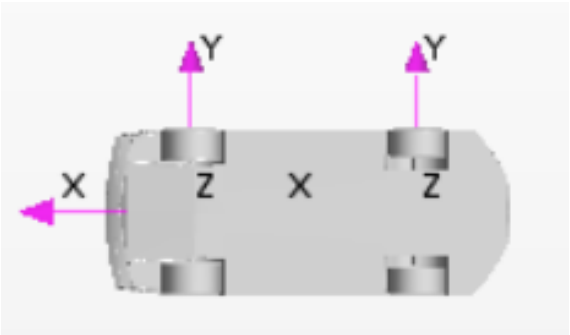

(a) Axles reference systems - Isometric view

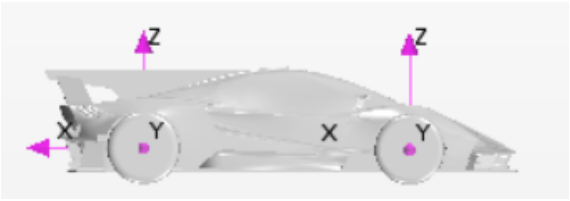

(b) Axles reference systems - Side view

Fig. 5.4.3: Axles coordinate systems

The downforce on the axles are determined by the moment's reverse formula, dividing the pitching moment acting on the opposite axle by the wheelbase.

$$F_{\,rear\ axle} = \frac{M_{\,front\ axle}}{wb} \qquad\qquad F_{\,rear\ axle} = -\frac{M_{\,rear\ axle}}{wb}$$

The wheelbase length of the car is $wb = 2700\ mm$
The last coordinate reference system used is positioned on the root aifroil of the low spoiler, around which the spoiler's incidence will be changed.

Fig. 5.4.4: Low spoiler's reference system

The performance of the original car are shown in the following pages.

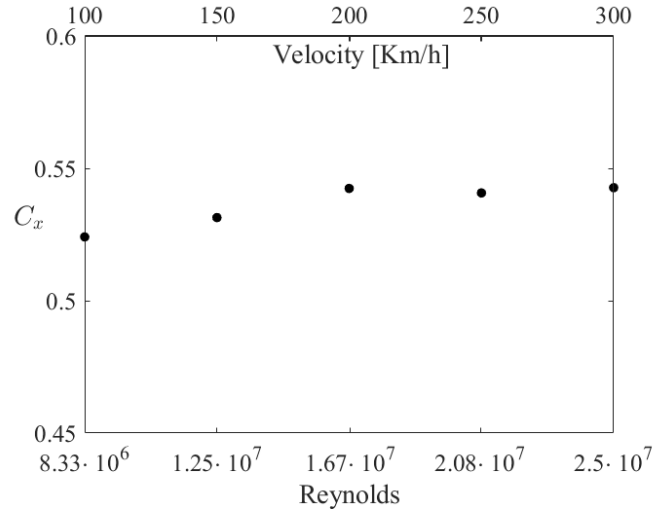

(a) $Re - C_x$ diagram

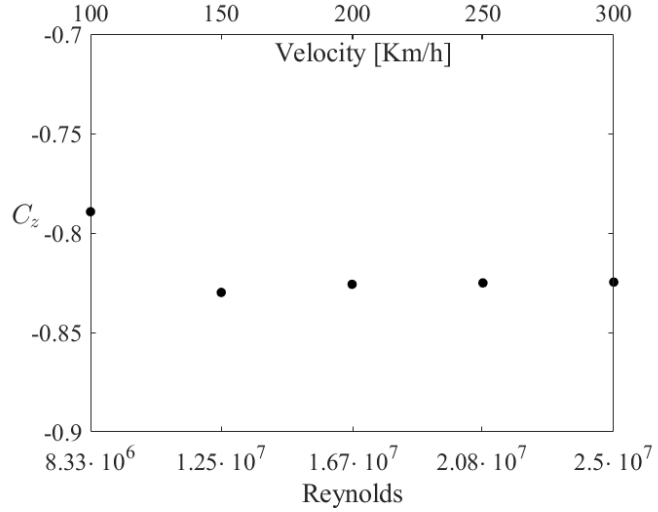

(b) $V - C_z$ diagram

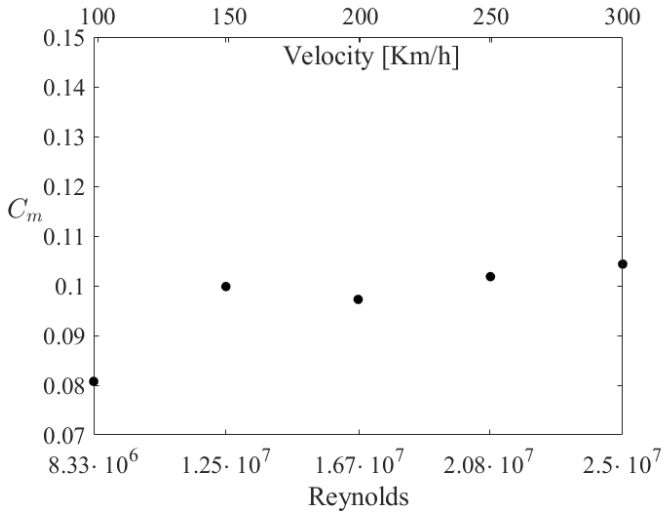

(c) $Re - C_m$ diagram

Fig. 5.4.5: Performance of the original car

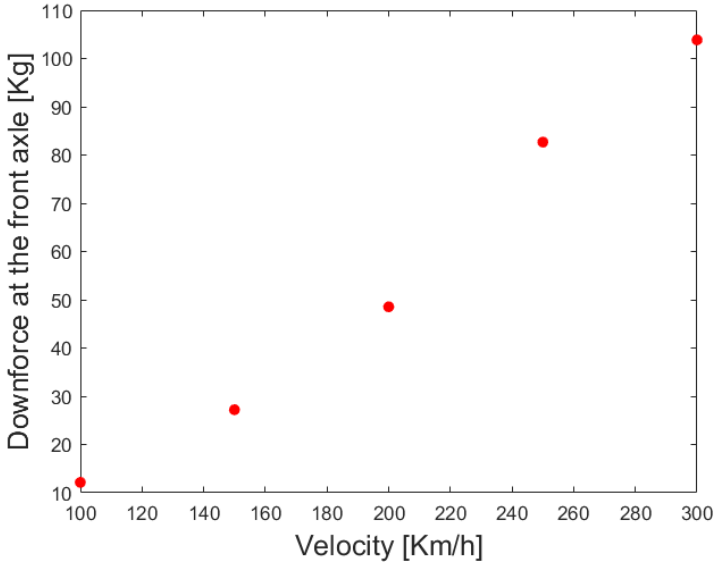

(a) Dependency of the downforce at the front axle on the velocity

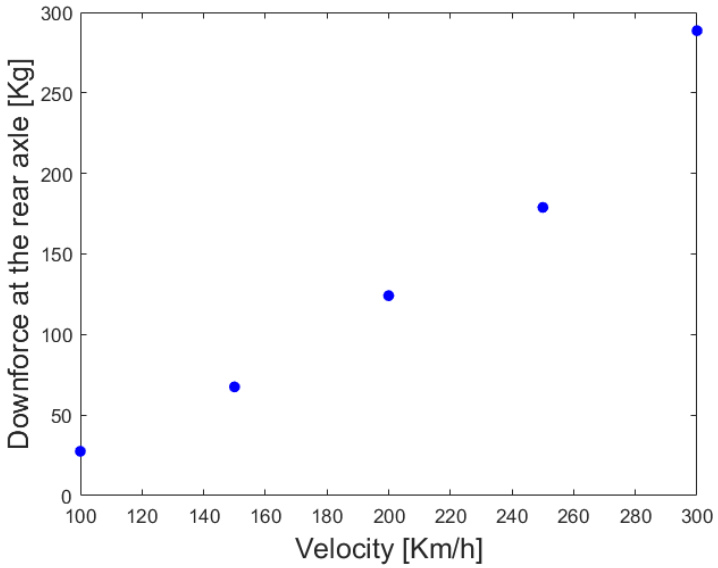

(b) Dependency of the downforce at the rear axle on the velocity

Fig. 5.4.6: Downforce-Velocity diagrams on the axles at the axles of the original car

	100 Km/h	150 Km/h	200 Km/h	250 Km/h	300 Km/h
DF front [Kgf]	12	27	49	83	104
DF rear [Kgf]	27	67	124	178	289

Table 5.4: Downforce on the axles of the original car

To evaluate the flow field around the car and to see the separation of the flow, the pressure and the wall shear stress on the car have been studied.

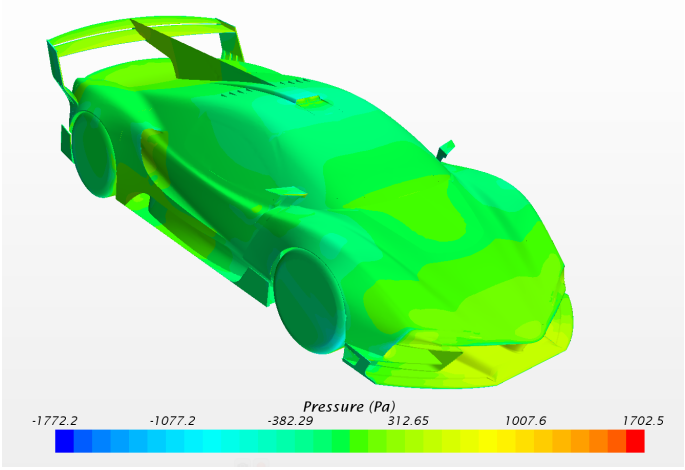

(a) Isometric view

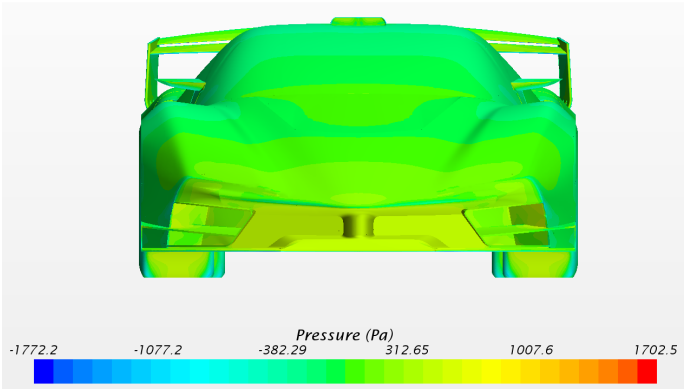

(b) Front view

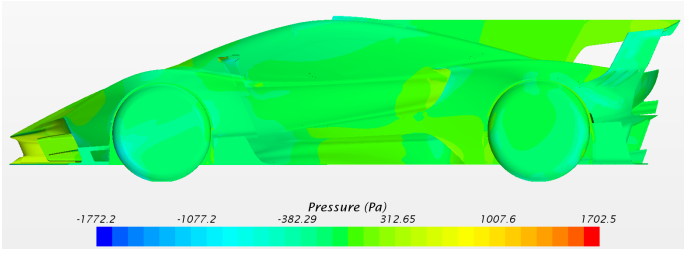

(c) Side view

Fig. 5.4.7: Pressure field around the car at $V = 100\ Km/h$

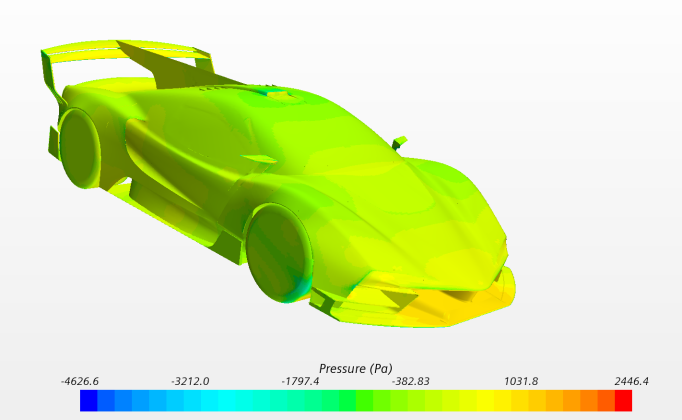

(a) Isometric view

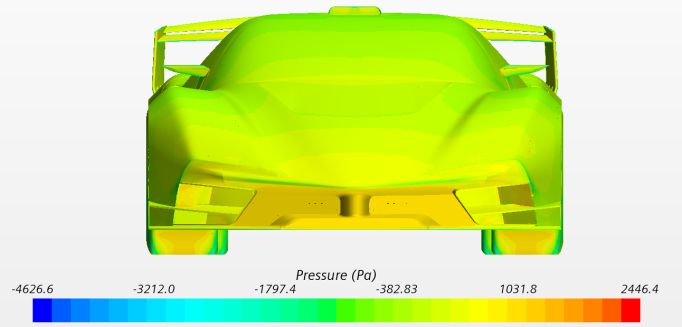

(b) Front view

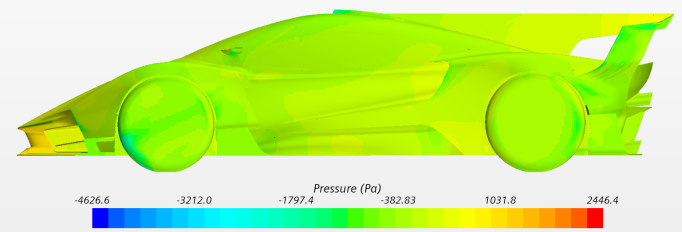

(c) Side view

Fig. 5.4.8: Pressure field around the car at $V = 150\ Km/h$

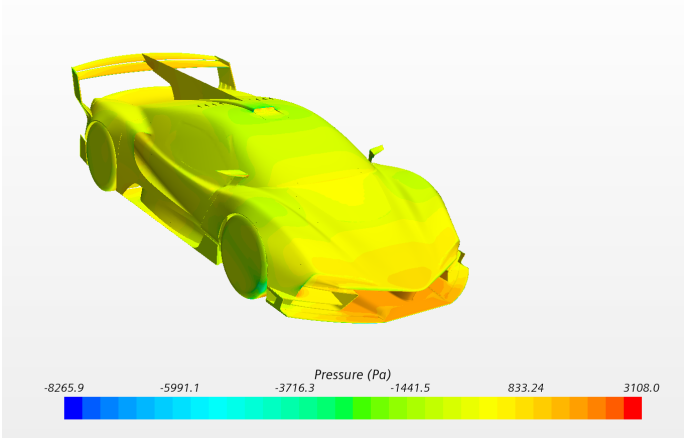

(a) Isometric view

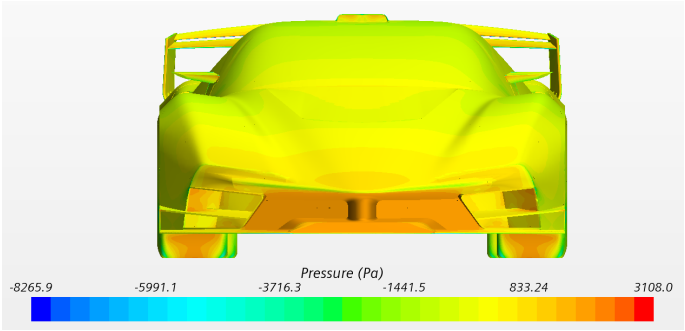

(b) Front view

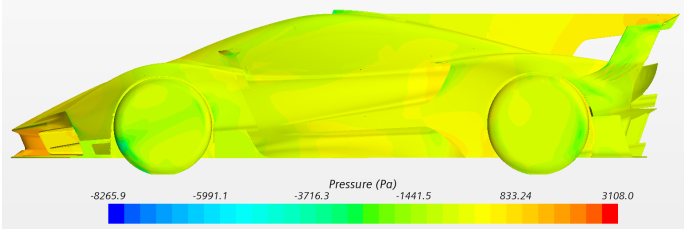

(c) Side view

Fig. 5.4.9: Pressure field around the car at $V = 200\ Km/h$

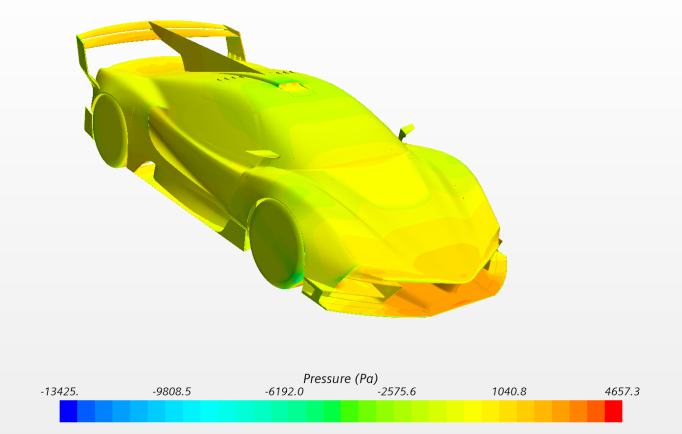

(a) Isometric view

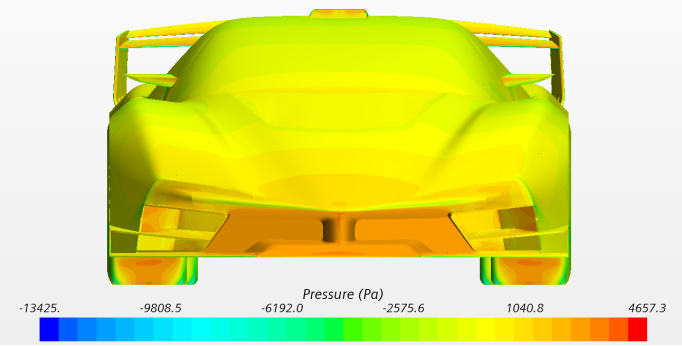

(b) Front view

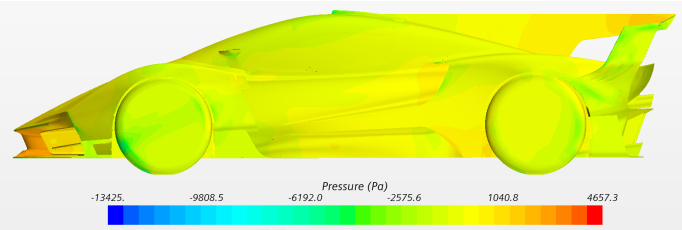

(c) Side view

Fig. 5.4.10: Pressure field around the car at $V = 250\ Km/h$

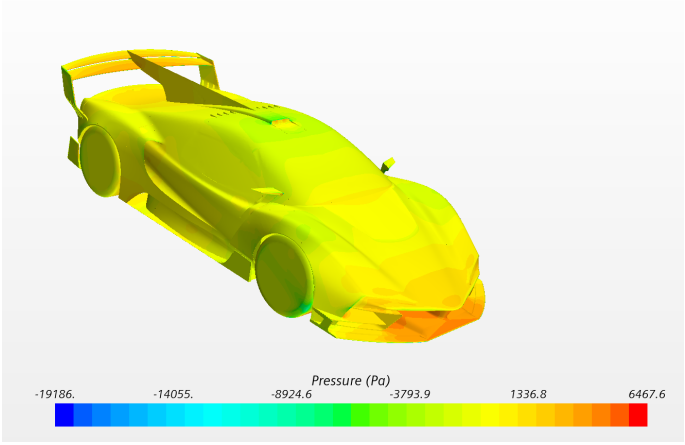

(a) Isometric view

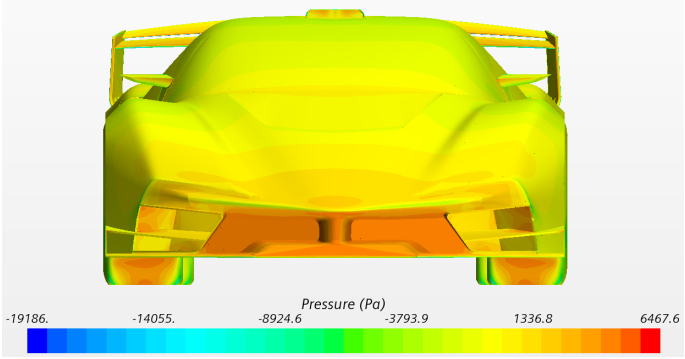

(b) Front view

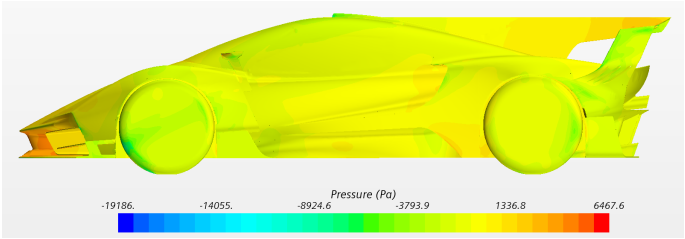

(c) Side view

Fig. 5.4.11: Pressure field around the car at $V = 300\ Km/h$

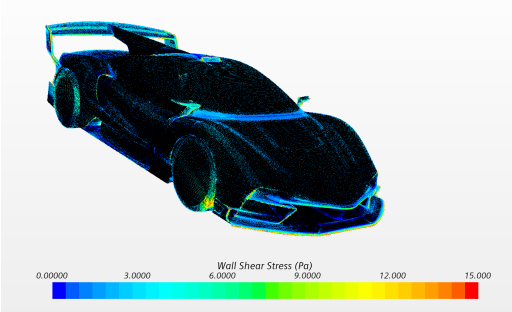

(a) Isometric view

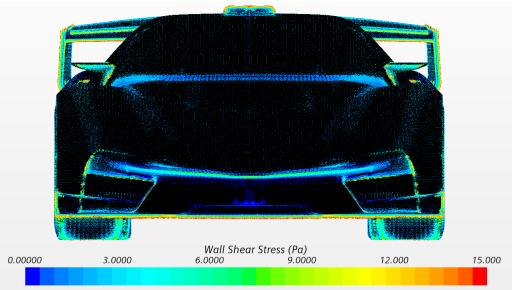

(b) Front view

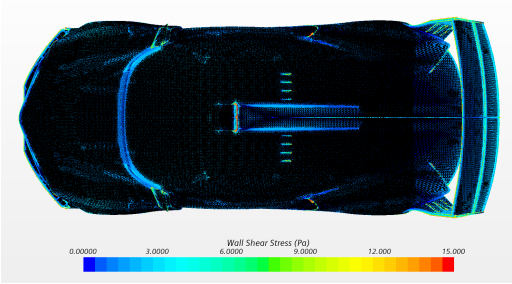

(c) Top view

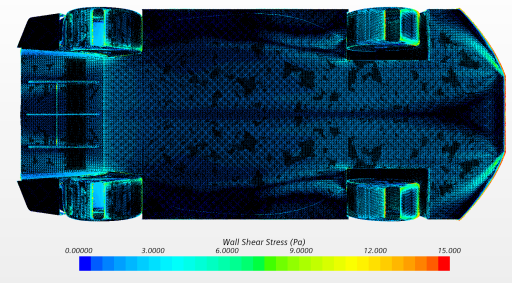

(d) Bottom view

Fig. 5.4.12: Wall shear stress at $V = 100\ Km/h$

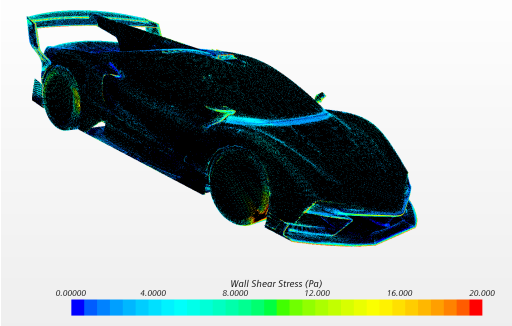

(a) Isometric view

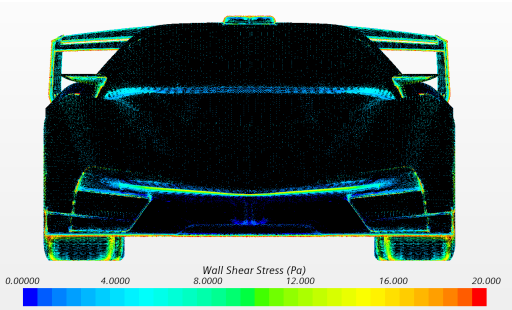

(b) Front view

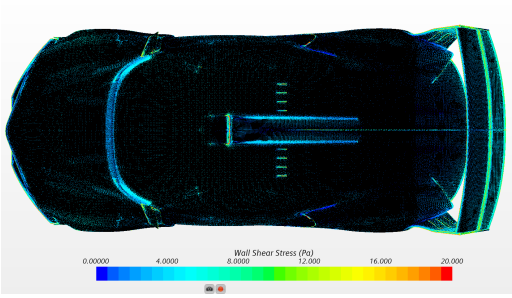

(c) Top view

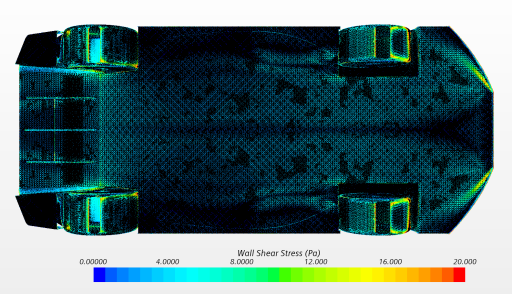

(d) Bottom view

Fig. 5.4.13: Wall shear stress at $V = 150\ Km/h$

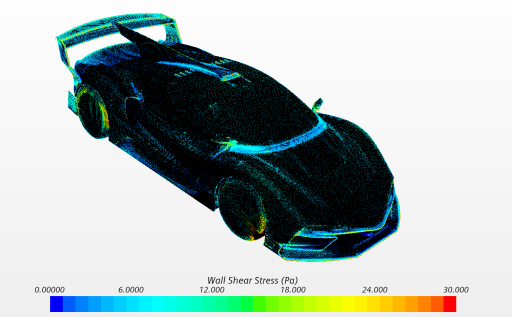

(a) Isometric view

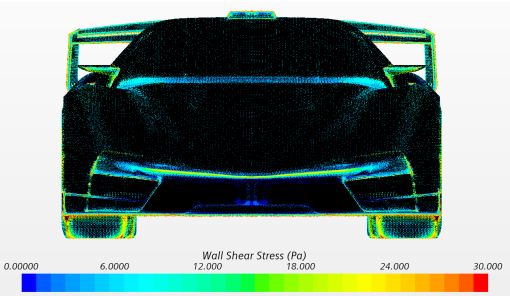

(b) Front view

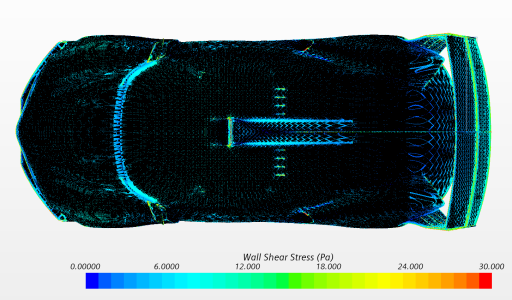

(c) Top view

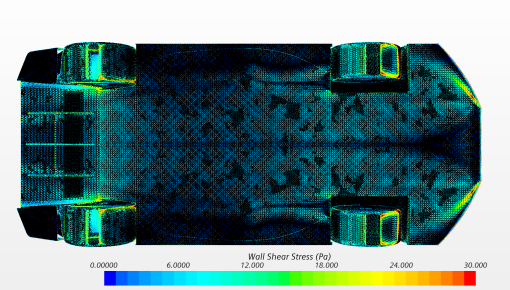

(d) Bottom view

Fig. 5.4.14: Wall shear stress at $V = 200\ Km/h$

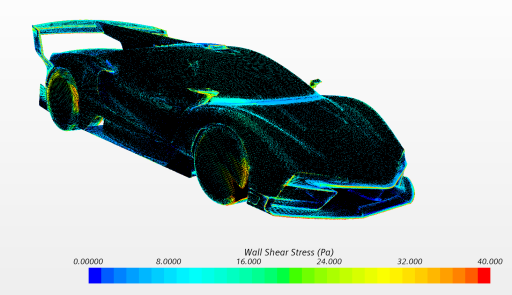

(a) Isometric view

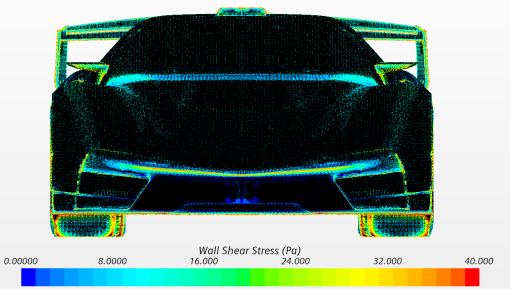

(b) Front view

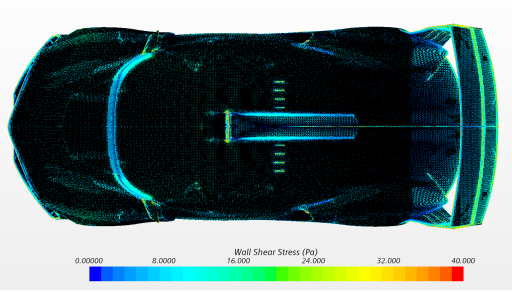

(c) Top view

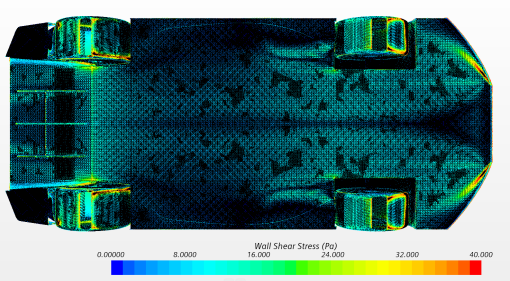

(d) Bottom view

Fig. 5.4.15: Wall shear stress at $V = 250\ Km/h$

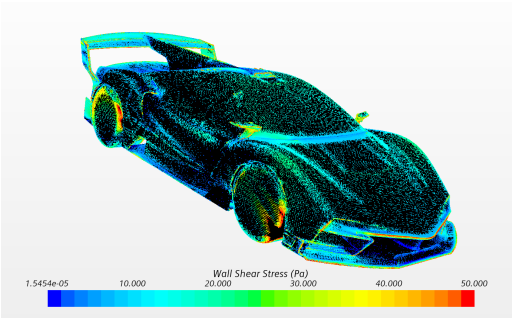

(a) Isometric view

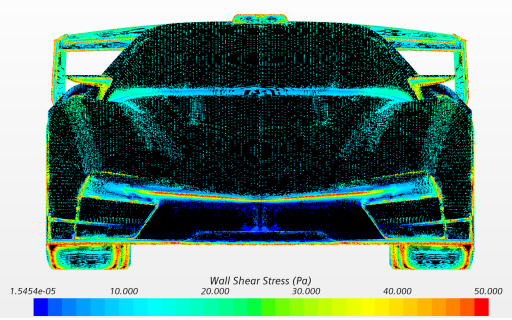

(b) Front view

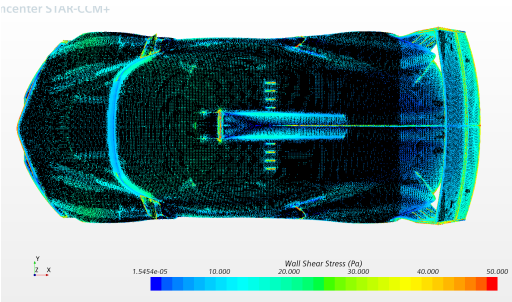

(c) Top view

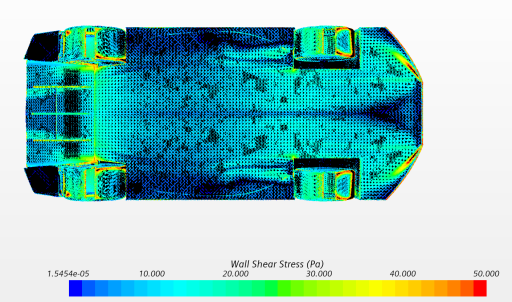

(d) Bottom view

Fig. 5.4.16: Wall shear stress at $V = 300\ Km/h$

Chapter 6

Topological optimization

6.1 First topological changes

The performance of the original car have been highlighted the main problems that have to be fixed:

- The downforce at the rear axle is greater than the downforce at the front axle. In other words, the pitching moment around the center of gravity is positive: that means that the front car tends to raise up unloading the front axle and making the wheels lose grip;
- The low spoiler is in stall condition: it will generate little downforce and increases the aerodynamic drag.

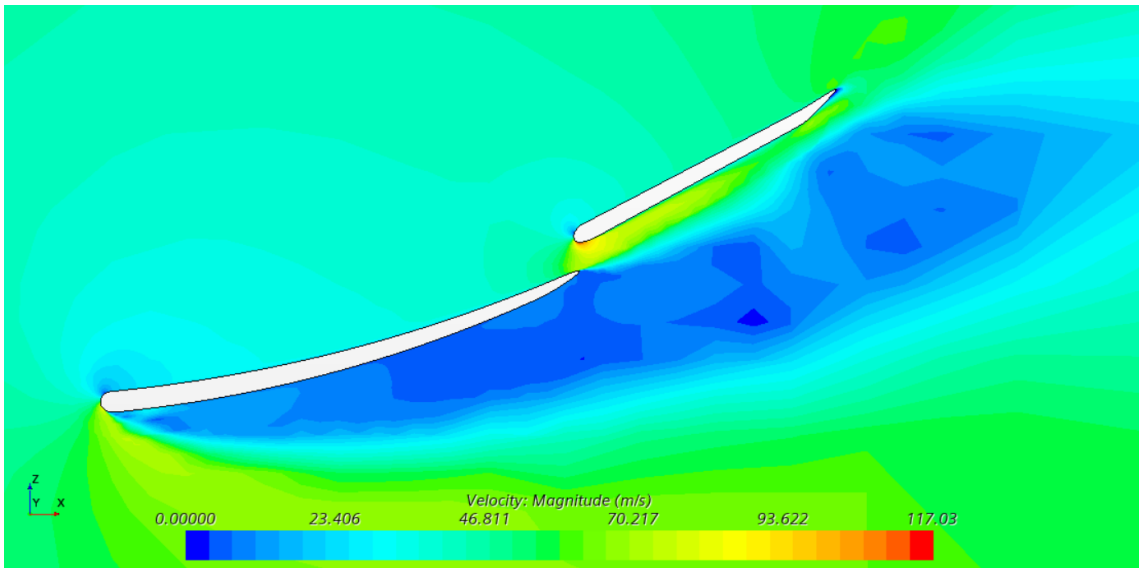

Fig. 6.1.1: Stall condition of the low spoiler

6.1.1 Variation of the car's pitch angle

In order to increase the aerodynamic load on the front of the car, the balance of the car has been changed by means of the rotation around its geometric centre of 0.5°, 1° and 1.5° The variation of the performance are shown in the figures below.

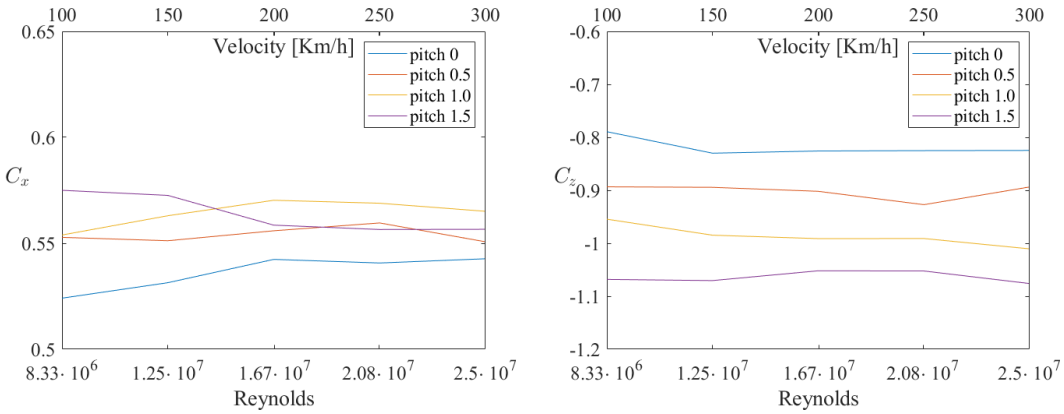

(a) $Re - C_x$ diagram

(b) $Re - C_z$ diagram

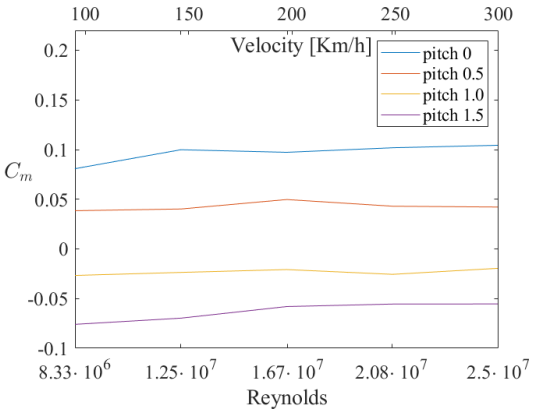

(c) $Re - C_m$ diagram

Fig. 6.1.2: Performance of the car at pitch angle variation

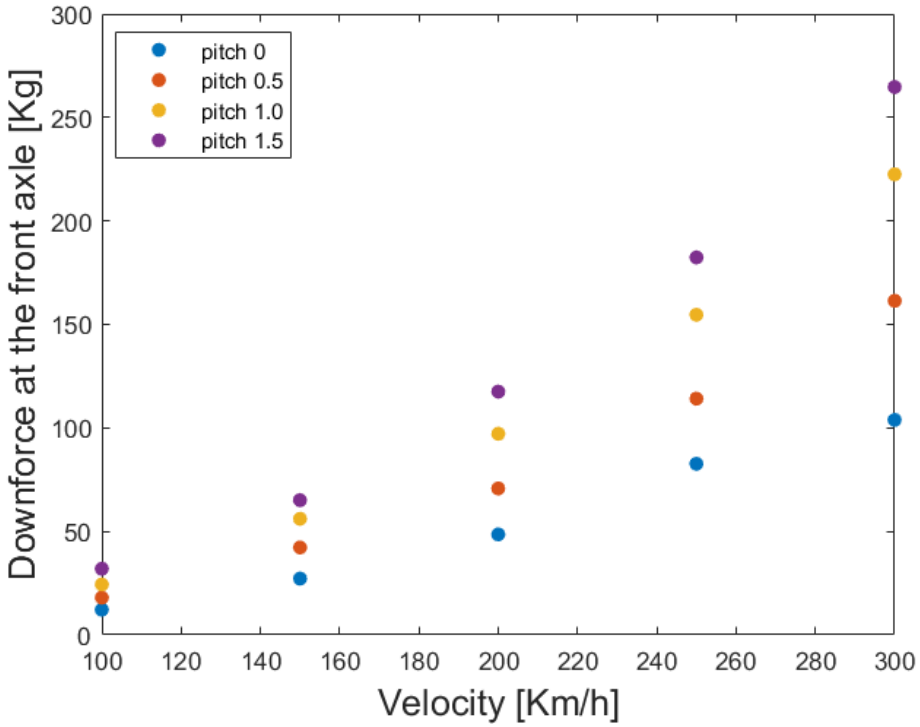

(a) Dependency of the downforce at the front axle on the velocity

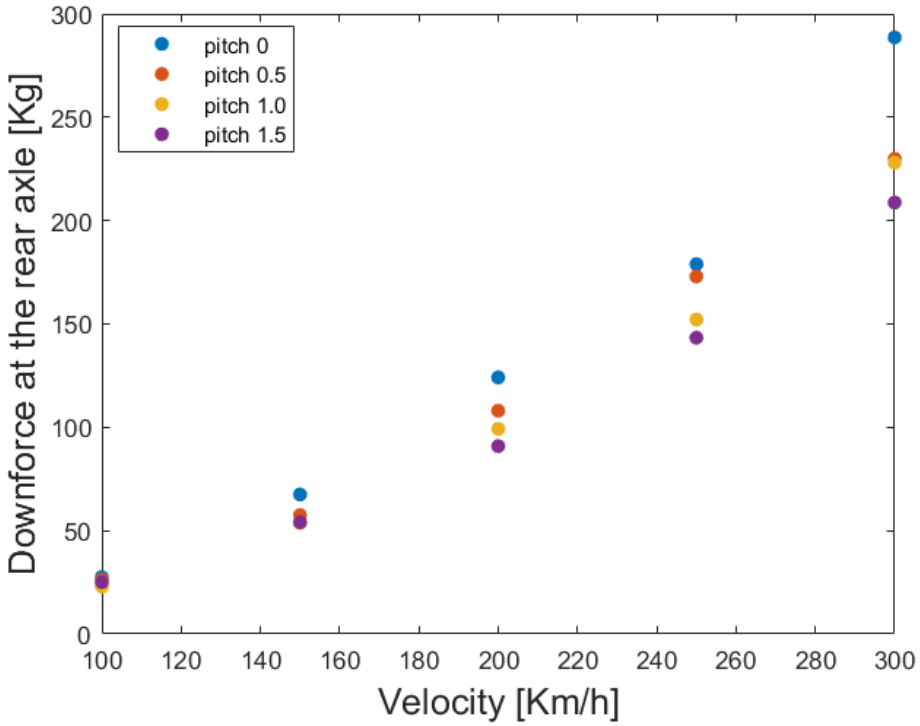

(b) Dependency of the downforce at the rear axle on the velocity

Fig. 6.1.3: Downforce at the axles at pitch variation

As it supposed, increasing the pitch of the car, the downforce at the front axle has been increased, unloading the rear axle. This variation can be seen also on the coefficient of pitching moment, reaching negative values for pitching angles values of 1° and 1.5°. Of course, both the downforce and the aerodynamic drag have been increased.
To see more clearly the variation of the performance, average values of C_x and C_z have been analyzed in the following tables.

Average C_x	**Pitch angle [°]**	**Variation**
0.536	0	-
0.554	0.5	+3.30 %
0.564	1	+5.20 %
0.568	1.5	+5.98 %

Table 6.1: Variation of the mean value of C_x with the car's pitch change

Average C_z	**Pitch angle [°]**	**Variation**
-0.819	0	-
-0.902	0.5	+10.15 %
-0.986	1	+20.44 %
-1.064	1.5	+29.89 %

Table 6.2: Variation of the mean value of C_z with the car's pitch change

The following tables show how many kilogram-forces of downforce act on the axes at each pitch angle, and the average front/rear axle aerodynamic load distribution at the pitch angle change.

	100 Km/h	150 Km/h	200 Km/h	250 Km/h	300 Km/h
DF front [Kgf]	18	42	70	114	161
DF rear [Kgf]	26	57	108	173	230

Table 6.3: Downforce on the axles at 0.5° angle pitch

	100 Km/h	150 Km/h	200 Km/h	250 Km/h	300 Km/h
DF front [Kgf]	27	56	97	155	161
DF rear [Kgf]	22	54	99	152	228

Table 6.4: Downforce on the axles at 1° angle pitch

	100 Km/h	150 Km/h	200 Km/h	250 Km/h	300 Km/h
DF front [Kgf]	32	65	117	182	265
DF rear [Kgf]	25	54	91	143	209

Table 6.5: Downforce on the axles at 1.5° angle pitch

Pitch angle [°]	**Average Front/Rear downforce distribution**[%/%]
0	29/71
0.5	41/59
1	50/50
1.5	56/44

Table 6.6: Average downforce distribution on the axle at the pitch angle change

6.1.2 Variation of the low spoiler incidence

As mentioned before, the aerodynamic stall at the low spoiler increases only the aerodynamic drag without any other benefit. To move the spoiler from the stall, the variation of the low spoiler incidence i_{low} is needed.
The characteristics of the two spoilers are listed in the table below.

	c [mm]	t	i [°]	Δi [°]
Low spoiler	198	1	15.5	-3
High spoiler	120	0.74	30	-9

Table 6.7: Characteristics of the original spoilers

where:

- c is the chordlength;
- t is the taper ratio, the ratio between root and tip chord length;
- i is the root incidence;
- Δi is the twist angle, the difference between root and tip incidence.

Starting again from the original car, the low spoiler incidence has been decreased by 2°, 4°, 6° and 8° and the simulations for $V = 200\ km/h$ have been run. The results are shown in the following pages

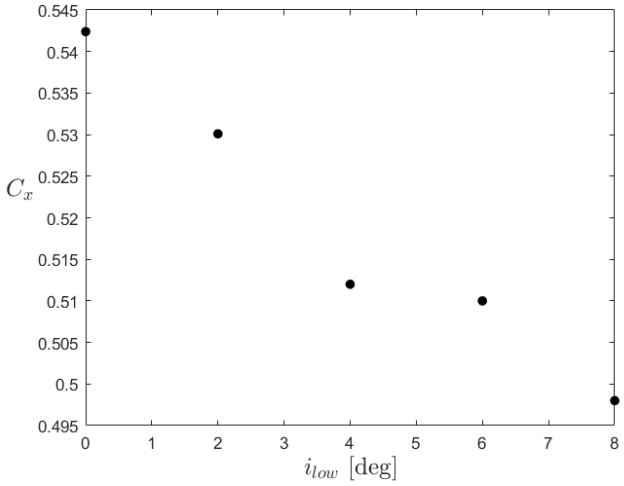

(a) $i_{low} - C_x diagram$

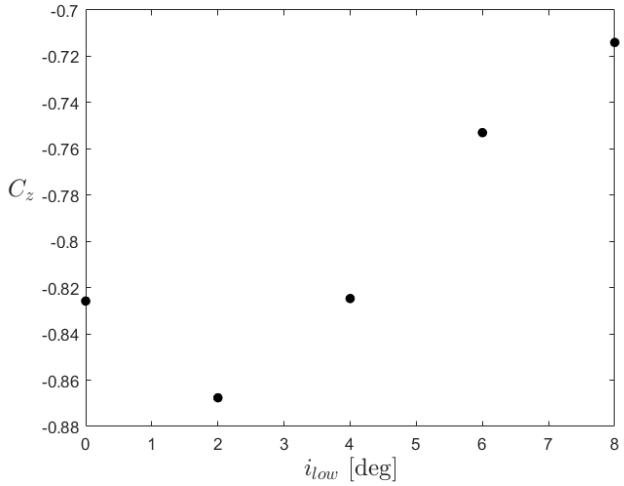

(b) $i_{low} - C_z$ diagram

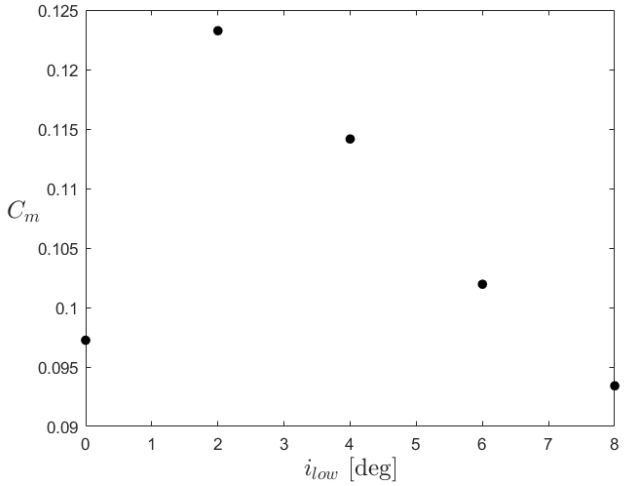

(c) $i_{low} - C_m$ diagram

Fig. 6.1.4: Performance of the car at the low spoiler incidence change at 200 Km/h

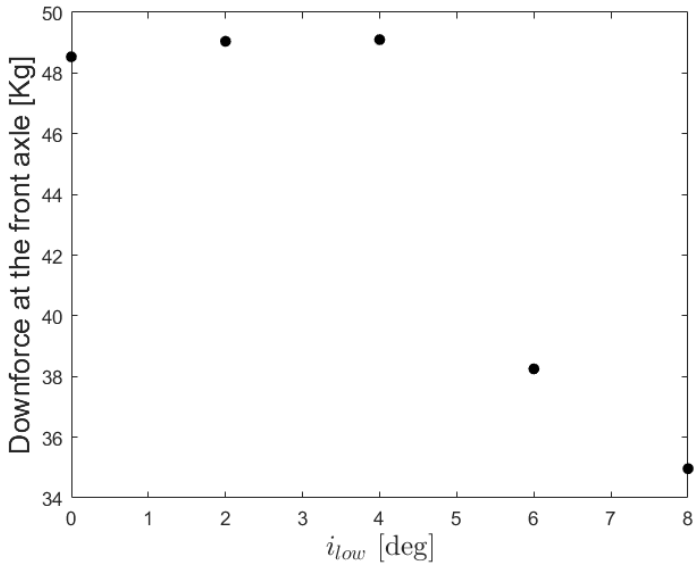

(a) Dependency of the downforce at the front axle on the low spoiler incidence

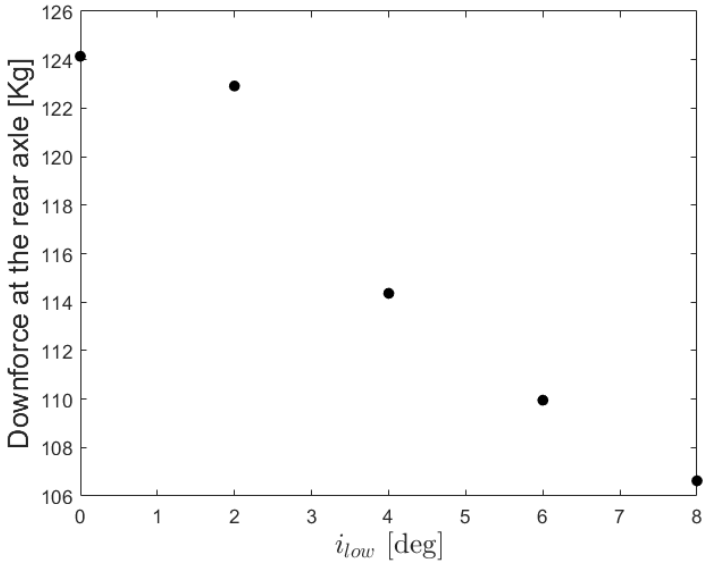

(b) Dependency of the downforce at the rear axle on the low spoiler incidence

Fig. 6.1.5: Downforce-incidence diagrams on the axles at the axles at the low spoiler incidence change

6.1.3 Performance analysis of the 1.5° pitched car, 8° change of low spoiler incidence and spoilers' airfoils

The chosen solution has been considered the best trade-off one to move the downforce towards the front axle and decrease the aerodynamic drag coefficient, reaching the aim of drag reduction and balancing the aerodynamic load on the axles. The following figures show the difference between the initial car and the improved car obtained by changing the pitching angle and lowering the low spoiler incidence. Furthermore, the original airfoils have been replaced by the NACA 2408 airfoils.

(a) The original airfoil

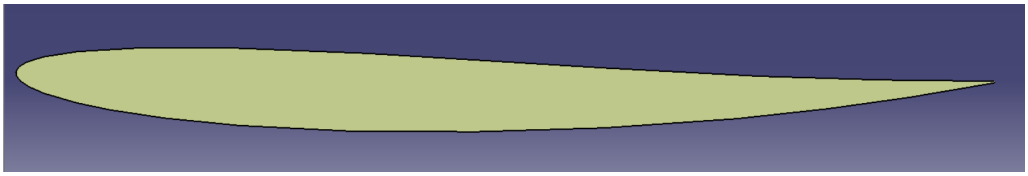

(b) The NACA 2408 airfoil

Fig. 6.1.6: The replacement of the spoilers' airfoils

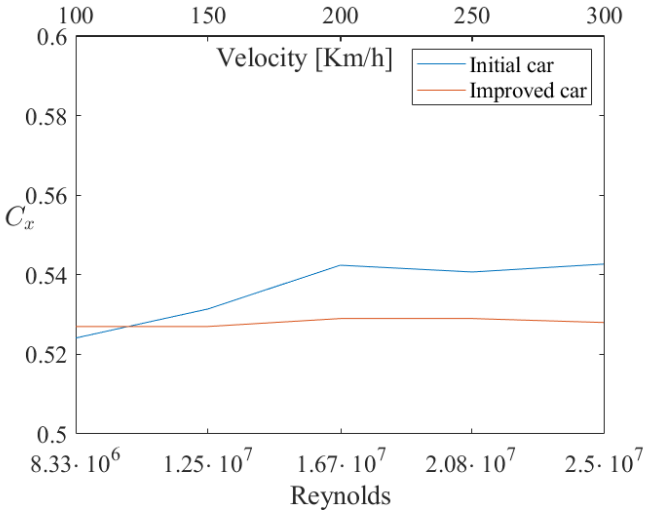

(a) $Re - C_x$ diagram

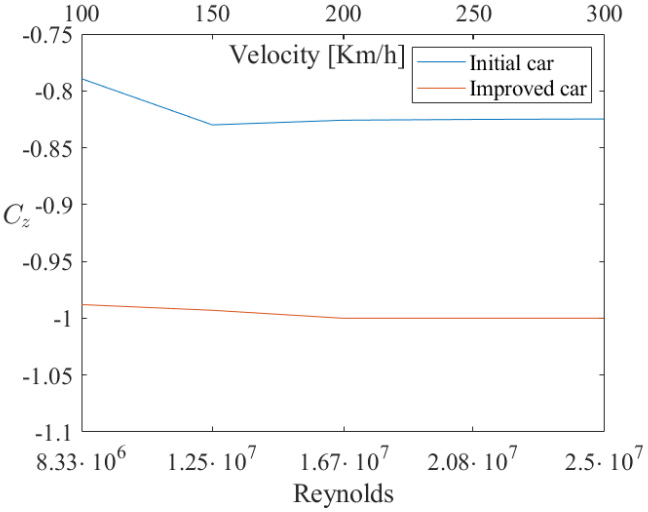

(b) $Re - C_z$ diagram

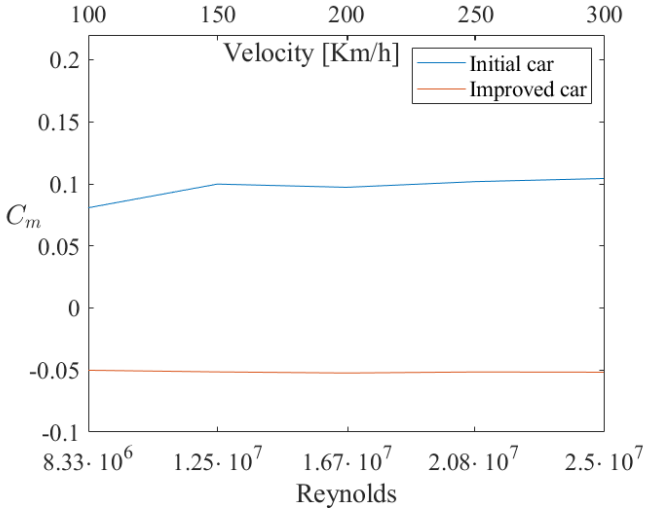

(c) $Re - C_m$ diagram

Fig. 6.1.7: Difference between the performance of initial and the improved car

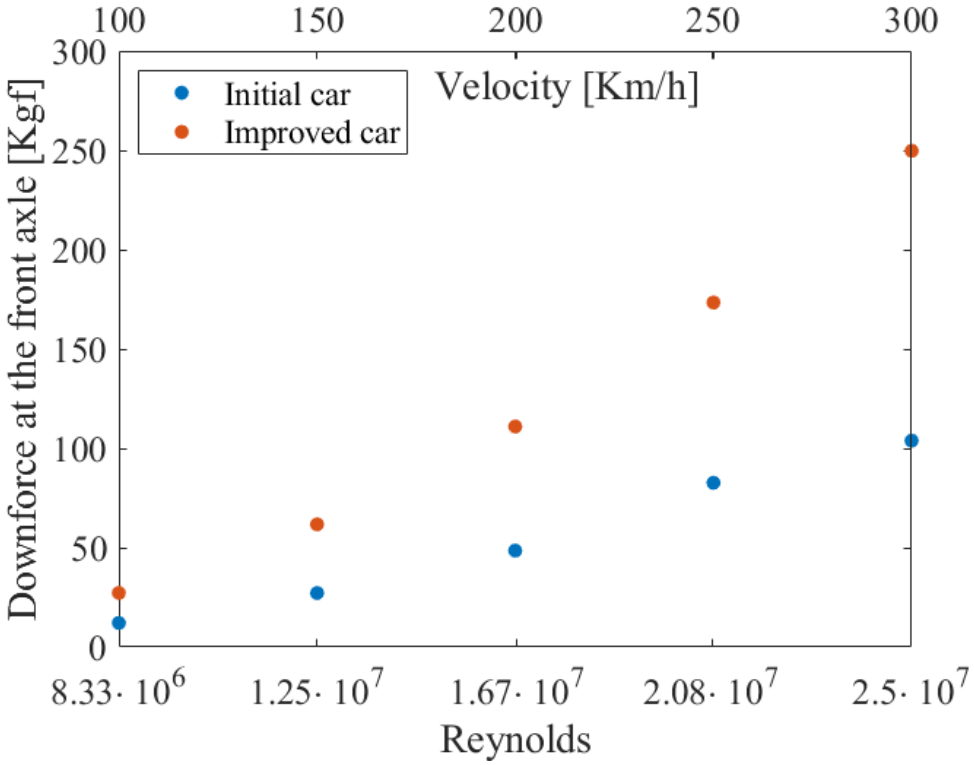

(a) Dependency of the downforce at the front axle on the velocity

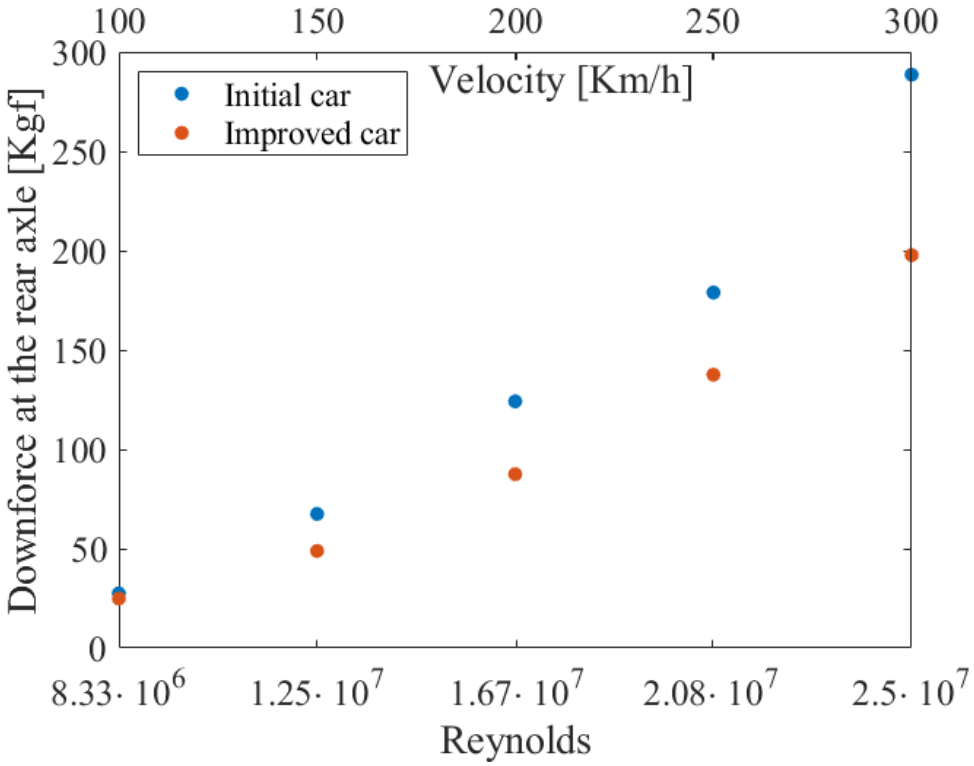

(b) Dependency of the downforce at the rear axle on the velocity

Fig. 6.1.8: Difference between the initial and the improved car's downforce at the axles

At the end of these improvements, the numerical quantities to show more clearly the improvement of the car are expressed below.

	Inital	**Current**	**Variation**
Average C_x	0.536	0.528	- 1.5%
Average C_z	-0.819	-0.996	+ 21.6%

Table 6.8: Variation of the mean value of drag and lift coefficients between initial and improved car change

Moreover, the balancing of the car has been improved, as it can be seen in:

- The mean value of the coefficient of pitching moment C_m: it changes from a positive value to a negative one, which shows the tendency of the final car to lower the nose in lieu of rising it like before the improvement, with a positive moment coefficient;
- The change of front/rear axle aerodynamic load distribution from 28%/72% to 56%/44%, which better expresses the change of moment coefficient.

6.2 Further topological improvements

6.2.1 Change of the splitter geometry

Besides the analysis of the modified car, the flow separation below the car due to the splitter has been noticed by the velocity field on the symmetry plane section.

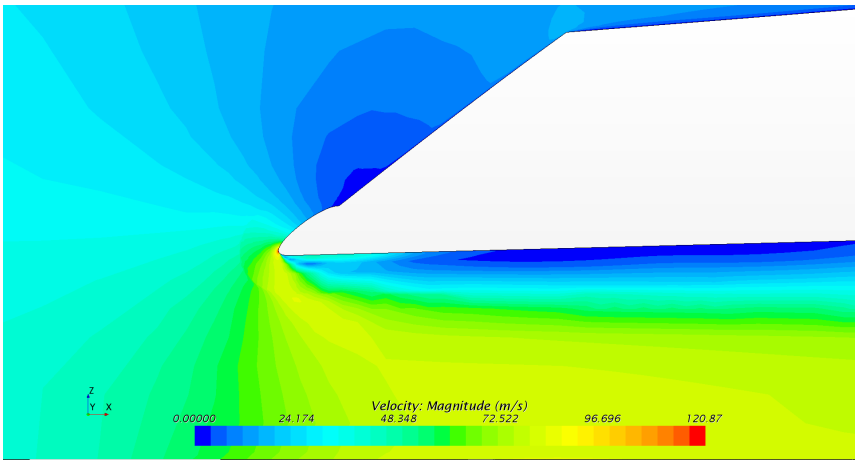

Fig. 6.2.1: Stall condition of the original splitter

The splitter's geometry has been modified using the CAD software, trying to drive the flow under the car in a better way.

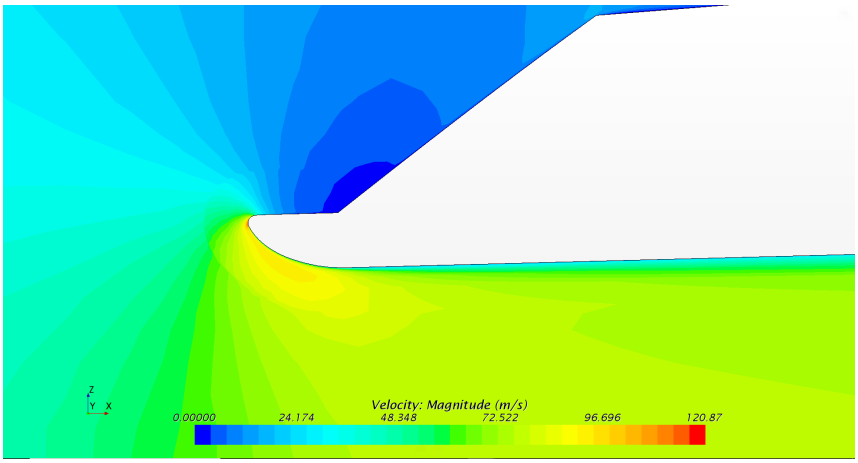

Fig. 6.2.2: Flow around the modified splitter

The flow doesn't stall anymore on the splitter, making the drag coefficient of the car further decrease. After this change, analyzed for the case $V = 200\ Km/h$, the aerodynamic drag has been reduced by 3.6% The flow reaches the separation anyway towards the wheels, and downforce coefficient results lower than before (considering the absolute value, from -1.002 to -0.957). The attempt of this topological optimization has been kept, as the goal of a further reduction of drag resistance has been reached.

6.2.2 Twist angle removal on the high spoiler

After the incidence variation of the low spoiler, it doesn't guide anymore the flow on the lower part of the high spoiler; the consequence is the high spoiler stall.

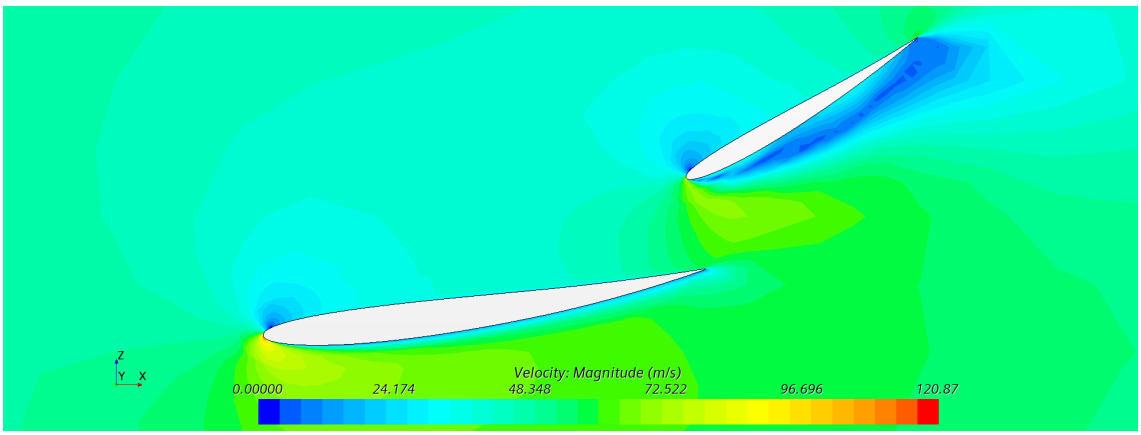

Fig. 6.2.3: Stall condition of the high spoiler

As seen before, the stall of a spoiler makes it lose its aerodynamic properties. The low spoiler stall is visible only on the first sections, as the twist angle lowers the airfoils' incidence towards the tip. Instead of changing the twist angle, it has been completely remove, setting the entire spoiler's incidence equal to the tip's one, with an overall root incidence reduction by 9°. The high spoiler does not stall anymore, reduction of both drag (0.481) and downforce (-0.898)

For this case, the overall drag reduction is there is an excellent drag reduction, but the decrease of downforce coefficient has been considered excessive. That's why, in order to increase downforce at the expense of the increase of drag coefficient, a Gurney flap on the high spoiler has been placed.

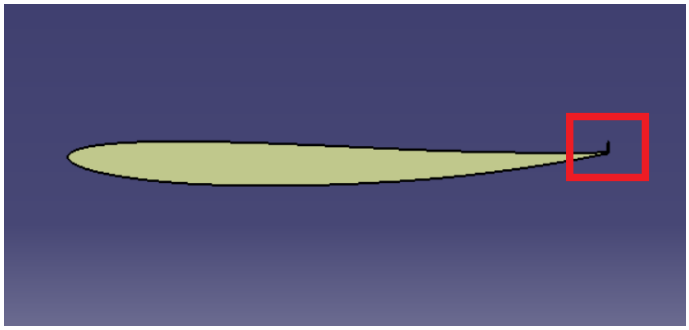

(a) The NACA 2408 airfoil with the Gurney flap

(b) Detailed view of the flap

Fig. 6.2.4: The replacement of the spoilers' airfoils

6.3 Final comparative analysis

At the end of these topological improvements, the last simulation campaign has been run.

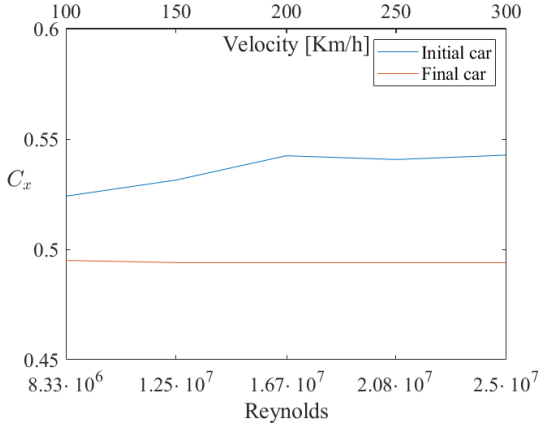

(a) $Re - C_x$ diagram

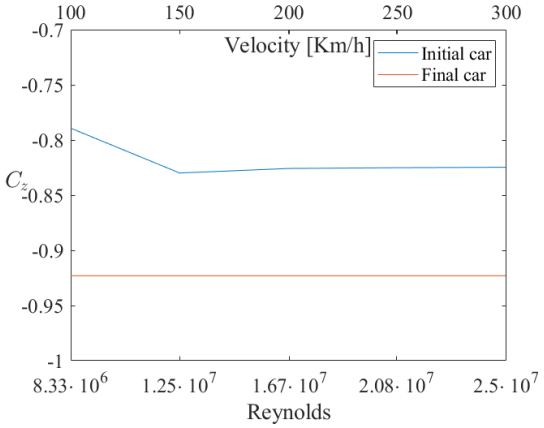

(b) $Re - C_z$ diagram

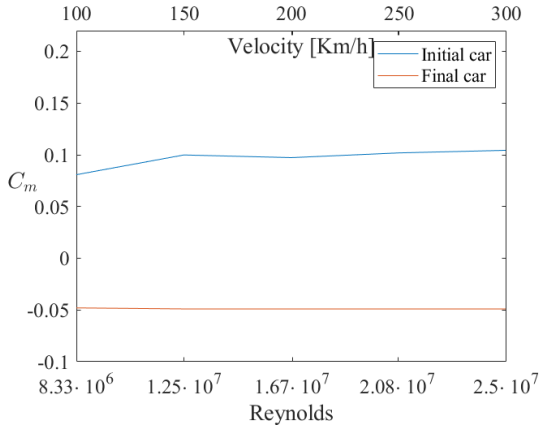

(c) $Re - C_m$ diagram

Fig. 6.3.1: Difference between the performance of initial and the final car

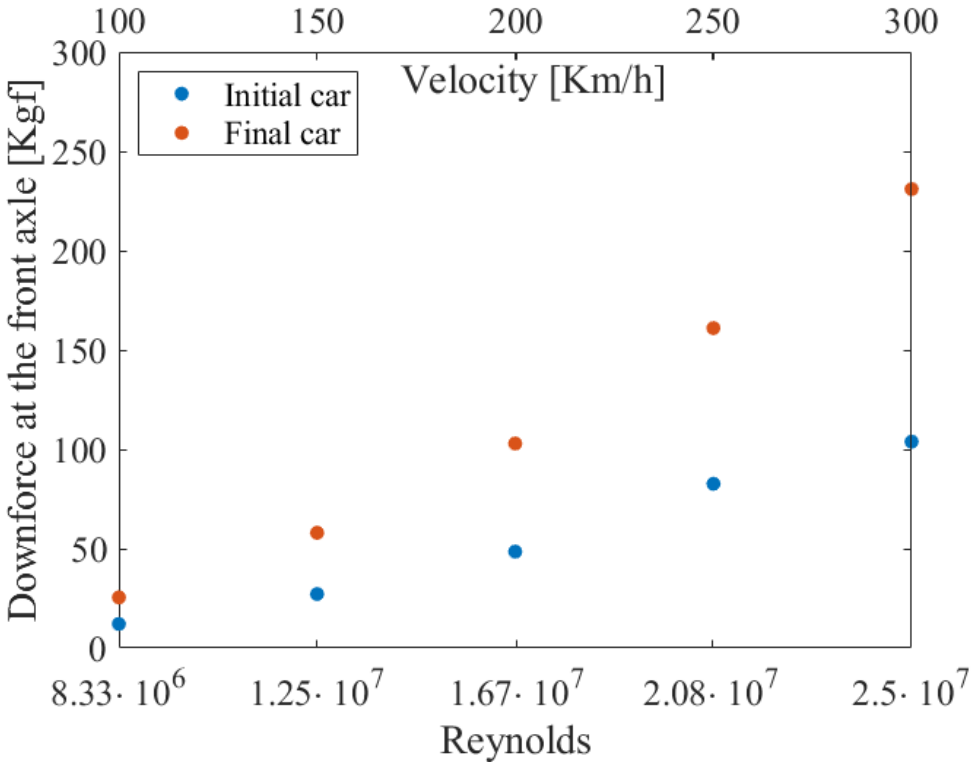

(a) Dependency of the downforce at the front axle on the velocity

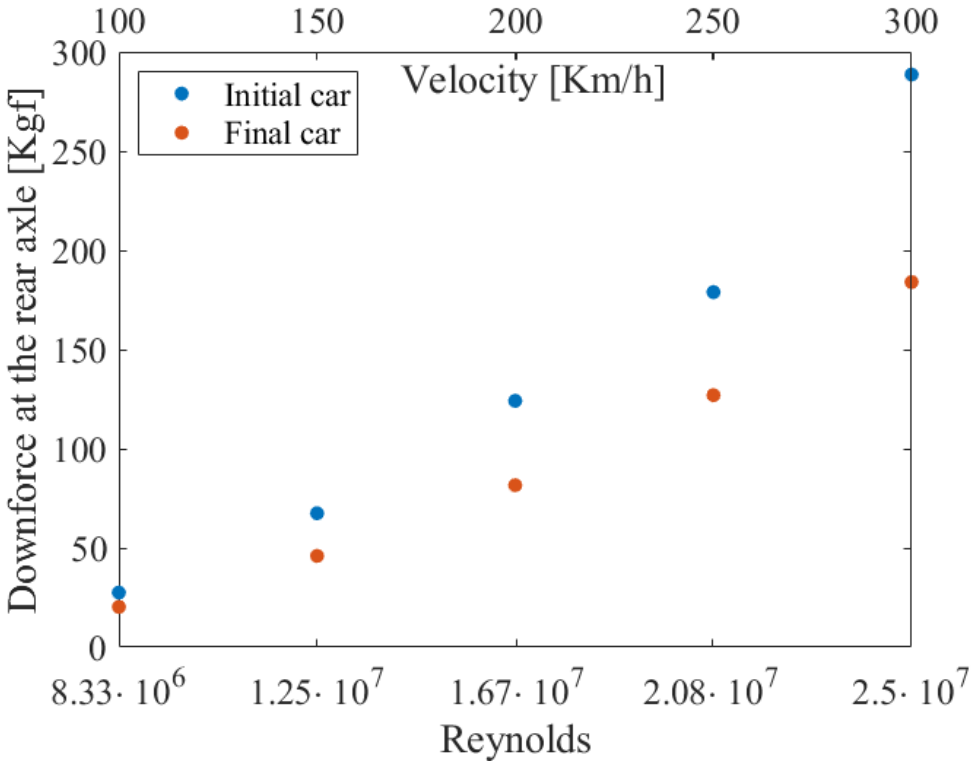

(b) Dependency of the downforce at the rear axle on the velocity

Fig. 6.3.2: Difference between the initial and the final car's downforce at the axles

Final conclusions

At the end of these improvements, the numerical quantities to show more clearly the improvement of the car are expressed below.

	Inital [°]	**Current**	**Variation**
Average C_x	0.536	0.494	- 7.8%
Average C_z	-0.819	-0.923	+ 12.7%

Variation of the mean value of drag and lift coefficients between initial and final car change

In comparison with the first modified car, the pitching moment coefficient remains negative (-0.049) and the aerodynamic load distribution at the front and rear axles remains the same as the intermediate step (56%/44%). The preset goals have been reached. The final car is aerodynamically balanced and drag have been reduced; Moreover, the final car produces more downforce than the initial one.

List of Figures

1.4.1 Finite and fixed control volume 5
1.5.1 Difference between laminar and turbulent flow 8
1.5.2 Unsteady behaviour of turbulent flows 9
1.6.1 Boundary layer 11
1.6.2 Transition from laminar to turbulent boundary layer . . 15
1.6.3 Structure of the inner layer of a turbulent boundary layer 16
1.6.4 Generation of drag and downforce over an airfoil 17
1.6.5 Example of pressure coefficient distribution over an airfoil 18

2.1.1 Drag on a vehicle 20
2.1.2 Decrease of the drag coefficient during the years 21
2.1.3 Difference between attached and separated flow 22
2.1.4 Flow separation mechanism 22
2.1.5 Velocity field, streamlines and wake on a race car 23
2.1.6 Laminar and turbulent separation on a sphere 24
2.1.7 $C_D - Re$ diagram of a sphere 24
2.1.8 Vortex generators 25
2.2.1 Approximation of a front end and related streamlines . . 26
2.2.2 Reduction of drag coefficient with hood and windshield inclination 27
2.2.3 Dependency of drag coefficient o the front end inclination 27
2.2.4 Approximation of A-pillar and windshield and related streamlines 28
2.2.5 Inclination angles of the windshield 29
2.2.6 Dependency of the drag coefficient on the roof camber . 30
2.2.7 The boat tailing technique 30
2.2.8 Dependency of the drag coefficient on the slant angle φ . 31
2.2.9 Difference between sharped and rounded shoulders . . . 32
2.2.10 Vortices on a 3D rotating wheel on the ground 33
2.2.11 Drag coefficient at increasing yaw angle 34
2.2.12 Deck strip and a free standing airfoil 35

3.0.1 Types of high performance vehicles 37
3.1.1 $F_y - \beta$ diagram 38
3.1.2 Forces on a cornering vehicle 39
3.1.3 Coefficients change over ground clearance 40
3.1.4 Effects of a rear wing 41
3.1.5 The airfoil 42
3.1.6 The 3D wing 43
3.1.7 Wing performances 43
3.1.8 The rear diffuser of a rally car 44
3.1.9 From left to right: the splitter, the dam and the frontal diffuser 45

4.1.1 Conservation law in a cell 47
4.1.2 Example of different types of mesh over the same domain 48
4.2.1 Representation of a computational domain and its boundary 49

5.0.1 The Montecarlo-BRC W12 model and its evolution . . . 52
5.1.1 Overview of the car 53
5.1.2 Geometry errors 54
5.1.3 The closed and clean car geometry 55
5.3.1 The car and the computational fluid domain block . . . 58
5.3.2 The computational fluid domain and the subtraction of the car 60
5.3.3 Comparison of the front car's mesh 61
5.3.4 Comparison of the side car's mesh 62
5.3.5 Comparison of the rear car's mesh 62
5.3.6 Comparison of the roof diffuser's mesh 63
5.3.7 Comparison of spoilers' mesh 63
5.3.8 Comparison of front external mesh 64
5.3.9 Comparison of side external mesh 64
5.3.10 Volumetric controls at the stagnation points of the car . 65
5.3.11 The volumetric control blocks 66
5.3.12 Stagnation points refinement (hood-windshield intersection example) 67
5.3.13 Wake and underbody refinement 68
5.3.14 Refinement blocks around the car 69
5.3.15 Wall y^+ at 100 Km/h 71
5.3.16 Wall y^+ at 150 Km/h 72
5.3.17 Wall y^+ at 200 Km/h 73
5.3.18 Wall y^+ at 250 Km/h 74

5.3.19 Wall y^+ at 300 Km/h 75
5.4.1 Center of gravity coordinate system 76
5.4.2 Wheels' reference systems 77
5.4.3 Axles coordinate systems 78
5.4.4 Low spoiler's reference system 78
5.4.5 Performance of the original car 79
5.4.6 Downforce-Velocity diagrams on the axles at the axles of the original car 80
5.4.7 Pressure field around the car at $V = 100\ Km/h$ 81
5.4.8 Pressure field around the car at $V = 150\ Km/h$ 82
5.4.9 Pressure field around the car at $V = 200\ Km/h$ 83
5.4.10 Pressure field around the car at $V = 250\ Km/h$ 84
5.4.11 Pressure field around the car at $V = 300\ Km/h$ 85
5.4.12 Wall shear stress at $V = 100\ Km/h$ 86
5.4.13 Wall shear stress at $V = 150\ Km/h$ 86
5.4.14 Wall shear stress at $V = 200\ Km/h$ 87
5.4.15 Wall shear stress at $V = 250\ Km/h$ 87
5.4.16 Wall shear stress at $V = 300\ Km/h$ 88

6.1.1 Stall condition of the low spoiler 89
6.1.2 Performance of the car at pitch angle variation 90
6.1.3 Downforce at the axles at pitch variation 91
6.1.4 Performance of the car at the low spoiler incidence change at 200 Km/h 95
6.1.5 Downforce-incidence diagrams on the axles at the axles at the low spoiler incidence change 96
6.1.6 The replacement of the spoilers' airfoils 97
6.1.7 Difference between the performance of initial and the improved car 98
6.1.8 Difference between the initial and the improved car's downforce at the axles 99
6.2.1 Stall condition of the original splitter 101
6.2.2 Flow around the modified splitter 101
6.2.3 Stall condition of the high spoiler 102
6.2.4 The replacement of the spoilers' airfoils 103
6.3.1 Difference between the performance of initial and the final car 104
6.3.2 Difference between the initial and the final car's downforce at the axles 105

List of Tables

5.1 Meshing campaign - variation of base size and external volume cell size 61
5.2 Meshing campaign - size variation of stagnation point's refinement and wake and underbody blocks 67
5.3 Set up of the wheels' rotation rate 77
5.4 Downforce on the axles of the original car 80

6.1 Variation of the mean value of C_x with the car's pitch change 92
6.2 Variation of the mean value of C_z with the car's pitch change 92
6.3 Downforce on the axles at 0.5° angle pitch 93
6.4 Downforce on the axles at 1° angle pitch 93
6.5 Downforce on the axles at 1.5° angle pitch 93
6.6 Average downforce distribution on the axle at the pitch angle change 93
6.7 Characteristics of the original spoilers 94
6.8 Variation of the mean value of drag and lift coefficients between initial and improved car change 100

Bibliography

[1] Anderson, J.D., *Fundamentals of Aerodynamics*, McGraw-Hill, 2011

[2] Arina, R., *Fondamenti di aerodinamica*, Levrotto & Bella, 2015;

[3] Hucho, W. H., *Aerodynamics of Road Vehicles*, SAE International, 1998

[4] D'Ambrosio, D., Notes of his lessons of Computational Fluid Dynamics at Politecnico di Torino.

[5] De Cupis, D., *Active Aerodynamics Design and Performance Optimization for Sport Vehicle*, Master Thesis in Automotive Engineering, Politecnico di Torino, 2019

[6] Kats, J., *Automotive Aerodynamics*, Wiley, 2016;

[7] Mathieu, J., *An introduction to turbulent flow*, Cambridge University Press, 2000;

[8] Quori, F., *Aerodinamica*, Levrotto & Bella, 1998

[9] Kuzmin, D., notes of his *Computational Fluid Dynamics*' course at University of Dortmund

[10] Garg, V., K., *Applied Computational Fluid Dynamics*, Marcel Dekker, Inc, 1998

[11] Moukalled, F., Mangani, L., Darwish, M., *The Finite Volume Method in Computational Fluid Dynamics*, Springer, 2016

[12] Houghton,E.L. et al, *Aerodynamics for engineering students*, Elsevier, 2016

[13] Benzing, E., *Wings - Their design and application to racing cars*, Giorgio Nada Editore, 2012